NOVA SCHOOL OF SCIENCE & TECHNOLOGY

DEPARTAMENT OF
MECHANICAL AND INDUSTRIAL ENGINEERING

DEVELOPMENTS IN DIRECTED ENERGY DEPOSITION ADDITIVE MANUFACTURING: IN-SITU HOT FORGING AND INDIRECT COOLING

VALDEMAR REBELO DUARTE

Master in Mechanical Engineering

DOCTORATE IN MECHANICAL ENGINEERING

NOVA University Lisbon

January, 2022

NOVA SCHOOL OF SCIENCE & TECHNOLOGY

DEPARTAMENT OF
MECHANICAL AND INDUSTRIAL ENGINEERING

DEVELOPMENTS IN DIRECTED ENERGY DEPOSITION ADDITIVE MANUFACTURING: IN-SITU HOT FORGING AND INDIRECT COOLING

VALDEMAR REBELO DUARTE

Master in Mechanical Engineering

Adviser: Telmo Jorge Gomes dos Santos
Associate Professor with Habilitation, NOVA University Lisbon

Co-advisers: Rosa Maria Mendes Miranda
Associate Professor with Habilitation, retired, NOVA University Lisbon

Examination Committee:

Chair: Paulo Manuel Assis Loureiro Limão Vieira,
Full Professor, *NOVA University Lisbon*

Rapporteurs: Altino de Jesus Roque Loureiro,
Full Professor, University of Coimbra
Carlos Alves da Silva,
Assistant Professor, University of Lisbon

Adviser: Telmo Jorge Gomes dos Santos,
Associate Professor with Habilitation, *NOVA University Lisbon*

Members: Eurico Gonçalves Assunção,
Invited Assistant Professor, University of Lisbon
João Pedro Oliveira,
Invited Assistant Professor, *NOVA University Lisbon*

DOCTORATE IN MECHANICAL ENGINEERING

NOVA University Lisbon
January, 2022

Developments in Directed Energy Deposition Additive Manufacturing: In-situ Hot Forging and Indirect Cooling

To my grandparents

Acknowledgments

I could not have achieved this work alone, therefore I would like to address the following acknowledgements:

First off all, to my supervisor, Professor Telmo Santos, for his daily guidance and support throughout this work. His expertise, broad knowledge and self confidence, has inspired me to keep the constant search for knowledge and to improve myself every day.

To my co-supervisor, Professor Rosa Miranda, I would like to express my sincere gratitude for her valuable contribution and advice, for the endless patience while helping me with the materials science matters and for her knowledge and work methodology that always urged me to aim for more than just good.

I am also most grateful to Prof. João Oliveira for granting the realization of the X-ray diffraction synchrotron and Electron Backscatter Diffraction characterizations, and for his contribution with useful inputs and comments to this work, as well as his relevant collaboration in research publication.

To my dear friend Tiago Rodrigues, who accompanied me during this long journey, who helped me to maintain my sanity with his integrity and his pure and honest companionship.

To my friend Francisco Ferreira, with whom I disagree and argue the most, but that through these conflicts, taught me to respect and accept the various meanings of life.

To all my colleagues: Diogo Pereira, Miguel Machado, Patrick Inácio, Pedro Ferreira, Pedro Fonseca, Pedro Rendas, Werley Farias, Igor Felice who were great companions and with whom I shared not only great professional moments but also socializing moments that were vital and unforgettable.

To Mr. António Campos and Mr. Paulo Magalhães for their promptness in assisting workshop tasks, and for promoting and organizing the "patuscadas".

To my parents and sister, who throughout my life have given me the skills, strength, education and love that allowed me to be here today.

To the special one that accompanied me and supported me during this journey, it would have been almost impossible to make this journey without you.

Finally, to Fundação para a Ciência e a Tecnologia (FCT - MCTES) for its financial support via the PhD grant SFRH/BD/139454/2018

Part of this research was carried out at PETRA III at DESY, a member of the Helmholtz Association. The research leading to this result has been supported by the project CALIPSOplus having benefitted from the access provided within the framework of the NFFA-Europe Transnational Access Activity.

The preliminary tests of this work allowed the application of the Project Smart WAAM: Microstructural Engineering and Integrated Non-Destructive Testing, and the remaining work benefited from its funding from the European Institute of Innovation and Technology (EIT). This body of the European Union receives support from the European Union's Horizon 2020 research and innovation programme.

Abstract

Additive Manufacturing (AM) by Directed Energy Deposition-arc (DED-arc) is competing with other AM technologies due to its high deposition rate, ability to produce large parts with medium/high geometric complexity and low capital and running costs. However, residual stresses, coarse microstructures, and defects on parts, such as cracks and pores, may compromise in-service industrial applications and need to be overcome.

This work aimed to develop and validate two innovative process variants: one based on *in-situ* hot forging; and the other on temperature control, that is, indirect cooling of deposited material and hot forging.

The hot forging variant consisted of locally forging the deposited layer at high temperatures using low forces. The goal is to create an uniform plastic deformation zone along the layer, to promote grain refinement, reduce material anisotropy and collapse defects.

The variant based on temperature control consisted of cooling the hammer components and the shielding gas used to protect the molten pool, to increase the solidification rate and thus, prevent grain coalescence.

For this, dedicated DED-arc equipment was designed and manufactured with specific features for research. The effect of hot forging was analysed in detail on 316LSi stainless steel, and the feasibility of its application was verified in other relevant industrial materials. It was concluded that hot forging can induce dynamic recrystallization, increase nucleation sites and prevent epitaxial grain growth. Thus, it contributes to an overall refined and homogeneous microstructure with improved mechanical properties.

The developed cooling system lowered the average temperature of the nozzle and hammer during consecutive depositions. Cooling of the shielding gas had no major effect on the cooling rates and microstructure of the materials, however, it was observed that the hot forging changes the heat flow conditions of the part, promoting higher cooling rates.

Resumo

A tecnologia de deposição direta de energia por arco (DED-arc) tem competido com outras tecnologias de fabrico aditivo devido à sua elevada taxa de deposição, capacidade de produzir componentes de grandes dimensões com média/alta complexidade geométrica e baixos custos de implementação e funcionamento. Contudo, as elevadas tensões residuais, as microestruturas grosseiras, ou os defeitos do tipo poros, podem comprometer algumas aplicações industriais e necessitam de ser superados.

Este trabalho visou desenvolver e validar duas variantes inovadoras de processo DED-arc: uma baseada no forjamento a quente; e outra no controlo de temperatura.

A variante baseada no forjamento, consistiu em forjar o material depositado imediatamente após a deposição, utilizando baixas forças. O objetivo foi a produção de uma zona de deformação plástica uniforme ao longo de cada camada, para promover alterações microestruturais, nomeadamente o refinamento dos grãos e a redução da anisotropia.

A variante baseada no trabalho termodinâmico consistiu em arrefecer os componentes do martelo e o gás utilizado para proteger o banho de fusão, com o objetivo de aumentar a taxa de arrefecimento e assim evitar a coalescência dos grãos.

Neste sentido, foi concebido e fabricado um equipamento de DED-arc, com características específicas para investigação. O efeito do forjamento a quente foi estudado detalhadamente no aço inoxidável 316LSi, e foi verificada a viabilidade da sua aplicação noutros materiais relevantes industrialmente. Concluiu-se que o forjamento induz recristalização dinâmica, aumenta os pontos de nucleação e impede o crescimento de grãos epitaxiais, contribuindo para uma microestrutura globalmente mais fina, homogénea e com melhores propriedades mecânicas.

O sistema de arrefecimento desenvolvido baixou a temperatura do bocal e do martelo durante as deposições consecutivas. O arrefecimento do gás de proteção não teve efeito nas taxas de arrefecimento nem na microestrutura do material, contudo, observou-se que o forjamento altera as condições de fluxo de calor, promovendo taxas de arrefecimento maiores.

Contents

List of Figures

List of Tables

List of abbreviation and symbols

a	Acceleration [m/s^2]
A	Forged area [mm^2]
AC	Alternating current
AF	Acicular ferrite
AM	Additive manufacturing
BCC	Body centred cubic
CAD	Computer-aided design
CC-WAAM	Compulsive constriction wire and arc additive manufacturing
CMT	Cold metal transfer
C_p	Specific heat [$J\ kg^{-1}\ °C^{-1}$]
CTWD	Contact tip to work distance [mm]
DAC	Distance to arc centre [mm]
DAQ	Data acquisition system
DC	Direct current
DED-arc	Directed Energy Deposition-arc
$d\bar{\varepsilon}_p$	Equivalent true strain
EBSD	Electron backscatter diffraction
F	Resultant force [N]
F_{avg}	Average force during the impact [N]
FCC	Face centred cubic

F_F	Forging force[N]
F_f	Forging frequency [Hz]
FGM	Functionally graded materials
F_s	Forging step [mm]
G_L	Temperature gradient [°C]
GOS	Grain orientation spread
HAZ	Heat-affected zone
HF-DED-arc	Hot Forging Directed Energy Deposition-arc
HWAAM	Hot-wire arc additive manufacturing
I	Impulse [N s]
IC-DED-arc	Indirect Cooling Directed Energy Deposition-arc
ISO	International Organization for Standardization
L_w	Arc length [mm]
m	Mass [kg]
M-A	Martensite-austenite
MAG	Metal active gas
MIG	Metal inert gas
p	Pressure of the compressed air [MPa]
PAW	Plasma arc welding
PBF	Powder bed fusion
PBF-EB	Powder bed fusion electron beam
PBF-LB	Powder bed fusion laser beam
PBS-LB	Powder bed sintering laser beam
PDAS	Primary dendrite arm spacing
PF	Polygonal ferrite
Q	Heat transfered [J]
R	Solidification rate [$^oC\ s^{-1}$]
r	Pneumatic cylinders radius [m]
R_m	Hammer internal radius [mm]
SDAS	Secondary dendrite arm spacing [µm]
SEM	Scanning electron microscopy [µm]

SFE	Stacking fault energy
S-L	Solidus-liquidus
TIG	Tungsten inert gas
TRL	Technology Readiness Level
TS	Travel speed [mm/s]
TTT	Time-temperature-transformation
UTS	Ultimate tensile strength [MPa]
V	Average speed [m/s]
v_f	Final hammer speed [m/s]
v_i	Initial hammer speed [m/s]
W	Bead width [mm]
WAAM	Wire arc additive manufacturing
WFS	Wire feed speed [m/s]
WLAM	Wire laser additive manufacturing
YS	Yield Strength [MPa]
β	Angle of the arc half-length [º]
ΔP	Momentum variation [N s]
Δs	Distance [m]
δt	Impact period [s]
ΔT	Temperature variation [ºC]
Δv	Speed variation [m/s]
ε	True strain

1

Chapter 1
Introduction

1.1 Motivation

Additive manufacturing (AM) is being considered by both industrials and researchers as a process that is inline with digitalization of industry, since it allows the production of parts almost directly from a computational 3D modelling file (CAD), almost without the interaction of an operator. In fact, it allows for significant technological advances, in particular the production of unusual or complex component shapes that can be difficult or impossible to manufacture with conventional manufacturing technologies. With AM, there is no up-front tooling cost required to manufacture a specific/customized component, allowing the companies to supply low-demand parts quickly and cost-effectively. In particular, the freedom of customization allowed by AM makes the market-of-one a reality [1,2].

Among AM processes for metallic alloys, Directed Energy Deposition-arc (DED-arc) has gained the interest of the scientific community, due to its suitability to manufacture medium/large-sized components with substantial reduction in material waste.

However, across the wide range of AM techniques, several issues related to porosities, coarse microstructures with strong texture and anisotropy of mechanical properties fail to meet standards requirements [3].

To overcome the drawback identified in DED-arc some authors have developed new process variants, such as high-pressure inter-pass rolling, shot peening, laser shock peening, active cooling and heating systems, or substrate vibration mechanisms [4]. Most of these studies are scientific based and lack industrial feasibility, as the variants are over-complicated and hinder the system flexibility to produce complex parts, or require extremely complex and dedicated deposition systems. Thus, although these

variants allow for the mitigation of some typical DED-arc defects, their industrial implementation is being delayed.

This research work aimed at the development of a dedicated AM equipment, with a compact torch system with multiple integrated features, that can be easily coupled to any moving system and welding power source, to perform improved DED-arc at low costs.

1.2 Objectives

The main goal of this research was to develop improved technological variants of AM by Directed Energy Deposition-arc to enhance the microstructure and mechanical properties, and simultaneously reduce the formation of internal defects, such as porosity on the produced part.

To achieve these goals, two variants were developed, namely: *in-situ* Hot Forging Directed Energy Deposition-arc (HF-DED-arc) and Indirect Cooling Directed Energy Deposition-arc (IC-DED-arc). They are based on two distinct fundamental principles: first through mechanical work, in which it is intended to exploit the low forces required to forge the material in the viscoplastic regime; and secondly through temperature control, to reduce heat build-up on the part.

The development of this work imposed both technological and scientific challenges since it requires theoretical background, knowledge of the deposition process, equipment characterization, materials characterization, and the development of process variants not yet studied in additive manufacturing. Therefore, the specific scientific goals were:

1) Study the influence and applicability of the plastic deformation in visco-plastic regime in different materials, through the mechanical and metallurgical characterization of samples.

2) Dynamic and kinematic characterization of the hot forging variant.

3) Advanced material characterization to evaluate the influence of the hot forging in the microstructure of the materials.

4) Thermodynamic characterization of the indirect cooling variant.

5) Study the influence of the integrated cooling on the material cooling rates and on the microstructure of the parts.

To achieve these scientific goals, the following technological challenges were established:

1) Design, develop, and production of customised XYZ automated moving equipment to perform DED-arc.

2) Design, develop, and production of a dedicated DED-arc torch with both integrated hot forging and cooling mechanisms.

3) Perform the proof-of-concept of both the hot forging and cooling variants.

4) Accomplish a functional prototype at a Technology Readiness Level (TRL) = 5, i.e., a prototype capable of demonstration in an industrial environment.

1.3 Work performed

The starting point was a review of the state of the art of the DED-arc process fundamentals, shortcomings, and innovative technological variants that have been developed to improve the technology. It was identified that, most of these variants attain the necessary improvements at the expense of some characteristic features of the DED-arc process, namely: the high deposition rate and the ability to produce parts with medium/high geometric complexity.

To perform the experimental work without equipment constrains, a customized and versatile automated moving equipment with 3 degrees of freedom was designed and produced. A modified metal inert/active gas welding power source was coupled to the equipment.

An innovative concept of a multi-feed device torch wherein the different inputs are decoupled and can be controlled independently, was designed, produced and tested, a video of the system can be seen here: video.

For the variant based on mechanical work, a pneumatic mechanism was added to the torch to locally forge the material immediately after its deposition, that is, *in-situ* viscoplastic deformation regime at high temperature. For the variant based on indirect cooling, a coil of copper tube was placed around the gas nozzle. A refrigerated liquid was forced through this coil, extracting heat from the nozzle and consequently cooling the hammer components and the shielding gas, leaving the entire surrounding environment of the part at a lower temperature. Although several authors have already developed and tested different cooling variants, the variant developed in this work is the only one that is based on the cooling of the shielding gas.

The proof-of-concept of the DED-arc hot forging variant was performed, and it was possible to achieve constant plastic deformation throughout the deposition of one layer, and it was verified that the plastic deformation promoted microstructural changes, mostly grain refinement with almost no texture.

The dynamic and kinematic characterization of the forging mechanism was carried out using a high speed camera. The hammer speed, impact force and deformation rate, that occur during forging were determined for the 316LSi stainless steel and the 1070 aluminium alloy. Several samples were produced in which the pneumatic pressure

applied and the forging frequency were varied, to evaluate their influence on the average impact force.

The flow stress curves for 316LSi under forging conditions were obtained and compared to the impact force and true strain measured.

Additionally, it was validated the hot forging mechanism ability to produce multi-bead layers.

A detailed investigation of the effect of forging on the metallurgical and mechanical properties of stainless steel 316LSi was carried out. Forging forces of 17 N and 55 N were tested. Optical microscopy, microhardness tests, high-energy synchrotron X-ray diffraction, uniaxial tensile tests, fractography and electrical conductivity measurements were performed for the characterization of samples.

The feasibility of hot forging was also verified in other relevant industrial materials with different properties, namely: mild steel, stainless steel 410, aluminium 1070, Inconel 625, monel 400 and copper aluminium alloy. For each material, 2 set of samples with the same processing parameters were produced, one as-built and the other with hot forging. The microstructure, microhardness, and electrical conductivity of each sample were measured and analysed.

To characterize the Indirect Cooling Directed Energy Deposition-arc (IC-DED-arc) system, a thermal analysis using thermography and thermocouples was carried out, to evaluate the effect of the cooling system on the hammer components, on the accumulation of heat and cooling rates of the part. The materials used were the stainless steel 316LSi and the high strength low alloy steel (HSLA), aiming to evaluate the effect on the microstructure of materials with and without solid state transformation. The microstructure and microhardness of each sample were measured and analysed.

1.4 Major findings

This work shown that the hot forging variant of DED-arc has potential to refine the solidification microstructure, reduce porosity and reduce overall anisotropy, with small applied forces that require low stiffness equipment.

The dynamic and cinematic characterization of the forging system determined that, under the deposition conditions used for the stainless steel 316Lsi, forging occurs at a true strain rate of 660 s^{-1} with an average force of 1695 N, during 0.3 ms, which represents a stress of 371.7 MPa.

The characterization of the 316LSi samples showed that hot forging refines the solidification microstructure by reducing the grain size by about 50 %. A reduction in microstructural anisotropy was also evidenced by the analysis of the 2D Debbye-Scherrer diffraction rings, where the texture of the as-built microstructure is not observed

in the hot forged parts. The mechanical characterization shows improvements in the hot forged samples, from 360 to 450 MPa in the yield strength, and from 574 to 622 MPa in the ultimate tensile strength, while elongation to fracture has slightly reduced from 32 to 28 %.

Additionally, the as-built samples have mechanical properties that do not comply with the American Society for Testing and Materials (ASTM) A666-15 standard [5], while at the expense of a slight decrease in ductility, the values measured on the hot forged samples were between those specified by the standard for the AISI 316L cold rolled to its 1/16 and 1/8 hard conditions.

It was also seen that this new DED-arc variant can mitigate internal porosity present in the samples, having been observed that increasing the forging force, the morphology of the pores changes from spherical to ellipsoidal, and in some cases the pores are completely collapsed.

AM with hot forging of copper aluminium alloy was seen to limit the epitaxial grain growth, refine and homogenise the solidification microstructure, improving the mechanical strength, and reducing the material anisotropy.

From the feasibility study of hot forging application in other materials, it was concluded that, in most of the tested materials, hot forging has a positive effect on the metallurgical properties, refining their microstructure, which prevents the epitaxial grain growth and reduces the microstructural anisotropy, without creating any type of defects. In the aluminium 1070 alloy, the ability of the hot forging variant to reduce porosities was also confirmed, specially those located in the central region of the sample.

In the characterization of the indirect cooling system, it was observed that it is able to lower the average hammer temperature by 50 °C, resulting in less heat accumulated in the part. Moreover, it was seen that hot forging change the heat flow conditions of the part, promoting higher cooling rates, and lower base and peak temperatures during the successive thermal cycles.

Regarding the microstructural changes, in the 316LSi, with the indirect cooling variant, it was observed a reduction of the primary dendrite arm spacing on the hot forged samples, while in the high strength low alloy steel, the increase in the cooling rate induced the transformation of more austenite into martensite as this is an hardenable steel.

1.5 Document structure

This thesis is structured in 7 chapters.

Chapter 2 presents a literature review of Additive Manufacturing (AM) Directed Energy Deposition-arc (DED-arc). The process fundamentals are detailed, as well as a brief comparison between the different arc welding technologies that can be used to perform it. A detailed description of the DED-arc solidification structure and the most common defects are presented in section §2.4. The process variants that were developed to mitigate these shortcomings are described in section §2.5.

In chapter 3 a description of the equipment developed within the scope of this thesis is detailed. The development of a customized 3-axis movement system is described in section §3.2 and the development of the three prototype versions of the of the customized DED-arc torch in section §3.3. It is also described the results of the preliminary tests that allowed the validation of the innovative concepts introduced in the torch design.

Chapter 4 describes the process parameters introduced in the hot forging variant and the dynamic and kinematic characterization of the forging mechanism. Hammer speed, impact force and deformation rate during forging were calculated. It is also presented the validation of the hot forging mechanism ability to produce multi-bead layers.

Chapter 5 focus on the evaluation of the forging effect in different materials. A in-depth study of the effects of hot forging on the microstructure and mechanical properties of stainless steel 316LSi is presented, as well as a preliminary study of the hot forging feasibility on the mild steel, stainless steel 410, aluminium 1070, inconel 625, monel 400 and copper aluminium alloy.

Chapter 6 presents the results of the tests carried out, with the cooling system, to assess its effect on the part heat dissipation and cooling rates, as well as the structural properties of the deposited material.

Chapter 7 summarizes the main conclusions of this work and highlights future research topics.

1.6 Publications in international indexed journals (ISI/Scopus) and patents

The scientific output published, submitted, and under preparation for international indexed (ISI/Scopus) journals are listed in this section.

Journal papers published:

[1] Valdemar R. Duarte, Tiago A. Rodrigues, N. Schell, R.M. Miranda, J.P. Oliveira, Telmo G. Santos, Hot forging wire and arc additive manufacturing (HF-WAAM), Additive Manufacturing, 2020, 35, 101193.

https://doi.org/10.1016/j.addma.2020.101193

Impact Factor: 10.998 (https://www.sciencedirect.com/journal/additive-manufacturing)

[2] Tiago A. Rodrigues, Valdemar R. Duarte, R.M. Miranda, Telmo G. Santos, J.P. Oliveira, Current Status and Perspectives on Wire and Arc Additive Manufacturing (WAAM). Materials 2019, 12, 1121.

https://doi.org/10.3390/ma12071121

Impact Factor: 3.623 (https://www.mdpi.com/journal/materials)

Journal papers submitted:

[3] Valdemar R. Duarte, Tiago A. Rodrigues, N. Schell, R.M. Miranda, J.P. Oliveira, Telmo G. Santos, In-situ hot forging wire and arc additive manufacturing of CuAl alloy, Additive Manufacturing, Manuscript Number: ADDMA-D-21-03092

Impact Factor: 10.998 (https://www.sciencedirect.com/journal/additive-manufacturing)

Journal papers under preparation:

[4] Valdemar R. Duarte, Tiago A. Rodrigues, J. A. Avila, M. Miranda, J.P. Oliveira, Telmo G. Santos, Influence of the hot forging wire and arc additive manufacturing on the Inconel 625 microstructure.

Patents:

WIPO patent application (WO/2020/261233), SYSTEM FOR HOT FORGING WIRE AND ARC ADDITIVE MANUFACTURING. Date of patent application: 27/06/2020. Date of

patent publication: 30/12/2020. Inventors: Telmo Santos, Valdemar Duarte, Tiago Rodrigues, João Oliveira, Rosa Miranda

https://patentscope.wipo.int/search/pt/detail.jsf?docId=WO2020261233&_cid=P21-KWS55N-43560-1

2

Chapter 2
State of the art

2.1 Introduction

In this chapter, a literature review of Directed Energy Deposition-arc (DED-arc) is presented. The DED-arc process fundamentals are introduced, as well as a brief comparison between the different techniques that can be used to perform it. In section §2.4, the most common defects in parts manufactured by DED-arc are detailed as well as its origins, and the process variants developed to mitigate these defects.

2.2 Additive manufacturing

Additive Manufacturing (AM) is the process that builds an object through the deposition of layer upon layer, using data from computer-aided-design (CAD) software to selectively deposit the material of each layer. This technology allows the production of complex and customized parts in one stage, reducing many of the conventional processing steps. In some cases, however, other steps have to be introduced after deposition with specific objectives such as: surface finishing, dimensional correction or heat treatments, to mention the most frequent ones. Components with complex geometries can be manufactured with a significant reduction in the number of parts needed, and thus, the assembly of multiple parts is reduced or even suppressed. Additionally, parts can be produced on demand, which reduces the need for storing spare parts, and improve the lead time of the component. Due to these reasons, AM is an emerging technology that has captured the interest of multiple industries, particularly those that often use high-value materials [6].

Since DED-arc enables the reduction of raw material and wastes, and the production of relatively complex geometries without an increase in costs, it is a viable option for industries that produce large-scale metallic parts, such as moulds, automotive, naval, aerospace and aeronautical industries. Additionally, AM process does not require tooling and is more suitable than the conventional manufacturing processes for low-volume production.

In the aerospace/aeronautical industry, the geometric complexity of the parts produced with conventional processes lead to a high buy-to-fly ratio (i.e., the mass ratio between the bulk material and the final component), and thus, a large amount of material is wasted, increasing the part cost. The aerospace industry has shown a great interest in AM processes since it is possible to produce near net-shaped parts and reduce the buy-to-fly ratio, which, in some particular cases, can get close to a 1:1 ratio. Additionally, the freedom in designing components, may also result in weight reduction.

In 2015, the publication by ISO of a family of standards on additive manufacturing ISO 52900 addressing the terminology, main process categories, part types and feedstocks, testing and data management for different materials allowed to have a common ground for communication and training in AM [7]. Table 2.1. depicts a summary of the AM processes for metallic materials.

Table 2.1 - Additive manufacturing process categories (adapted from: [7])

Metallic materials		
Process	Powder bed fusion (PBF)	Directed energy deposition (DED)
Feedstock	Powder	Wire
Technique	- Powder bed fusion laser beam (PBF-LB) - Powder bed fusion electron beam (PBF-EB) - Powder bed sintering laser beam (PBS-LB)	- Wire arc additive manufacturing (WAAM) or (DED-Arc) - Wire laser additive manufacturing (WLAM)

2.3 Directed Energy Deposition-arc

2.3.1 Process fundamentals

Currently, the most used metal additive manufacturing processes based on fusion are the powder-bed systems that use either laser or electron beams as heat sources. The interest in these processes is mainly due to the high precision dimensional tolerances that enable the production of very detailed parts with complex geometry and good surface finishing [8]. However, its deposition rate of approximately 1 kg/h is considerably low when compared to the 6 kg/h of the Directed Energy Deposition-arc (DED-arc) processes, which increases the lead time [9]. Moreover, the use of feedstock material in the form of powder increases the process susceptibility to the formation of defects such as pores and cracks, which can hinder the mechanical properties of the parts.

Directed Energy Deposition-arc uses an electric arc as the heat source and a solid wire as the feedstock material. Though, at the expense of precision and geometric complexity, when compared with the laser-based powder additive manufacturing, DED-arc has a wide range of applications, lower cost and the ability to form large parts. Additionally, it improves the raw material utilization and shorten product manufacturing cycle [10]. Most industrial applications, require machining post-processing of the functional surfaces, even in the parts manufactured by powder bed techniques.

Directed Energy Deposition-arc techniques are those that use the fundamentals of the arc-based welding process, such as metal active gas (MAG), metal inert gas (MIG), tungsten inert gas (TIG), or plasma arc welding (PAW), to melt the wire feedstock and deposit the material layer-by-layer until the final product is built.

Both MIG/MAG, TIG, and PAW processes use an electric arc as a heat source, which is the transmission of electric current between a pair of conductors through a gas that gets ionized when passing electric current.

In the TIG welding process, an electric arc is established between a non-consumable electrode and the workpiece. To add the filler material an external wire feeding unit is necessary. The non-consumable electrode is usually composed of tungsten with small additions of other elements, such as thorium, zirconium, cerium, or lanthanum, that gives it specific properties for different applications. It uses inert gases to sustain the arc and to protect the molten pool from atmospheric contamination. To perform additive manufacturing based on TIG, the welding torch can be attached to a movement system with 3 or more axes. However, the relative position between the material feeder and the torch is a critical parameter to ensure consistency of bead geometry, that should be maintained constant throughout the deposition, which in the case of the production of highly complex parts requires additional automation to rotate the wire feeder according to the deposition direction.

The PAW process starts with a pilot arc that is established between the non-consumable electrode and a copper nozzle, both placed within the torch, usually by applying a high-frequency voltage. When the torch is brought near the workpiece, the arc is then transferred from the electrode to the workpiece. The main difference from the TIG technique is that the electrode is recessed in the welding torch and the arc is forced to pass through an orifice in the copper nozzle, which constricts the arc and thus increasing its energy density. This causes the arc to achieve higher temperatures (around 15000ºC [11]) than the ones achieved in TIG or MIG/MAG (around 5000 ºC [12]), therefore, the PAW torches require active cooling. The addition of the filler material must be performed as in the TIG process.

Unlike MIG/MAG and TIG, the PAW torches have two gas inputs, one for the plasma gas, that is ionized, and the other for the shielding gas, which surrounds the arc and protects the molten pool. Usually, the same gas type is used in both, but separation is required since the flow of the plasma gas is an important parameter for arc stabilization and may differ from the flow of the shielding gas required to promote effective protection of the molten pool.

The procedures to perform AM based on plasma are very similar to the ones based on TIG. However, due to the narrower arc, special attention must be given to the alignment of the filler material with the plasma column, requiring a more rigid movement system that is able to ensure this alignment.

The MIG/MAG process uses a continuous wire feed while the electric arc is established between the wire and the workpiece, which generates heat and creates a weld pool that contains both. The difference between MIG and MAG is related to the shielding gas. In MIG only inert gases, such as, argon and helium, are used to prevent the exposure of the molten pool to the atmospheric air, while in MAG, the shielding gas is composed of active gas, such as carbon dioxide, hydrogen, oxygen or mixtures containing both inert and active.

Unlike the other techniques that use non-consumable electrodes, in MIG/MAG welding is commonly used in reverse polarity with the wire connected to the cathode (+) and the workpiece connected to the anode (-). Since most of the heat generated by the arc is located at the positive pole, the MIG welding is capable to achieve high wire melting rates.

Due to the continuous wire feed, the rate at which the wire is melted in the arc must match the wire feed speed. To achieve this control, the MIG process uses a power source with a constant voltage dynamic characteristic, that provides direct current. This constant voltage characteristic is what forces the arc length to be maintained constant during the deposition. In detail, this means that if arc length increases the arc voltage also increases, and thus the arc current decreases. Since the wire melting rate is mainly determined by the current it also decreases, and the tip of the consumable wire move closer to the molten pool. If the arc length decreases the opposite occurs, resulting in a constant arc length and wire melting rate. This characteristic is also known as the self-adjusting arc.

The transition from MIG/MAG welding to additive manufacturing can be as simple as coupling the welding equipment to a movement system with 3 or more axes. Often a robotic arm is used to provide the desired movements. Figure 2.1 shows schematically the fundamental features of arc welding process.

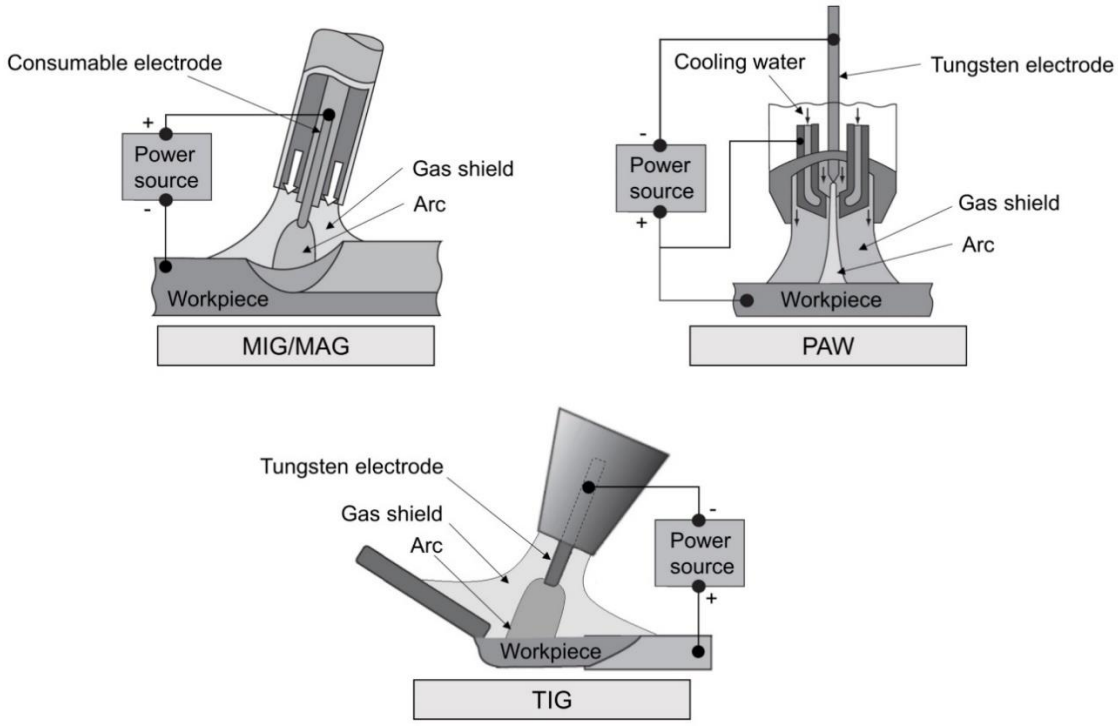

Figure 2.1 - Fundamental features of the MIG/MAG, TIG, and PAW processes (adapted from: [13])

Although all these welding processes fit within the same AM category, they have very different characteristics that make one preferred over the others depending on the application in question.

Among the three welding process, PAW is the one with the highest energy density, which allows deposition at higher travel speeds, narrower deposition bead and therefore, high part accuracy [14]. However, this technique is by far the one that requires the most extensive capital expenditure, not only in the electrical supply sources but also in the wire supply system. Because of its high energy density, and consequently a very narrow arc, the entire system for feeding the consumable wire must be very rigid and precise in its position relative to the arc.

In regard to arc energy density, TIG and MIG/MAG are very similar, having a lower density than the one achieved by PAW. Therefore, the deposited beads are larger which reduces the process ability to produce fine detailed parts.

As a comparison, the typical width of a bead deposited by PAW varies between 2 and 7.5 mm [15–17], while for the TIG and MIG/MAG processes the width of a bead varies between 3.9 and 11 mm [18–20].

Regarding the equipment, the cost of a TIG power supply is lower than those of the PAW, but a high rigidity system is still needed to guarantee the correct supply of the consumable wire, and therefore the overall complexity of the deposition system increases as well as its cost.

MIG/MAG is, whenever possible, the process of choice, due to its simplicity of implementation and easier tool paths, which comes from the fact that the supply wire is the consumable electrode itself and it is coaxial with the torch [21]. Additionally, it is also the arc welding process that has the highest deposition rate, that can surpass the 6 kg/h [9].

However, the characteristics of conventional MIG/MAG process are not satisfactory for processing certain materials such as aluminium, magnesium and titanium alloys, as the deposition instability gives rise to excessive spatter, internal defects, and consequently a greater surface roughness. In this regard, the Fronius Cold Metal Transfer (CMT), which is a modified MIG/MAG process that relies on controlled dip transfer mode, produces beads with superior surface quality, lower thermal heat input, controlled droplet transition and a substantial reduction in the amount of spatter generated [22]. Because of this, the process has been widely used in research [23].

2.4 Common shortcomings in DED-arc

As in other conventional manufacturing processes, the DED-arc parts are also susceptible to the appearance of defects. The presence of defects inside a component, as well as the development of a deleterious microstructure, dictates its performance and behaviour, which affects significantly the mechanical properties and can lead to catastrophic failure.

Therefore, it is important to know which types of defects may occur in a component produced by DED-arc and which are the mechanisms responsible for their occurrence, to take the necessary precautions to avoid the formation of these defects. Due to the fundamental similarities between the DED-arc and welding processes, the formation of defects is also similar in both processes, which represents a great advantage, because there is a vast knowledge on defects formation as well as active or passive ways to avoid their formation in welding technology and metallurgy.

Defect formation is not only related to the deposition technique, but is also material-dependent, as some materials are more prone to one type of defect than others. As an example, aluminium alloys easily tend to form porosities more frequently than other materials, due to its affinity to oxygen and hydrogen.

The main DED-arc shortcomings are presented below, as well as their formation mechanisms and practices to avoid their formation. Moreover, a review of the most common solidification structures in DED-arc is presented in subchapter 2.4.1, since this is responsible for several factors that can determine the application and in-service performance of the component, such as mechanical properties, fatigue lifetime and defects formation.

2.4.1 Distortion and residual stress

One of the main problems related to the production of parts using additive manufacturing technologies is the inherent residual stresses. The appearance of residual stresses is also a very common phenomenon in arc welding, and since the DED-arc is based on arc welding technology, residual stresses are formed similarly to those observed in welding.

In arc welding, residual stresses occur when a part is subjected to non-uniform thermal fields [24], that promote different expansion and shrinkage of the part under constrain.

According to Withers and Bhadeshia [25], these stresses can be separated by their characteristic length into 3 categories. Most of the residual stresses generated during arc welding are placed into the Type I category, which are the long-range stresses that equilibrate over macroscopic dimensions. These stresses can be estimated using continuum models where the polycrystalline or multiphase nature of the material is often disregarded. Type II residual stresses are the ones that equilibrate within several grain

dimensions. And the Type III stresses only exist over atomic dimensions and achieve equilibrium within the same grain.

The effects that the type I residual stresses can have in a part depends on their magnitude. If the residual stresses are less than the yield strength of the material, the component presents only a geometric distortion in an elastic regime, which can be reversed through a post-heat treatment. When the residual stresses are locally higher than the yield stress of the material, it may deform plastically, which makes it, in most cases, irreversible. In cases where the generated residual stresses surpasses the ultimate tensile strength of the material, permanent plastic deformation and the formation of cracks are expected. In either case, the formation of residual stresses throughout the material deposition leads to the loss of geometric tolerance and may promote delamination between layers [26].

Several authors have studied the residual stresses in DED-arc by both experimental and simulation methods. Ding et al. [27], worked with a 3D thermo-elastic-plastic finite element model to simulate the deposition throughout DED-arc, aiming to predict the stress distribution and distortions. The theoretical results were compared with experimental tests in which the stresses were measured by neutron diffraction strain scanner ENGIN-X. The results show that the residual stresses are practically uniform across the deposited wall where the following layers are little influenced by the stress field present in the previous layers. On the other hand, it is along the vertical direction that the longitudinal residual stresses are most exhibited, describing almost a straight line with a negative slope, being these the ones responsible for the part wrapping. In detail, next to the substrate, longitudinal residual tensile stresses are present, while at the top of the part, next to the last layers, compression stresses are present, as shown in Figure 2.2. In addition, other authors have also measured the distribution of residual stresses in manufactured wall structures and have reached the same stress distribution where the magnitude of the stresses can reach up to 70 % of the material yield strength [28–32].

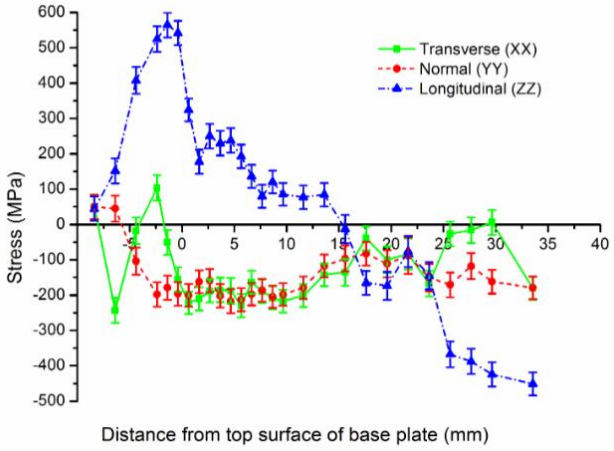

Figure 2.2 - DED-arc residual stresses in the longitudinal, normal and transverse directions [30]

There are several procedures and techniques to mitigate and/or reduce the formation of residual stresses. The first form of intervention to control residual stresses is through the welding parameters [33], (such as current, voltage, travel speed, interlayer dwell time, etc.) as these influence the thermal cycles to which the part is subjected and therefore the formation of residual stresses [34]. However, there is still a flaw concerning this area of research, mainly due to the difficulty of measuring these stresses accurately.

Residual stresses can also be controlled by an adequate sequential path planning, particularly in the production of parts with complex geometry. M P Mughal et al. [35] did a finite element-based three-dimensional analysis to study the structural effects of deposition patterns in DED-arc, and concluded that the deposition strategy has a considerable effect on the extent and magnitude of residual stresses. Similarly, Chi Zang et al. [36], compared the residual stresses of two parts with the same geometry manufactured with different deposition paths and concluded that, for each part, specific path planning strategies are necessary for achieving high-quality DED-arc parts with both optimal outline accuracy and residual stress levels.

Qian Chen et al. [37], proposed a continuous scanning path optimization method where the path design takes into account the thermal cycles induced into the part and aims to mitigate or minimise the residual stresses. Although this technique can be used transversely in several AM processes, it was just tested virtually and not physically to date.

Several variants of the DED-arc process have been developed recently aiming at mitigating residual stresses. These variants are further detailed in section 2.5.

2.4.2 Cracks and delaminations

Cracks and delaminations are very common defects in powder bed AM processes such as powder bed fusion laser beam (PBF-LB) and electron beam (PBF-EB), but they can also occur in DED-arc in specific conditions.

Delamination is the separation of adjacent layers within a part and may be caused due to insufficient re-melting of the previously deposited layer, resulting in a weak or even non-existent bond between layers. This type of delamination can be avoided by changing the process parameters aiming to increase the heat input and therefore to ensure a good bond between successive layers. The preheating of the substrate must also be considered when delamination defect occurs, as it raises the general temperature of the part, and therefore increases the percentage of re-melting of the previous layer [10].

Another cause of delamination is the formation of cracks, that together with residual stresses can easily propagate and cause the layers to separate totally or not.

The conditions in welding are physically different from those of DED-arc, particularly, in DED-arc there is no physical constraint while in welding the parts to be joined are

constraining the welding bead, which influences the development of the residual stress and therefore, the propagation of cracks. Despite this difference, the formation of cracks follows the same principles in both processes, as it depends on the process parameters and the material composition. In some cases, cracking may be unavoidable. There are different mechanisms from which cracks may form during DED-arc, but they can be categorized into two major groups, hot cracking, and cold cracking.

Hot cracks appear at high temperature due to the segregation of alloy elements within the grain boundaries with the formation of low melting temperatures liquid films.

In aluminium alloys such as Al-Mg hot cracking usually occurs when the low melting point constituents are rejected by the solidified structure, which results in the formation of a thin film of liquid between the grains. If this film cannot be fed successfully from the weld pool, it does not withstand the contraction strain and a crack is formed [17,28].

Another material that is also susceptible to hot cracking, is austenitic stainless steel, but in this material, the cracking occurs due to the segregation in the grain boundaries of impurities such as, phosphorus and sulphur, or alloying elements such as silicon and niobium. These segregations, usually have a fragile behaviour to tensile stresses and originate cracks due to the shrinkage of the material during solidification [29].

Cold cracking, is referred to cracks that form after the solidification is complete, during the cooling of the part, or even some time after the deposition of the material. The formation of this type of crack is mainly associated with the presence of hydrogen in the deposited material and/or the presence of residual stresses in the part. The presence of hydrogen causes localized embrittlement of the deposited material, thus the material loses its ductility properties, and consequently cracks appear [30]. This type of cracks is more common in materials with high hardness, such as high-strength steels [31,32].

The formation of cracks is mainly material dependent, and although it can be minimized by adjusting the process parameters, in most applications it is only possible to eliminate through the adjustment of the deposited material composition.

When depositing the combination of different materials the susceptibility to cracking and delamination increases, as the dissimilar metals have differences in their solubility and/or chemical reactivity, intermetallic phases may form [28].

Whereas other defects within the interior of the part can usually be mitigated with post-processing, the delamination is usually macroscopic and cannot be repaired by post-processing [10,33].

2.4.3 Porosity

Porosity is the presence of cavities within the deposited material and is considered a defect as it affects negatively the mechanical properties of the part, in particular, its elongation and fatigue strength [38], and therefore needs to be minimized.

The formation of porosities is usually classified as raw material-induced or process-induced. In DED-arc there are two raw materials, the wire feedstock and the substrate. In both, the presence of impurities, such as moisture, grease, and other hydrocarbon compounds, can be absorbed by the molten pool, causing porosities and/or inclusions [33]. Thus, cleaning the raw material is important to minimize the formation of porosities during the deposition.

E. M. Ryan et al. found that the primary influence on porosity in AA2319 is the wire batch used, and it is mainly due to the surface finish and cleaning, where the wire with a good surface finish resulted in much lower porosity than the wire with a poor surface finish. The reason is that the poor surface quality may affect the arc stability, and act as sites of contamination which increases the amount of hydrogen introduced in the molten pool. Moreover, when comparing the wire batch influence to the process parameters and wire composition both have a neglectable influence on the porosity. Similar results have been achieved for the ER4043 aluminium wire [39].

During the deposition of the material, several factors can lead to the formation of porosities. Starting with the process parameters, a set of process parameters that promote an unstable and violent arc may lead to an exaggerated agitation of the molten pool, which in turn induces the creation of voids. The excess of shielding gas flow rate can also lead to the inclusion of the shielding gas within the solidified metal, and contributes to an unstable molten pool.

One of the main causes for the appearance of porosities is the absorption, by the molten pool, of atmospheric gases, such as nitrogen, oxygen, and hydrogen. Particularly, in the deposition of aluminium alloys, the main cause for the appearance of porosities is the absorption of hydrogen by the molten pool. The capacity of the aluminium to dilute the hydrogen is much higher when it is in a liquid state and drastically reduces during solidification, which causes the hydrogen to be rejected but becomes trapped inside the solid material, forming pores [40].

Although there are several factors that can lead to the formation of pores, they are usually interconnected. Therefore, to obtain the least possible amount of porosity it is required that all the parameters are correctly parameterized. Because of this, porosity represents a recurring problem, for which it is difficult to present a single solution able to solve it in any situation.

For example, the increase in heat input, in some situations, can be beneficial for the reduction of porosity, as it allows the deposited material to be liquid for a longer time,

consenting gases that are present to be expelled from the molten pool [41]. On the other hand, when welding aluminium, the increase of the heat input represents an increase in the hydrogen solubility of the liquid aluminium, promoting the formation of pores [42].

It is well known that, among the various welding modes used for the deposition of aluminium alloys, cold metal transfer (CMT) is the one that creates less porosity, due to its short and stable arc and high level of control in drop detachment.

Maider Arana et al. [43], studied the influence on the porosity of the type and flow rate of shielding gas, as well as different deposition strategies, during the deposition of Al-Mg with the CMT technique. The two deposition strategies used were hatching and circling. The results demonstrated that the deposition strategy influences the porosity, however, the correct selection of type and flow rate of the shielding gas obliviate, in most scenarios, the effect of the different deposition strategies. Yurri et al. [44] had also assessed the influence of the switchback deposition strategy (moving cyclically the torch forward and backwards). The authors had achieved less porosity (between 3 and 19 % less) in the samples produced with this strategy and claim that the switchback movement may stir the molten pool in such a way that facilitates the escaping of the trapped gases.

2.4.4 DED-arc solidification structure

Although microstructure, per se, is not considered a defect, the solidification process is responsible for determining certain properties of the material and can also be the source of defects such as residual stresses, distortions and cracks. Since DED-arc uses the same heat source as electric arc welding processes, the typical structure of DED-arc components is very similar to the one found in multipass welding. However, there are occasions when the microstructure of DED-arc differs from traditional arc welding due to the repeated thermal cycling, heat flow, and the shell geometry typically used in DED-arc. Therefore, it is important to understand the fundamental principles and the variables that allow the control of the solidification process.

Nucleation and solidification

The microstructure of a material depends, among other things, on its composition, solidification process and solid state phase transformations. To start the solidification process, it is necessary that the nucleation of solid phase occurs within the liquid phase and it can occur either homogenously or heterogeneously. In the solidification of pure metals the homogenous nucleation is more frequent. When the liquid is cooled below its equilibrium melting temperature (undercooling), the liquid become unstable and the atoms slowly start to bond together forming a crystalline structure. However, in most metallic materials the homogeneous and heterogeneous nucleation occur simultaneously, and particularly in fusion welding the heterogeneous nucleation is predominant. To occur heterogeneous nucleation the presence of a solid substrate or a

foreign particle (such as an oxide, nitride, sulphide, etc.) is required to initiate the formation of a crystal from it. Additionally, these foreign particles are usually stable above the melting temperature of the material, and therefore less or no undercooling is required to promote the nucleation [45].

In fusion welding, the dominant form of heterogeneous nucleation is the one that occurs from the solid substrate and it requires low undercooling or other driving forces. Therefore, solidification initiates immediately after the material cools below the liquidus temperature on pre-existing solid grains [45]. Grain growth develops by epitaxy, that is, the crystallographic orientation of solidified grains is the same of the subjacent grain that is best oriented along the thermal flow directions and perpendicular to isothermal lines. This results in a continuation of the crystallographic orientation that is maintained throughout multiple layers.

It is also possible to artificially promote heterogeneous nucleation through the addition of particles, with a melting point higher than that of the alloy to be deposited, that act as nucleation sites, this process is also known as inoculation. In DED-arc some studies have been performed where inoculating particles are added directly into the molten pool. In general, the results show a more refined and heterogeneous microstructure, which is a big step towards the mitigation of the anisotropic properties typical of the DED-arc parts [46–49].

The growth phase begins after nucleation, which can occur in different modes. These modes determine the morphology of the solidified material at the Solidus-Liquidus (S-L) interface, which for materials without solid state phase transformations, is maintained during the cooling down to the room temperature, and therefore forms the morphology of the grains observed in metallographic analysis. In the solidification of metals, the possible modes are: planar, cellular, cellular dendritic, columnar dendritic and equiaxed dendritic. Although they also depend on other parameters such as material composition, the solidification mode is mainly determined by the combined effect of the solidification rate (R) and the temperature gradient (G_L) as shown in Figure 2.3.

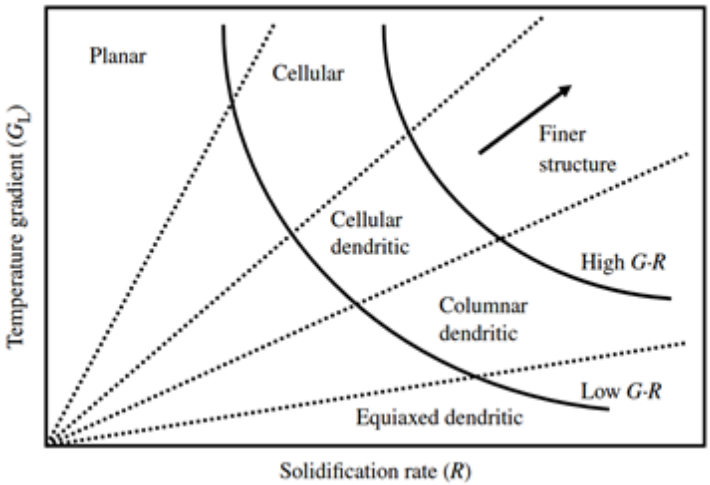

Figure 2.3 - Effect of temperature gradient and solidification growth on solidification mode [45]

Under the solidification conditions usually found in fusion welding and DED-arc the most common modes are the cellular, cellular dendritic and columnar dendritic. The planar morphology requires that a very slow growth rate is maintained, which is not stable in the solidification of alloys, and therefore, the planar interface quickly breaks down into a cellular or cellular dendritic growth. At the other end, the equiaxed dendritic mode requires a large constitutional supercooling and a very shallow temperature gradient, a condition that is usually impossible to achieve in fusion arc welding.

The material local cooling rate can be plotted as the product between R and G_L, and it is the parameter that mostly influence the size of the solidification structure (grain size) in the additively manufactured components [50]. Through the analysis of Figure 2.3, it can be verified that, if the ratio between these two parameters is maintained constant, an increase in the cooling rate does not change the solidification mode, but refines the microstructure. Finer structures are obtained with higher cooling rates, due to the shorter growth times are available for the growth of the grains, and the opposite is also true. The quantification of this structural feature is normally obtained by measuring the distance between the axial centre of adjacent cells or dendrites. Depending on the material's cooling rate, it can vary from several millimetres to a few microns.

In conventional DED-arc the cooling rate decreases as the part height increases, due to the heat accumulated in the previously deposited layers and the constraint that it imposes to the heat flow. Therefore, the grain structure becomes coarser in the upper layers than those in the lower layers [6].

The direction in which the grains grow tends to be perpendicular to the isothermal lines and opposite the direction of the temperature gradient. In DED-arc the maximum heat flow direction is perpendicular to the fusion line of the molten pool pointing towards the previous layer [51], and as explained before, the re-melting of the previous layer induces the epitaxial grain growth at the solid-liquid interface in a cellular or dendritic solidification

mode [52]. The combination of these factors result in a continuation of the crystallographic orientation of grains from previous layer that grows by epitaxy, so large grains form crossing multiple layers. This phenomenon is particularly visible in the Ti6Al4V alloy, since due to its composition it preferably solidifies in planar or columnar modes, as showed in Figure 2.4 b).

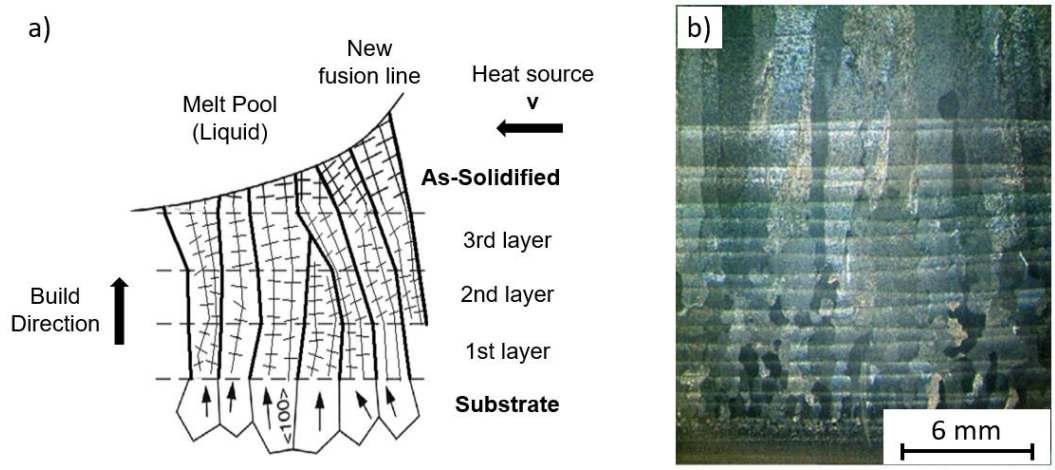

Figure 2.4 - (a) Schematic representation of the directional solidification pattern of epitaxially columnar grain growth during DED-arc [44], (b) actual micrography showing the columnar grains formed during DED-arc of the Ti-6Al-4V [53]

In detail, the direction of grain growth in AM can slightly deviate from the vertical direction depending on the deposition strategy. Figure 2.5 shows a comparison between a unidirectional and bidirectional deposition pattern, and it can be observed that the grain tends to deviate to follow the direction of the deposition.

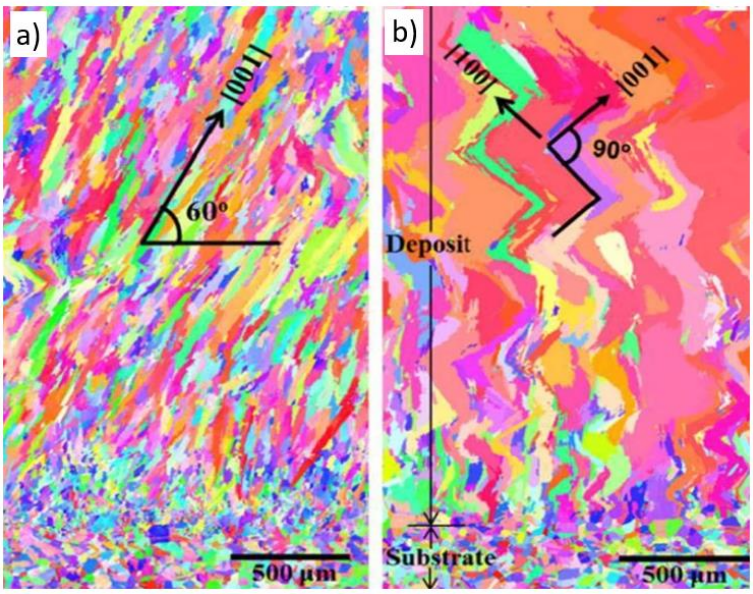

Figure 2.5 - Electron backscatter diffraction (EBSD) characterization of the longitudinal plane of a directed energy deposition of IN718 with (a) unidirectional and (b) bidirectional deposition strategy [54]

Several authors have already demonstrated that this large columnar grains oriented with specific directions, cause anisotropy of the mechanical properties in DED-arc, particularly in the material ductility which is particularly detrimental for applications involving multidirectional stresses [56–60].

In the coarse columnar grain microstructure of the Ti-6Al-4V, the tensile strength and ductility properties decrease when tensions are applied perpendicular to the grain boundaries (i.e. aligned with the horizontal direction). In this case, and due to the large size of the grains, the crack easily propagates through the grain boundaries promoting premature failure, contrary to what occurs in a homogeneous and refined microstructure where the grain boundaries act as a barrier for the propagation of dislocations [58].

Non- heat and heat treatable materials

Some of the metallurgical processes that define the final structure of the component also occur in the solid state, while it is cooling to room temperature, including recrystallization, grain growth, phase transformations, among others. Thus, not only the structure of the material that is remelted during the deposition of the next layer is affected, but also the adjacent material whose temperature is increased above a threshold value (within the solid state) that activates these processes. This portion of material is commonly known as the heat-affected zone (HAZ), and the extent of these processes can change the microstructure, and therefore, the properties of the deposited material.

The materials are usually divided into two categories: non-heat treatable and heat treatable alloys.

The non-heat treatable alloys are those that achieve their properties mainly through solid solution strengthening or strain hardening that is applied in process such as forging, rolling, extrusion, cold drawing, etc. Most of the pure metals, like aluminium, copper, platinum, molybdenum, tungsten and tantalum belong to this category. Moreover, alloys with small additions of alloying elements usually exhibit single phase microstructures, and these are also non-heat treatable.

Among the aluminium alloys, those that are non-heat treatable are the 1xxx, 3xxx, 4xxx and 5xxx series Al alloys, as the strength properties of these are initially obtained by alloying the aluminium with other elements, and a further increase in the strength of these alloys can only be achieved through strain hardening.

Other commonly used materials in DED-arc are the austenitic stainless steels 304L and 316L [61] and they are also considered non-heat treatable, since strength improvements obtained by other methods than cold working are usually negligible.

Some studies have shown that the austenitic stainless steels produced by DED-arc exhibit tensile properties above the annealed base metal properties. However, they are also accompanied with a drastic decrease in ductility. The observed strengthening effect

becomes particularly evident in depositions with low heat input (high cooling rate) since it is caused by the refined microstructure that is formed during deposition, combined with the presence of retained delta-ferrite [59,62–64], that occurs due to the inhibition of the solid state phase transformation of the delta ferrite (bcc) to austenite (fcc) during cooling [61].

Opposing to what was described above, the heat-treatable alloys are those that can achieve their properties through the application of heating and cooling operations in its solid-state. In addition to heat treatments most of these alloys can also improve their properties through strain hardening. Among many others, some of the most frequently used materials in DED-arc that are considered as heat treatable are the aluminium 2xxx, 6xxx and 7xxx alloys, high strength steels, nickel-based superalloys, titanium alloys, martensitic stainless steels, etc [6].

These alloys are much more complex to process by AM techniques than the non-heat treatable alloys, since, depending on the material composition, there are several metallurgical processes that can occur during cooling. Additionally, in materials like maraging and tool steels, these metallurgical processes are, usually, very sensitive to the cooling rate, that can be controlled through the process parameters. Therefore, the process parameters have a great influence in the final mechanical properties of the deposited material, making it difficult to achieve uniform strength properties [65–68].

Although there is a vast knowledge of materials science that allows the identification and prediction of phase transformations through the use of phase diagrams and Time-Temperature-Transformation (TTT) diagrams, the wide range of parameters of the AM processes, as well as the part geometry itself, induce highly complex thermal cycles on the deposited material. The microstructure of a part can differ from one zone to another, depending on the thermal cycles that they have been through, making it very difficult to predict the phase transformations or other metallurgical process that can occur after solidification.

2.5 DED-arc Process Variants

2.5.1 Cold and hot-work based variants

One of the main DED-arc variants is based on high-pressure inter-layer rolling and was developed at Cranfield University Welding Engineering Research Centre [69]. The process is schematically depicted in Figure 2.6 and consists of imposing a load of up to 100 kN through a roller that is travelling over the already deposited layers. The load is applied onto a layer after it cools down to near room temperature, to promote plastic deformation, recrystallizing the microstructure during the following pass and, therefore, reducing the grain size and improving the mechanical properties of the material.

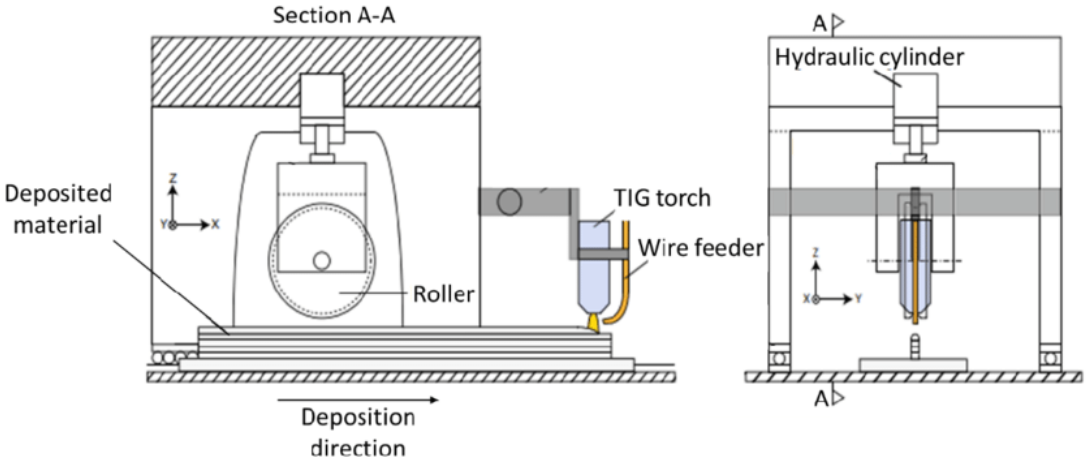

Figure 2.6 - Schematic diagram of high-pressure inter-layer cold rolling

The first studies in which this variant was used were performed with the Ti-6Al-4V titanium alloy and showed that inter-layer rolling in DED-arc induced prior β grain refinement, thickness reduction of the α-phase lamellae, and an overall modification of the microstructure from columnar to equiaxed. Rolling loads of 50 and 75 kN were tested and it was observed that increasing the applied load promoted more recrystallization, and exhibited smaller prior β grains than the ones observed for lower rolling loads [70].

A complementary study on the microstructure of the inter-layer rolled titanium has showed, through electron backscatter diffraction (EBSD) analysis, that the normally coarse centimetre-scale columnar β grain structure could be refined down to less than 100 μm, and that both the β and α phase textures were substantially reduced to close to random [71].

In other studies, it was also verified through neutron diffraction and the contour method that in the DED-arc of Ti, the inter-pass rolling promotes grain refinement without negatively influencing the development of residual stresses [72], and in some cases, it has successfully reduced the longitudinal residual stress of the parts [73].

Another advantage of rolling operation is the reduction of porosity on the DED-arc parts, particularly in the deposition of the aluminium alloys, where the porosity normally restricts their use in most applications. It has been reported that with the increase of the rolling load (up to 45 kN) the inter-layer rolling is able to gradually flatten the pores to the point where they are not detected by optical microscopic. However, when the inter-layer rolled samples are subjected to a post-heat treatment the re-growth of the porosities was observed, suggesting that some of the porosity were not completely annihilated during rolling [74].

Other studies have also demonstrated that the inter-layer cold rolling has a positive influence on the mechanical properties of the DED-arc deposited aluminium alloys, where the microhardness and strength properties (UTS and YS) were enhanced with the increase of the rolling loads [75,76]. Additional, this DED-arc variant can control the residual stress in the DED-arc of 2319 aluminium, and eliminate the distortion of the part [77].

Results such as improved mechanical properties, grain refinement, and random texture were also obtained in INCONEL 718 alloy [78,79] and unalloyed tantalum [55].

Additionally, cold rolling has also been used to control the accuracy of the parts by applying a roller on the side of the walls, and consequently, improve the surface finish of the final part geometry [80,81].

Since this is a technique based on cold working, it is expected that similar results are obtained in other materials that may also be susceptible to this type of mechanical treatment. One of the main aspects that need to be considered when applying the inter-layer rolling is the need to ensure that the depth of the plastic deformation is big enough to not be fully remelted when the deposition of the next layer occurs. Nevertheless, this process variant has some limitations, such as the need for a system with high rigidity that is capable to withstand high loads (up to 100 kN). Regarding its application at an industrial level, this variant may present some constraints in the production of parts with high geometrical complexity as it requires additional path planning for the roller, and, since it is carried out at low temperatures, it requires a dwell time between layers sufficient big for them to cool down, which may represent a significant reduction in the productivity.

Other studies, where the concept of cold working is also used in DED-arc technology, have also been carried out. In an attempt to complement or replace the inter-pass cold rolling technique J. R. Hönnige et al. [82] have applied an inter-pass machine hammer peening on DED-arc parts, claiming that it offers greater flexibility and speed than the rolling. In this study, the plastic deformation was applied in both the top surface of every four layers and the side surface of the built wall. The authors have studied in detail the effectiveness of machine hammer peening on the grain refinement of Ti-6Al-4V DED-arc. The results show that when hammer peening is applied to the top surface of each

layer, the deformation depth was approximately 0.5 mm, and when the next layer is deposited, the depth of re-melting experienced by each layer is 0.7 mm [83]. Although it may suggest that the remelting of the previous layer eliminates the effect of the plastic deformation, the grain refinement was found to occur up to 2.4 mm of depth, which happens due to the relatively low plastic strain required to obtain high levels of β-grain refinement in this titanium alloy, which has also been corroborated in other studies [84].

Overall this techniques promotes (in DED-arc of Ti-6Al-4V) a grain refinement and an increase of tensile properties similar to the ones reported for the inter-pass cold rolling with 50kN [85].

Youheng F. [86], used a system similar to the cold rolling described above, to deform the material when it is hot, a unique difference is that instead of waiting for the part to cool down, the roller travels behind the torch at a constant distance, thus deforming the material at high temperatures. In this particular study the author used a bainitic steel that was deformed at a temperature of 900 °C, with a force of 5000 N and a deformation rate of 0.8 s^{-1}. The results showed that with this hot deformation it is possible to obtain a uniform deformation, and that the as-built columnar dendrite microstructure changes to a fully equiaxed grain structure in the hot-rolled samples. However, the author highlighted that this system is very sensitive to changes of welding bead height, and even small deviations can lead to substantial increases of the roll force, which difficult the production of a flat surface by maintaining a constant distance from the roll to the torch.

Using the same system, Cheng X. [87] studied the effects of Al-Mg4.5Mn alloy, and analyzed the correlation of defects with fatigue resistance. The hot rolling closed about 2/3 of the part defects, and reduce their average size, but the morphology had no variation. Moreover, the hot rolling has not improved the parts mechanical strength, but their elongation was 30 % higher than the conventional DED-arc.

Other studies carried out with similar equipment were also performed in 45 steel [88] and Ti-6Al-4V [89], where, microstructure refinement, texture reduction and improvement of anisotropy and mechanical strength were obtained.

2.5.2 Active inter-layer cooling and heating based variants

Although DED-arc deposition is very similar to welding, there are some new features that have a great influence on the properties of the final component [90].

One of these features is the inter-layer temperature [91,92], i.e. the temperature of the previously deposited layer immediately before the deposition of the next layer, and it determines the conditions of heat dissipation by conduction through the part, affecting the cooling rate and, therefore, the microstructure and mechanical properties of the part. A higher inter-layer temperature combined with high heat inputs results in poor heat dissipation and consequently low cooling rates that result in a coarse microstructure and may lead to an anisotropic material. In an extreme scenario, working with high temperatures lead to unstable depositions and may even lead to the collapse of the wall.

The standard method to control the inter-layer temperature is by imposing an interlayer dwell time, and the part naturally cools down to the desired temperature. However, as the heat dissipation conditions vary along with the build, the inter-layer dell time must also vary to maintain constant the inter-layer temperature, and the deposition conditions. F. Montevecchi et al. [91] developed a finite element-based technique that optimizes the inter-layer dwell time, with the simulation of thermal behaviour during part production, aiming to ensure a constant inter-pass temperature.

Figure 2.7 shows the calculated dwell time variation along with the layers, required to maintain constant inter-layer temperature, for the mild steel deposited with a certain set of parameters, as well as the expected molten pool volume for each layer.

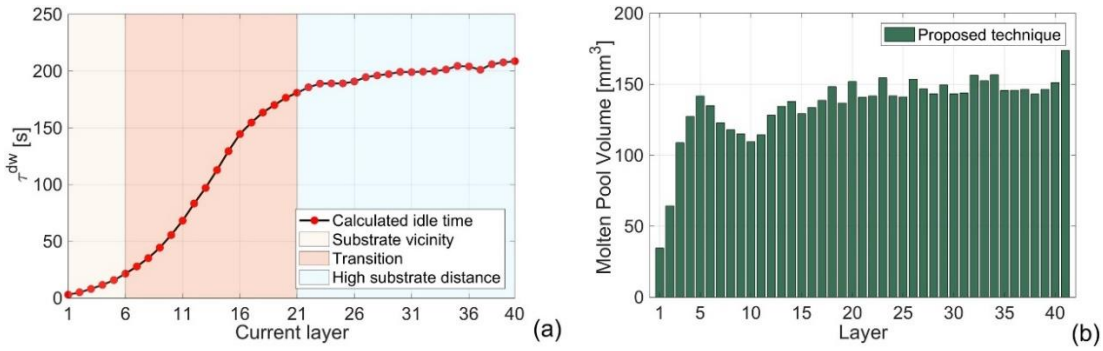

Figure 2.7 - Results of the optimization of the inter-layer dwell time, with finite element simulation: (a) idle time values and (b) expected molten pool volume for each layer.

However, to achieve the same inter-layer temperature in each of the deposited layers, the inter-layer dwell time must be increased until the 21st layer roughly, as can be seen in Figure 2.7 (a). This leads to an increase in the total production time, and therefore, several researchers have been addressing this issue through the use of forced cooling techniques.

Fang Li et al. [93], introduced in DED-arc an in-process active cooling system based on thermoelectric cooling technology, to mitigate the differences in heat dissipation between

consecutive layers. The experimental setup consists of thermoelectric coolers coupled to flat fin heat sinkers that are attached to external fans. The cold side of the thermoelectric coolers was attached to the side surface of the built wall, separated by a highly thermally conductive silicone rubber to ensure good contact between the cooler and the side surface of the wall. This DED-arc variant can reduce the total fabrication time by 60.9%, and simultaneously, due to the increase of the cooling rate, the microstructure was refined by 25%. Moreover, the active cooling compensates for the excessive heat delivered to the part, which enables not only the reduction of the inter-layer dwell time but also the increase of the wire-feed speed, achieving overall higher deposition rates [94]. Although the promising results, this variant lacks regarding its industrialization, as it is extremely complex, time-consuming, and potentially expensive to implement on the production of higher complexity geometry parts.

Another active cooling variant, that does not have the same problem as the above is through the use of a gas jet impingement, which may be applied at the same time of the deposition (immediately after the arc) or in between the layer's deposition. The used gas either can be compressed CO_2 [95–98] or dry air [99–102]. When the gas jet is applied simultaneously with the deposition of the material, it is important to ensure that it does not cause disturbances in the welding shielding gas, especially when the gas used for cooling differs from the gas used as the shielding, since these disturbances promote arc perturbances and inconsistency, and therefore the formation of defects in the deposited material.

Throughout the various studies, results such as microstructure refinement and a slight increase (up to 10 %) in mechanical properties (hardness, yield strength, and ultimate tensile strength) are common. These are mainly due to the more effective heat dissipation that increases the material cooling rate.

The main advantage of this variant is the improvement in manufacturing efficiency through a reduction of up to 80% of the dwell time between the deposited layers [97].

Additionally, the effect of the inter-pass forced cooling on the sample surface waviness, has shown to be material dependent. Some authors reported results of the deposition of the Ti6Al4V alloy, where there are no significant variations in the part waviness [98], while others demonstrate that the inter-pass forced cooling applied during the deposition of mild steel, promotes an increase in the waviness resulting in a decrease of the effective wall thickness of 10% [99].

Another development in the field of forced cooling was made by immersing the part in the production in a water tank. This can be done in a passive way, where only the substrate is submerged during the entire production of the part, or in an active way, where, as the part is being built, the percentage of it that is submerged increases [103]. The results had shown that this parameter of the active cooling has a direct influence on the part surface waviness. The increase of the cooling rate promotes narrower and larger

beads leading to a higher waviness, while an increase of the heat input favours a smother wall surface as it improves the material wettability [104]. Similar to the observed in the gas jet impingement technique, it has also been demonstrated that a refined microstructure and an increase in the microhardness of the deposited material are obtained when the active water cooling is applied [105]. It was also found that this refined microstructure contributes to a part with less anisotropic mechanical properties [103].

In the deposition of aluminium alloys, the presence of water, and its hydrogen content, near the material being deposited may be a concern with regard to pore formation. However, when the samples were compared to the control sample, the authors did not observe any increase in the porosity volume that could be related to the presence of water [103,104].

The disadvantage of techniques that promote faster cooling of the components is that they tend to generate residual stresses of greater magnitude. One possibility for the reduction of residual stresses is to do the opposite, heating the component so that the cooling rates are decreased, and/or causing a heat treatment effect during the production of the part.

An innovative method to mitigate residual stresses was developed by Xingwang Bai et al. [106]. It consists of an inductor with two identical coils mounted on both sides of the part in production, as depicted in Figure 2.8. The inductor can perform different roles according to its relative position to the arc, if it is moving ahead of the arc it performs real-time preheating and, if it is moving behind the arc it performs real-time post-heating.

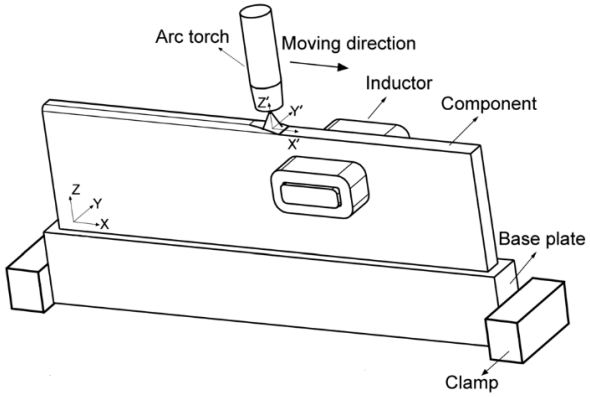

Figure 2.8 - Schematic of induction heating used as a secondary heat source in DED-arc [106]

Through the use of finite elements, the effects of different induction heating patterns on the temperature and stress state during multilayer deposition were investigated and experimentally validated. The results showed that both real-time preheating and post-heating lead to a decrease in the residual stresses, with preheating proving to be more efficient to reduce the residual stress than post-heating.

Although it may seem contradictory, it is possible to reduce the effective heat delivered to the part in production by introducing an additional heat source applied only to the wire.

This variant was developed by Zixiang Li et al. [107] and was named hot-wire arc additive manufacturing (HWAAM), it consists of the use of another power source to heat the wire, which assists the melting of the filler material, and thus it is possible to reduce the energy of arc created by the TIG power source.

The secondary power source has the positive pole connected to the filler wire, while the negative is connected to the substrate, similar to what happened in the MIG/MAG process. However, the electric arc is only established between the tungsten electrode and the part. The current that goes through the wire is conducted by the molten pool that shorts the circuit between the wire and the substrate, heating the wire through the Joule's effect.

The experiments were carried out with the production of four titanium alloy samples, the first was a control sample with no secondary current and an arc heat input of 207 J/mm, in the following samples the secondary current was increased to 60, 80, and 100 A, and the arc heat input as respectively reduced to 180, 142 and 137 J/mm. Besides a visible change in the wall geometry due to different heat inputs, the microstructure of the samples produced with HWAAM was a mixture of short columnar grains and equiaxed ones, instead of the DED-arc typical long columnar β-grains.

This variation of the microstructures has also been reflected in the material mechanical properties, where was observed that with the increase of the secondary current, the differences in both the tensile strength and elongation between the horizontal and vertical direction sharply reduced to a near isotropic state.

2.5.3 Multiple wire-based variants

The ability to add multiple wires to the molten pool simultaneously, increases considerable the versatility of the DED-arc technology, as this enables to control the chemical composition of the deposited material. This control can be done in a stationary way, thus allowing the production of an alloy in-situ, or if it is done transiently, it is possible to selectively vary the properties of the deposited material, i.e. the in-situ production of functionally graded materials (FGM).

Using DED-arc as an in-situ alloying process, enables the low-cost and rapid manufacturing of intermetallic, or other alloys, with different phase compositions, that otherwise are difficult and expensive to produce.

One of these is the titanium aluminide (TiAl) alloys, which are a promising high-temperature structural material, with particular applications in the aerospace field. However, due to their low ductility at room temperature, it is challenging to manufacture these alloys with conventional processes [108]. Several studies have been addressing this issue and studied the production of these alloys with the DED-arc process by controlling the feed speed of each wire (titanium and aluminium wires) independently.

Additionally, the authors were able to control both the resultant microstructure and mechanical properties of the final component [109–113].

When the used materials have very different melting points, the deposition process can lead to the volatilization of the alloy elements with lower melting temperature. As an example, in the production of the TiAl intermetallic alloy, the authors solve this problem by utilizing a two-wire TOP-TIG additive manufacturing technique, with the Al wire fed in TOP-TIG welding mode and the Ti6Al4V wire fed in conventional TIG welding mode [114].

The in-situ production of other intermetallics such as Fe_3Al [115,116] and FeNi [117] has also been successfully carried out using the DED-arc process. The authors were able to finely control the chemical composition of the deposited material, achieving fully dense components with homogenous chemical composition after the 10^{th} layer. Between the first and the 10^{th} layer, the dilution of the substrate into the part was still preponderant.

The in-situ alloying DED-arc technique have been also used to manufacture other alloys. The NiTi alloys are conventionally fabricated using casting or powder metallurgy. However, the casting cannot often make parts with complex geometries, like the ones required for the biomedical and aeronautical industries. Chen Shen et al. [118] have successfully manufactured the binary $Ni_{53}Ti_{47}$ alloy by feeding pure Ti and Ni wires into the molten pool generated by the TIG process. Thus, enabling the production of NiTi complex parts with the DED-arc technology. The same research group has also successfully deposited a copper-rich Cu-Al alloy, using the same experimental setup [119].

Even among the wide range of aluminium alloys, there is always a limitation of the chemical composition of the commercially available wires. The DED-arc technology has consecutively proved that it is able to produce customized aluminium [120,121] and copper [122] alloys by simply adjusting the relative feeding speed of the two, or more, different wires.

As it was mentioned before, when the relative feeding speed of the multiples wires is adjusted during the deposition, a component is obtained with a gradient of chemical composition and mechanical properties, therefore a functionally graded material (FGM) is produced.

When the target is the production of a FGM with a vertical gradient, as illustrated in Figure 2.9, the performed studies showed that it is possible to accurately achieve the designed chemical composition by adjusting the ratio between both wires feed speed for each layer and that due to the remelting of the previously deposited material, the final component has a smooth and continuous composition gradient. Additionally, it was observed that the chemical composition is generally homogeneous in the transverse direction [123–125].

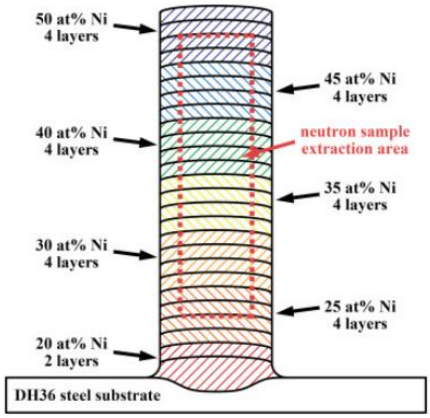

Figure 2.9 - Schematic drawing of a Fe3Ni–FeNi vertical functional graded material

The use of multiple wires in DED-arc can also be applied with the aim to achieve higher deposition rates, by using multiple wires with the same chemical composition. When this technique is combined with a MIG/MAG power supply, the deposition rate can achieve 9.5 kg/h [126]. Although it is mechanically and thermally possible to feed and melt the wire at higher rates, from this point on, the required heat input to properly melt the added material is too high, which leads to the appearance of defects such as porosity, cracks [127] or even to the collapse of previously deposited layers [126]. Therefore, to achieve even higher deposition rates, the use of an additional cooling mechanism, such as the previously mentioned, must be considered. Another study has demonstrated that this increase in the deposition rates is possible without compromising the part accuracy by exploiting the weld bead's asymmetric nature in the transverse twin-wire TIG [128].

Another innovative DED-arc variant, where the authors have completely restructured the basic principles of the DED-arc deposition is the compulsive constriction wire and arc additive manufacturing (CC-WAAM) [129]. This variant consists of establishing an electric arc between the metallic wire feedstock and a tungsten electrode, rather than between the wire (or the non-consumable electrode) and the workpiece in traditional DED-arc. Additionally, the melted metal in this stage is forced to be ejected from a nozzle with a narrow space. Figure 2.10 shows the schematics of the CC-WAAM variant.

This variant has several similarities with the PAW and Keyhole-TIG processes, but the core difference is that in these processes only the shielding gas and/or the electric arc are constrained and forced to pass through a narrow space, while in this variant the authors also force the molten material to pass through the same orifice that constricts the shielding gas and the electric arc.

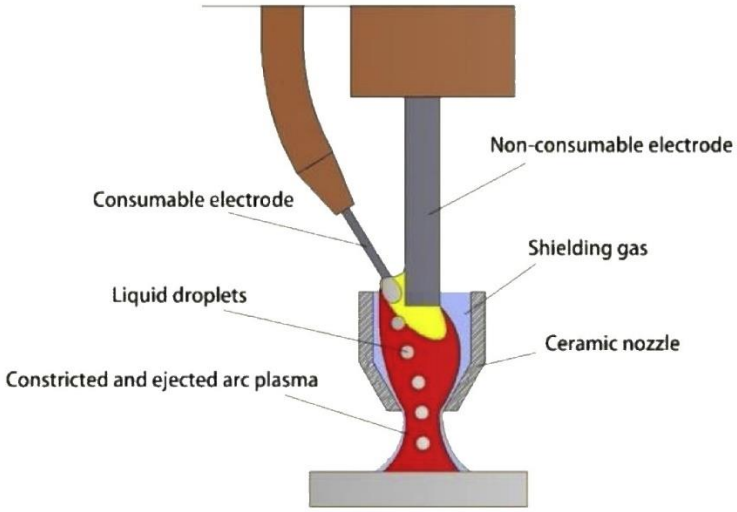

Figure 2.10 - Schematic of the compulsive constriction DED-arc variant

The main advantage of this process is that the heat input that is actually delivered to the workpiece is considerably less than the one in a conventional DED-arc process, as demonstrated by Rodrigues et al. [130] in a similar study with the only difference being the non-constriction of the molten material.

Additionally, this lower heat input, has an impact on the microstructure of the material, promoting a fine and homogeneous microstructure distribution, with less sharp or even inexistent interlayer boundary [129].

2.6 Summary

The principles of the DED-arc AM technology were described, as well as its benefits and shortcomings.

To overcome these, new variants have been developed by different research groups, but most of them simultaneously hinder some characteristic features of the DED-arc process namely, the high deposition rate and the ability to produce parts with medium/high geometric complexity. In detail these new variants obstruct the industrialization of the process impractical because they:

- Require systems with high structural rigidity;

- Require additional degrees of freedom from the movement equipment;

- Introduce additional complexity to the path planning;

- Increase the dwell time between layers;

- Increase the complexity and set-up times.

Therefore, this work aims to contribute to improve the technology by developing an innovative concept of a multi-feed device wherein the different inputs are decoupled and

can be controlled independently. To overcome defects such as porosity and coarse microstructure, a new system was proposed consisting of hot forging the material while it is in the viscoplastic regime. Therefore, it is possible to exploit the low forces required to forge the material without the need for deposition systems with high structural rigidity, nor detriment of any other advantage of the DED-arc process. Additionally, it was also proposed a new variant based on thermodynamic work, to control the material cooling rates, and thus, prevent grain coarsening.

3

Chapter 3
Development of customized research equipment

3.1 Introduction

This chapter describes the equipment developed within the scope of this thesis. The development of a customized 3-axis movement system is described in section §3.2.

To achieve the proposed objectives of introducing two new variants to the DED-arc process, a fully customized deposition torch was developed and produced. In section §3.3 the development of 3 prototypes of the customized torch to forge the deposited material in the viscoplastic regime or at high temperature and to control its cooling is detailed. It is also presented the results of the preliminary tests that allowed the validation of the innovative concepts introduced in the torch.

3.2 Development of 3 axis moving table

One of the tasks of this work was the design, development, production and validation of a customized moving equipment with 3 degrees of freedom to be used as a 3D printer. The in-house production of a customized equipment allows for greater flexibility, especially for research, that otherwise would be impossible to obtain. The equipment can be modular, which facilitates eventual changes after its production and allows further developments of DED-arc technology as well as to carry out researches in other fields without the need to develop or purchase new equipment. Furthermore, the commercial DED-arc machines are pre-defined by the manufacturer and some of the software control parameters are locked, so the user can not change them, which in a research environment can be a huge constrain. Additionally, the possibility to add instrumentation devices is an asset.

During the development stage of the equipment, several aspects were taken into consideration to cover not only the current need, but also future needs, as well as its use for other applications than DED-arc. Thus, the following requirements were established:

- Human size scale equipment;
- Mechanical stiffness;
- Modular structure with easy customization/adaptation;
- ± 0.5 mm of positional accuracy;
- Facility to couple additional instrumentation;
- Independence of the torch from the moving system;
- Moving speed ≥ 3 m/min in both X and Y axis;
- The moving head with connections for:
    - Stepper motors;
    - USB;
    - Welding power source;
    - Shielding gas.

Considering the functional requirements above, the equipment was 3D modelled in CAD software as shown in Figure 3.1. It was adopted a cartesian configuration based on a multi-base upright mount for Z-axis, and a base mount for Y and X axis.

The X-axis consists of 2 linear guides supported by a rectangular frame. The Y-axis is composed of a structure with 2 *Bosch* profiles of 40 by 120 mm that support two linear guides, which have attached the movable head in which the different DED-arc torches can be attached.

For building the machine frame, the 80 x 80 mm *Bosch Rexroth's* profile was selected. These aluminium profiles provide the required stiffness for this application. The wide range of connections and accessories available for these profiles provide them with great

versatility, enabling the coupling of other features, such as instrumentation, and eventual changes to be made effortless.

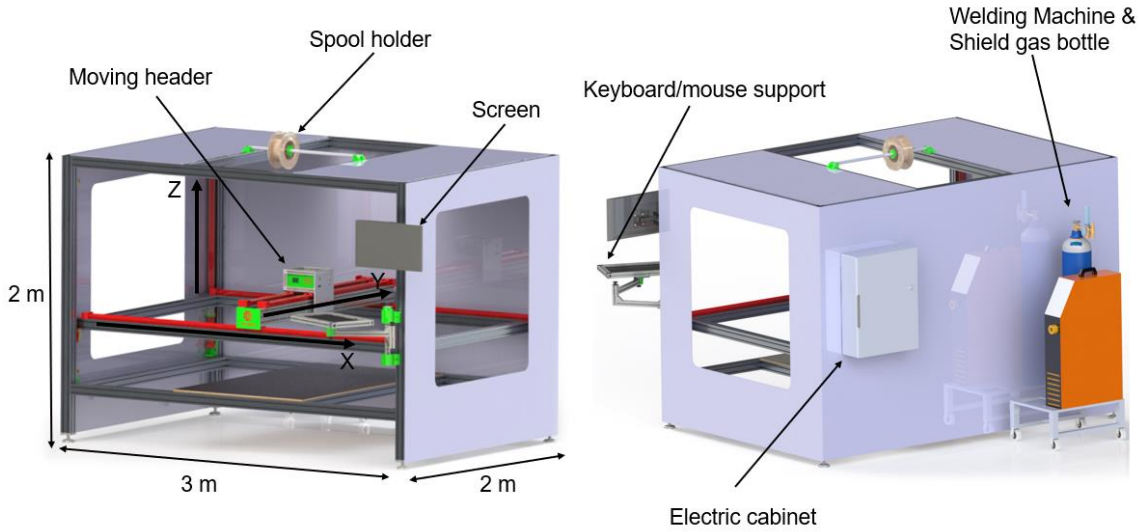

Figure 3.1 - Computer aided design (CAD) model of the 3-axis movement system to be used as a customized 3D printer

The movement of the table was achieved by linear guides with carriages. For both X and Y axes, two *Igus drylin ® ZLW-1040 Standart-02* model linear guides were used, with movement transmission through a toothed belt and a useful stroke of 2500 mm on the X-axis and 1400 mm on the Y-axis. All these guides have, at one end, a shaft and a support for coupling a NEMA 23 stepper motor. The transmission ratio of the linear guides is 70 mm/rev, i.e., for each rotation of the shaft the carriage travels a linear distance of 70 mm. Although it may depend on the guide length, the specification of these guides indicates that a maximum deviation of ± 0.2 mm, from the prescribed position, with a maximum radial load of 300 N is guaranteed.

The Z-axis has to support the weight of the moving parts of the equipment, as well as, any additional loads (e.g. instrumentation or equipment) that may be added. Taking this into account, four *Igus drylin® SLW-1040* linear guides were selected for the Z-axis with a useful stroke of 1250 mm. The movement transmission is made through a trapezoidal lead screw (with 10 mm of diameter) and a carriage with a ball-bearing nut. Since the trapezoidal lead screw has a single start thread, the transmission ratio is given by the screw pitch, which is 2 mm, i.e. for each rotation of the shaft the carriage travels a linear distance of 2 mm. The use of linear guides with lead screw allows to lift high loads even with low power stepper motors, however, this is only possible at the expense of the speed of the movement. Each linear guide can stand a maximum axial load of 700 N.

To actuate each linear guide, the *57STH56 NEMA-23* bipolar stepper motors equipped with a planetary gearbox with a reduction ratio of 4.25:1 were selected. The step angle

of the stepper motor is 1.8 º, which corresponds to an angle of 0.42 º at the gearbox output. Considering the transmission ratio of 70 mm/rev in the X and Y axis guides and 2 mm/rev in the Z-axis guides, resulting in a resolution of 0.093 mm on the X and Y axes and 0.0023 mm on the Z-axis. Additionally, this resolution can be increased by using a stepper motor driver that is able to subdivide each step, as explained later in this chapter.

This stepper motor combined with the planetary gearbox has a maximum torque output of 4.57 N·m. Disregarding the friction between the ball bearing and the lead screw, and considering a mean lead of the screw of 10 mm it is possible to estimate, with equation 3.1, the total load that each motor/guide assembly can lift in the Z-axis. Thus, the maximum value of 2.87 kN was calculated, which exceeds the 700 N recommended by the manufacturer of the guides, and thus the stepper motor is suitable for the application and is oversized to not be the limiting element of the load capacity. Additionally, loads up to 2.17 kN can be placed on the rectangular structure, which also supports the X and Y guides, without compromising the movement of the system in the Z-axis.

$$F_z = \frac{T_m \cdot 2 \cdot \pi}{P} \qquad \text{Eq. 3.1}$$

Where: F_z [N] is the maximum vertical load, T_m [N·m] is the stepper motor torque, and P [m] is the screw lead.

Regarding the X and Y axis guides, the maximum vertical load that the stepper motor can move depends, among other things, on the friction coefficient between the carriage and the guide. In this case, these guides have a polymeric bush that has a static friction coefficient (against anodized aluminium) of approximately 0.18. The other important parameter is the diameter of the pulley that moves the belt, which, although not provided by the manufacturer, can be calculated through the transmission coefficient. Thus, considering that the transmission coefficient of the linear guides is 70 mm/rev this is equivalent to saying that the pulley has a mean perimeter of 70 mm, which corresponds to a mean radius of 11.14 mm. Using equation 3.2, where: F_x [N] is the maximum radial load, T_m [N·m] is the stepper motor torque, μ is the coefficient of friction, and r [m] is the pulley radius, the value of 2.28 kN was calculated for the maximum radial load that each guide/motor assembly can move along the X and Y axes, exceeding the 300 N recommended by the guide manufacturer and therefore, leaving the engine oversized so as not to be the limiting element.

$$F_x = \frac{T_m}{\mu \cdot r} \qquad \text{Eq. 3.2}$$

For the axial load the maximum value was calculated (considering that no other loads are applied, and the effect of friction is negligible) dividing the motor torque by the guide pulley radius, which results in a maximum axial load of 410 N.

The electronic system of the machine is composed of an *Arduino Mega 2560* connected to the *Ramps 1.4* shield, which is widely used in the common fused deposition modelling 3D printers. This control module was chosen because it does not have built-in stepper drivers, which allows the use of any type of stepper driver. In this application, it is essential that the drivers are not embedded in the control board, as the equipment has 8 stepper motors, each one consumes an electric current of about 2 A each, and if they are all active at the same time, a current of 16 A would have to pass through the control board circuit, and these boards are not suitable for handling that much current. Thus, the *PiBot Driver Rev2.2* stepper drivers were selected. Each stepper driver is powered externally from the control board (as shown in Figure 3.2) and can handle a maximum current of 4 A. These stepper drivers are also able to sub-divide the steps into further increments up to 16 times.

To control the axis with multiple stepper motors properly, the signal generated by the ramps was multiplied to the drivers of each motor, to assure a synchronous movement among the motors of the same axis.

The Arduino was flashed with the open-source firmware *Marlin*, which uses a derivative of G-code control language to execute simple tasks. Since this firmware is design for the widely used fused deposition modelling printers, adjustments in the steps per millimetre ratio of all the axis were made, and all temperature sensors and alarms have been disabled.

The control board is also responsible for the communication with the MIG/MAG welding power source, by simulating the push of the torch trigger with a relay. Figure 3.2 shows the electrical diagram of the 3-axis movement system.

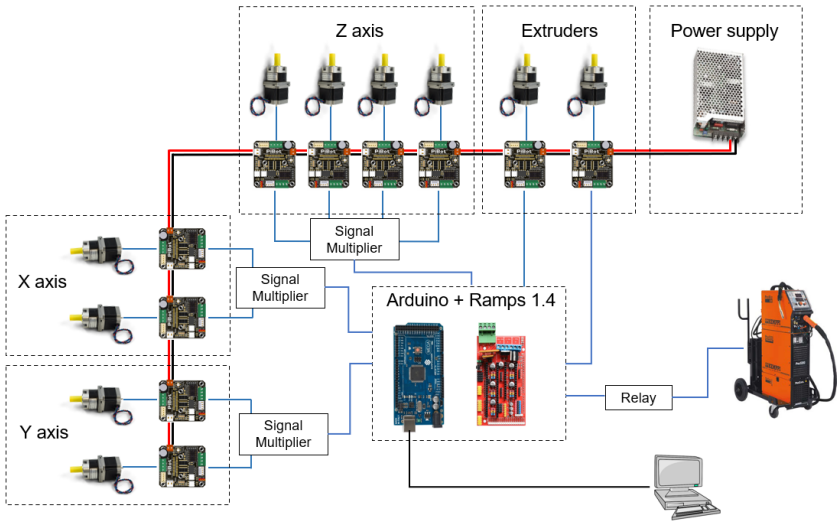

Figure 3.2 - Electrical diagram of the developed 3-axis movement system

To provide the necessary power for the melting of the material, a KEMPY welding machine was used, with a Pro MIG 3200 power source and a Pro MIG 501 control unit.

A copper power cable (with a section of 25 mm^2) was connected to the negative output of the power source, which passes through energy chains until it reaches the movable head, thus making available the electric power for the coupled torches. A power cable was also connected to the welding machine power supply positive pole and the equipment steel substrate. Thus, if it is necessary to change the polarity, it can be simply done by changing the connections of the cables on the welding machine power supply.

To provide the shielding gas to the torch, a flexible tube was passed through the same energy chains, from the movable head to the solenoid valve inside the welding machine, thereby, the welding trigger automatically activates the shielding gas. Figure 3.3 shows a photograph of the final version of the moving equipment. The equipment has been used almost daily since 2018 and has demonstrated excellent reliability and overall performance.

Figure 3.3 - Photograph of the developed 3 axis 3D printer

3.3 Development and test of customized DED-arc torch prototypes

In most of the research carried out in the DED-arc field, the used setup consists of conventional welding torches attached to a 6-axis robot arm. However, conventional welding torches were initially designed for manual welding and to be used by an operator where ergonomic and safety concerns exist. Thus, power, shielding gas, and wire must be fed through the same hose. Due to these design constraints, the commercial welding torches were not optimized for the application in DED-arc processes and do not provide the necessary flexibility to implement the proposed variants. Therefore, an innovative concept of a multi-feed device wherein the different inputs are decoupled was designed and manufactured to better fulfil the DED-arc needs. It is also worth noting, that all the device inputs can be controlled independently, except for the WFS that needs to be coupled to the electric welding power.

This concept was developed in 3 stages. The first aimed to develop a prototype able a proof of concept. The second incorporated technical improvements identified in the first prototype aiming to produce parts with more than one layer. Finally, a fully functional prototype was produced.

3.3.1 Prototype 1 – Proof of concept

The main objective of the development of this prototype was to carry out a preliminary proof of concept regarding the plastic deformation of the deposited material while it is in the viscoplastic regime or at high temperature. This torch consisted of a wire feeding system, in which the wire was guided to a set of rollers, one of which is a bearing with freedom of rotation and the other a steel roller connected to a stepper motor, whereas according to its rotation speed, the wire feed speed was determined.

To introduce the shielding gas, an adapter was designed, that was connected to a standard welding gas diffuser, placed inside the gas nozzle.

The temperature at which most steels are in the viscoplastic regime is between 950 and 1300 ºC. To identify the region in which the material is in the viscoplastic regime during its deposition, a temperature measurement was performed with a thermographic camera. Although the emissivity coefficient varies in the electric arc zone, and therefore the temperature measured near the electric arc is inaccurate, it is possible to obtain an approximation of the temperature of the surrounding material. From the temperature field measurement shown in Figure 3.4 a), the temperature data of a horizontal line passing through the molten pool were obtained and is shown in Figure 3.4 b). An approximation of the zones in which the material is in the liquid and viscoplastic state are also represented, as well as the temperature above which the material is in the viscoplastic regime (950 ºC).

During the material deposition through the DED-arc process, the material is in this temperature range at a maximum distance of about 12 mm from the arc.

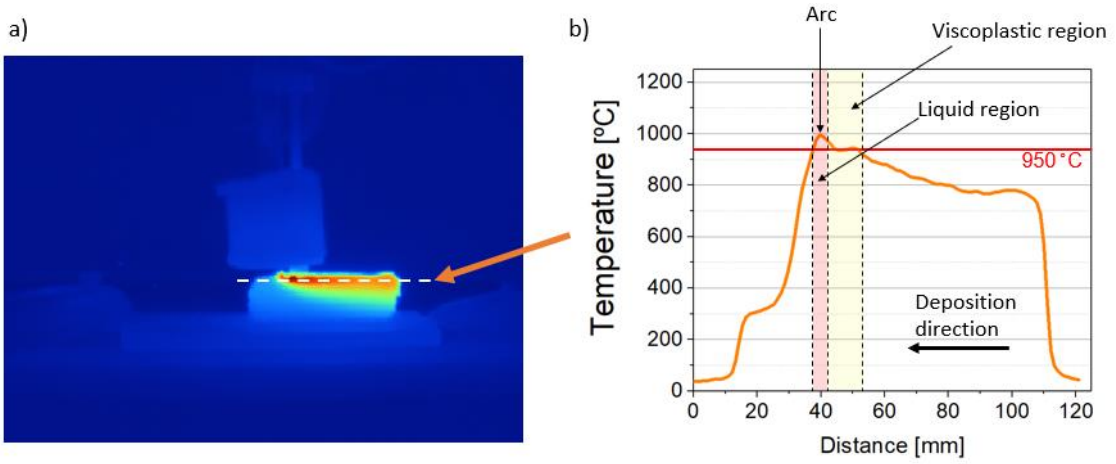

Figure 3.4 –Thermographic image acquired during material deposition (a), and horizontal temperature distribution of the deposited material (b)

Therefore, to take advantage of this viscoplastic regime, the hammer has to be placed at a maximum distance of 12 mm away from the arc, thus, the prototype was designed with the hammer placed inside the gas nozzle.

To provide the mechanical work, a solenoid actuator, *Mechatronics* model TT2, with simple action was used. The maximum force of the solenoid was 35 N when its stroke is in the zero position (fully closed). The actuator was controlled using a solid-state relay, which interrupted the power supplied to the solenoid through a signal sent by a signal generator. The frequency of the hammer's movement (up and down) was, thus, determined by the frequency of the control signal. Since the actuator is single-acting (i.e. it only exerts force in one direction) it was necessary to insert two springs so that when the actuator is deactivated it returns to the initial position, where the hammer is not in contact with the workpiece. It is important to notice that the force applied by the springs is in the opposite direction to the force of the solenoid so the resultant force is lower than the force exerted only by the solenoid.

The support of the forging system was manufactured in Polylactic acid (PLA) through the Fused Deposition Modeling (FDM) 3D printing process. This support consists of two main parts: the fixed part, shown in blue, which is attached to the steel rod that guides the consumable wire and supports the solenoid chassis; and the movable part, shown in green in Figure 3.5, which is fixed to the movable part of the solenoid (core) and connects to the hammer through an M3 threaded rod.

Even though the entire forging system is electrically isolated from the rest of the deposition system, when the hammer touches the workpiece it has the same electrical potential of the part (the positive) and since the hammer is very close to the welding

nozzle, the arc may be established between the welding nozzle and the hammer, instead of being established between the wire and the workpiece. Thus, the hammer tip was produced in *MACOR*, which is a ceramic material, and therefore a good electrical insulator, eliminating the possibility of establishing undesirable arcs. This material also has the characteristic of being machinable through conventional processes, which greatly facilitates production and allows to make simple and particle changes in its design. In this first approach, a cylindrical hammer with a diameter of 10 mm was produced.

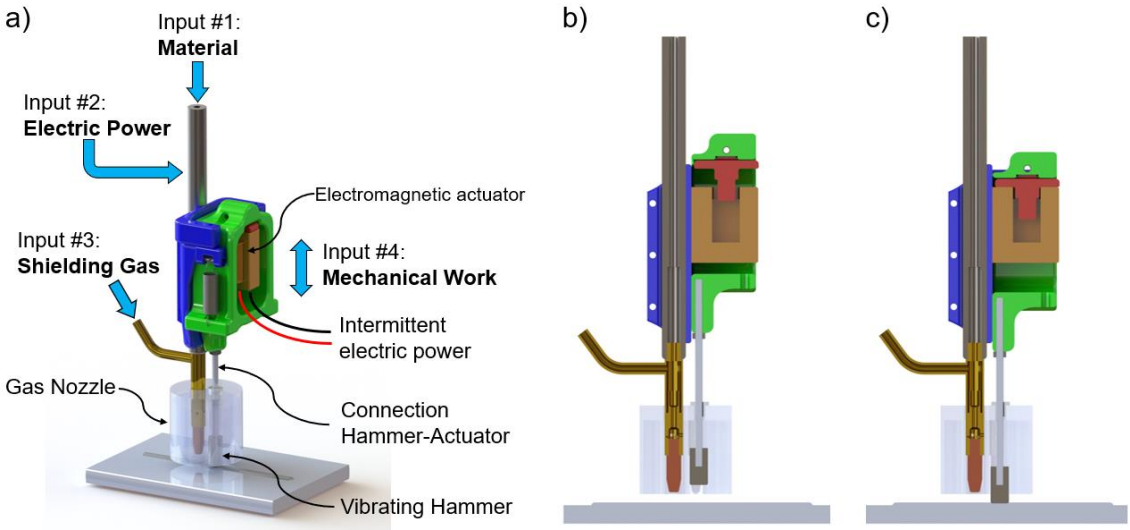

Figure 3.5 - CAD model of the proof-of-concept torch prototype (a) with a section view showing the hammer in the retracted (b) and extended position (c)

3.3.1.1 Experiments and proof-of-concept results

To demonstrate the feasibility of the concept of plastic deformation during the deposition of material, samples of 316L stainless steel were produced. The length of the samples was fixed at 100 mm. The process parameters used to deposit and deform the material are shown in Table 3.1. It should be noticed that the hammer force is prescribed by a solenoid actuator and therefore, it can vary depending on the position of the solenoid when the hammer hits the workpiece.

Table 3.1 - Process parameters used in the proof-of-concept experiments

Welding mode	MIG welding – continuous mode (DC+)
Wire feed speed	3 m/min
Current RMS	43.4 A
Travel speed	0.36 m/min
Voltage	20 V
Contact tip to work distance	8 mm
Shielding gas	Argon 99.99 %
Gas flow rate	20 L/min
Forging frequency	10 Hz
Distance from the arc to the hammer	9 mm

To evaluate the effect of the hot forging, a single bead sample was performed and the hammer was activated in half of the deposit length, as shown in Figure 3.6. With this first test it was evident that the hammer has a considerable impact on the bead geometry as it flattens the layer. The plastic deformation occurs constantly and uniformly during the deposition creating a flat top surface.

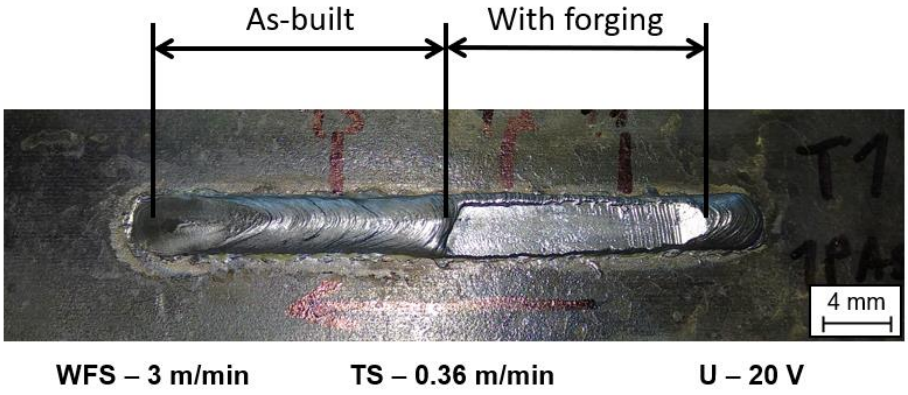

Figure 3.6 – Top view of a single bead produced with and without forging

The sample was cut and prepared for metallographic analysis. Cross-sections from both the deposit as-built and with forging were analysed. Metallographic analysis close to the top of the forged layer show a length of about 0.75 mm where the grain is more refined than that observed in the same zone of the as-built layer (Figure 3.7). This confirms that the deformation caused by the hammer induces grain refinement.

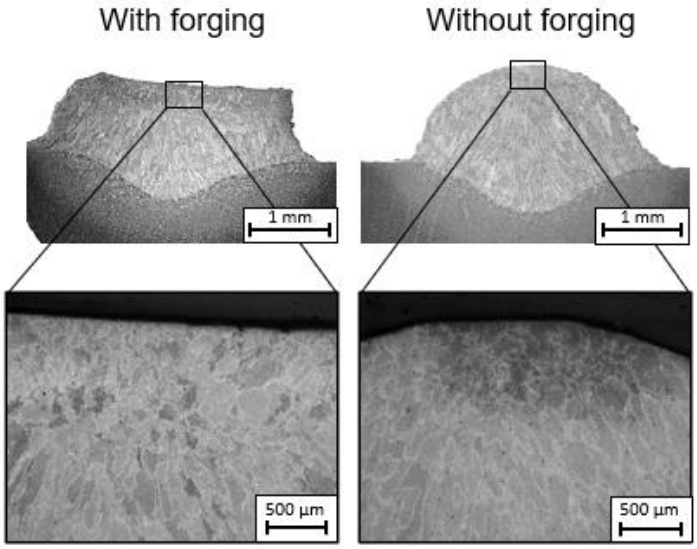

Figure 3.7 - Macrographs and micrographs of single beads shown in Figure 3.6

However, the deposition of the following layer is expected to melt this zone of grain refinement and promote grain coalescence. To assess this effect, samples with two layers were manufactured.

Since the gas nozzle was significantly wider than those normally used in welding, the shielding gas flow has been increased to compensate the nozzle diameter and provide a good gas protection of the molten pool. However, for samples with two layers, as the height between the nozzle and the substrate increased, the presence of porosity was observed in the upper layers, suggesting that gas protection was insufficient. Although it was not possible, with this setup, to make a reliable comparison in microstructural terms, it was systematically observed that the areas that had been forged had less porosity than the non-forged ones, as shown in Figure 3.8.

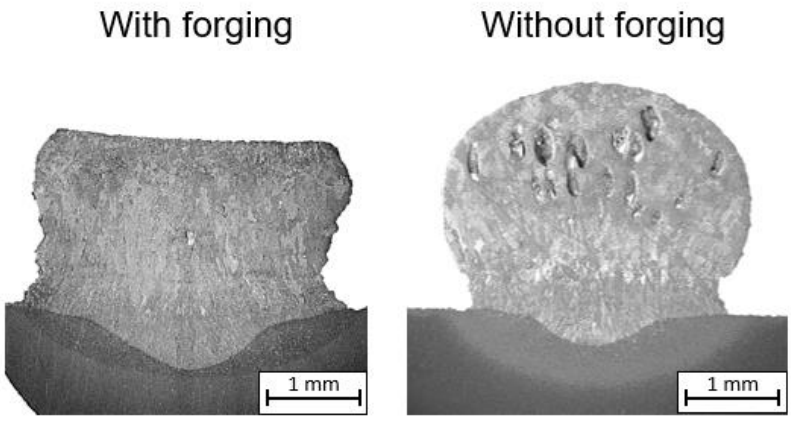

Figure 3.8 - Macrograph cross-section of a two layers samples performed

Overall, the proof-of-concept results showed the potential of this new variant, demonstrating that it is possible, with low forces, to apply plastic deformation

immediately after the material deposition, while it is at high temperatures, and that this deformation promotes changes in the microstructure of the material and reduces the porosity. However, there were identified several aspects that needed correction and improvement:

- The fact that the solenoid does not apply a constant force throughout its stroke length, required a very fine-tuning of the distance between the torch and the workpiece, and when the workpiece presented an uneven upper surface, even if small (about 1 mm), the plastic deformation was no longer uniform, which made it impossible to produce samples with multiple layers.
- After a few tests, the hammer started showing signs of deterioration, such as cracks and splinters, and in some cases, it even failed completely. Therefore, it was necessary to change the hammer material to increase its reliability and durability.
- The gas nozzle compromises the performance of the shielding gas on the molten pool, as the flow is coming out in a turbulent regime and without a preferential orientation because the nozzle diameter does not constrict it in only one direction, causing the appearance of porosities in the upper layers of the samples.

3.3.2 Prototype 2 – Technically improved

A second improved prototype was designed and produced introducing changes in the actuator, the hammer material and the gas nozzle.

To obtain a constant force throughout the hammer stroke, the actuator was changed from a solenoid to a double-acting pneumatic actuator, in which the obtained force is proportional to the pressure of the compressed air that was controlled with a *Festo MS-LFR* pressure regulator. To actuate the pneumatic cylinder a 5/2-way bi-stable solenoid valve *Festo VUVS-LK20* controlled by a data acquisition (DAQ) device was implemented.

To improve the hammer tip reliability and durability the material was changed to tool steel. However, this is an electric conductive material, requiring some additional precautions. The welding nozzle was electrically isolated from both the main conductor (+) and the substrate (−) as in MIG torches. The vibrating hammer was electrically connected to the main conductor (+) through a high electrical resistance (R) (Figure 3.9). Thus, when the hammer is lifted but remains very close to the DED-arc part, its electrical potential is the same of the main conductor (+), thereby avoiding arc ignition between the two. In addition, the high electric resistance (R) also avoids the current to flow from the part to the hammer when a short circuit is established due to the hammer contacting the part, and prevents the arc from being established between the hammer and the part when they are not in contact, as the resistance value is higher than the arc resistance.

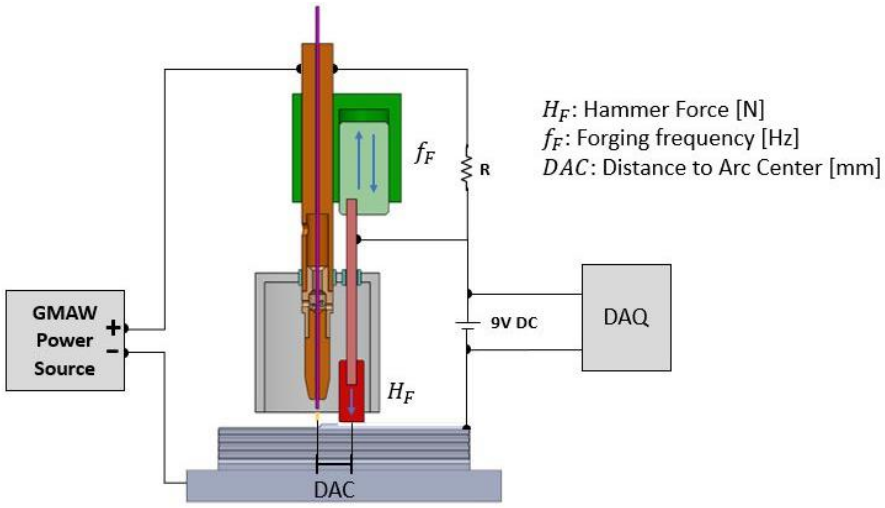

Figure 3.9 - Electrical scheme developed to avoid unwanted arc ignitions

To solve the porosity problem, the open bottom of the nozzle was partially covered, leaving open only a central strip of about 15 mm wide. In Figure 3.10 is presented the multi-feed device prototype.

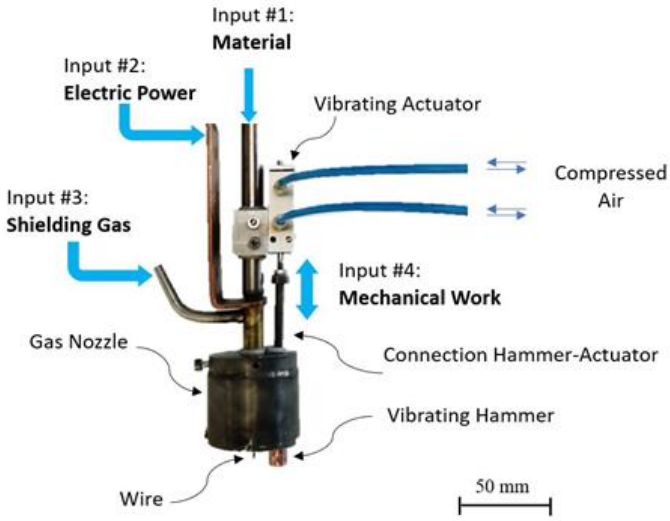

Figure 3.10 - Multi-feed device prototype

The evaluation of the intermittent contact between the hammer and the workpiece was carried out through the implementation of an electrical circuit (represented in Figure 3.9). This circuit includes a 9 V battery with one pole connected to the hammer and the other to the workpiece, thus, the hammer works as a switch, and when it comes in contact with the part it closes the circuit. In this way, the voltage measured at the battery terminals depends on whether the hammer is in contact with the part or not. Thereby, the contact period (short circuit) corresponds to a low voltage and the noncontact period (open circuit) to a high voltage. A data acquisition device was used to measure and record the voltage at the terminals of the battery at a sample rate of 5000 samples per second. For this test, a hammer frequency of 10 Hz and a duty cycle of 50 % was established. The

results of the hammer frequency accuracy shown in Figure 3.11, confirm that the pneumatic system responds according to the prescribed parameters within an acceptable window.

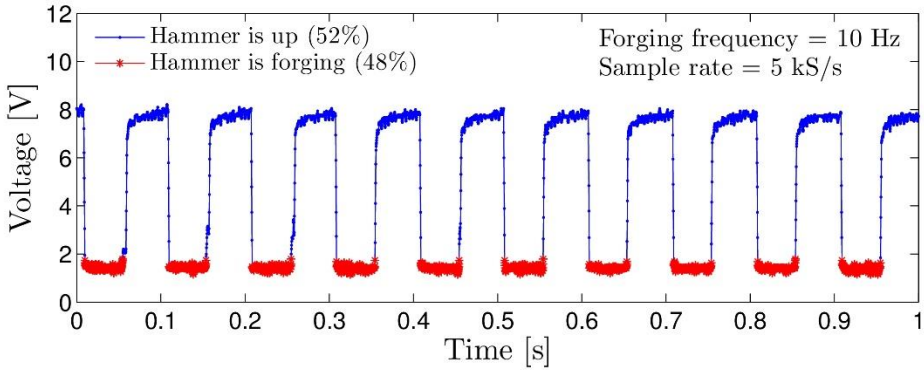

Figure 3.11 - Variation of voltage with respect to time to evaluate the hammering frequency accuracy

The thermal field analysis during material deposition was used to determine the temperature of the material while it is being forged, and the temperature of the hammer during this process. Figure 3.12 depicts a thermographic image acquired during the deposition of a multilayer sample produced with a cylinder-shaped hammer under a load of 17 N. As it can be seen, the material under the hammer is at a temperature of about 917 °C, while the hammer is at 250 °C. At these temperatures, materials such as the austenitic stainless steel 316L shows strain hardening, thermal softening, and coupled effect of temperature and strain, since it is in the range of hot working conditions (800 to 1200 °C) [131]. Looking at the hammer temperature, since it is made of tool steel the temperatures reached are insufficient to damage or soften it. Thus, this thermal analysis allows to confirm that the hammer actuates on the material while it is still at temperatures in the range of hot working operation, which can improve the mechanical properties of the deposited material.

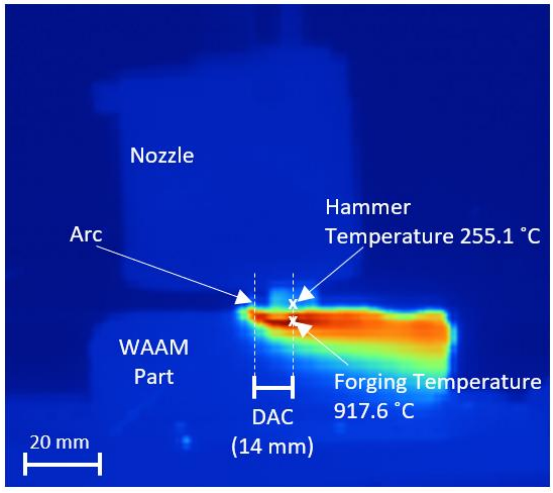

Figure 3.12 - Thermographic image of the deposited layer during the forging process

3.3.3 Prototype 3 – Functional prototype

The development of the functional prototype considered all the undesirable aspects observed during the production and testing of the previously ones.

Since the DED-arc process is mainly advantageous to produce components with medium/high geometric complexity, the design used in the previous prototypes does not favour this characteristic of the process. Since the hammer is linearly aligned with the welding tip, nonlinear depositions are not possible or cannot be performed without an additional degree of freedom (rotation) of the robot or XYZ table and the consequent increase in the complexity of the AM trajectory code.

To overcome this obstacle, the hammer was designed as a circular crown placed concentrically with the welding nozzle, it can be outside or inside the gas nozzle, or it can be the nozzle itself to have alternating vertical movement and also function as a hammer (Figure 3.13). Thus, the circular hammer enables the ability to forge nonlinear deposition paths since the forged area can run along 360˚, which makes the forging action independent of the torch moving direction. As the hammer surrounds the welding tip, part of the hammer is always aligned with the deposited material whatever direction the welding tip moves.

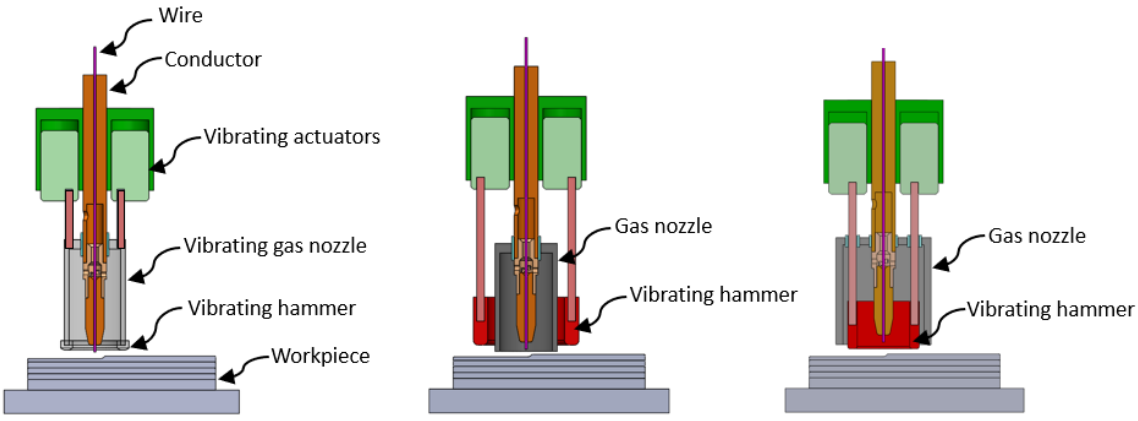

Figure 3.13 - CAD model of the hammer place option: (a) gas nozzle as a hammer; (b) hammer outside of the gas nozzle; (c) hammer inside the gas nozzle

It was chosen the version in which the gas nozzle also functions as the hammer, where a circular crown was placed at the bottom end of the nozzle, which is the component that works as the hammer. This variant allowed more freedom in the selection of the distance between the hammer and the arc, since both inside and outside hammer variations the gas nozzle impose limitations to the hammer positioning.

One of the aspects of concern was the stability of the hammer support. When the hammer touched the workpiece, even for a few seconds, it suffered a horizontal force, due to the drag, that caused flexion of the hammer support. To correct this, a *SKF* linear guide was added to guide the nozzle/hammer system.

In order to guarantee that the circular crown hammer actuated symmetrically and prevent rotation instead of a translation movement, two pneumatic actuators were placed symmetrically, and the pneumatic circuit was split as close as possible to the actuators. The objective was that the pressure drop in the pneumatic circuit was equal in both actuators.

The pneumatic system consisted of: two *Festo ADN-12-10-I-P-A* pneumatic cylinders; one *Festo MS-LFR* air filter; one pressure regulator and gauge; and one 5/2-way bi-stable solenoid valve *Festo VUVS-LK20* (Figure 3.14).

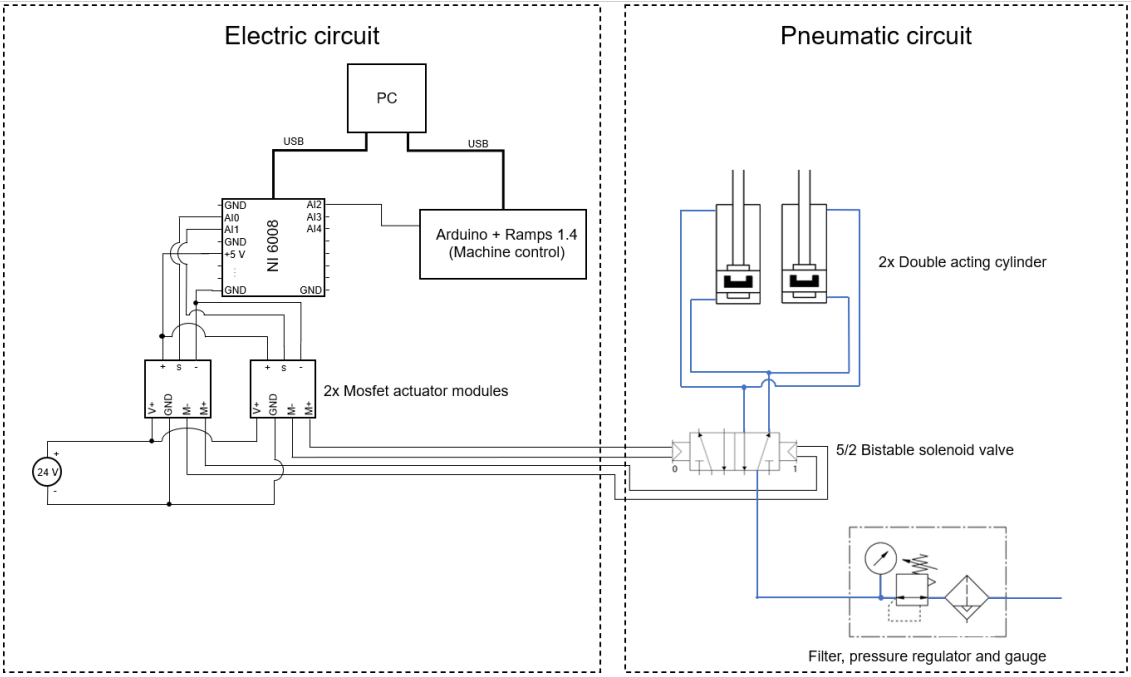

Figure 3.14 - Electrical and pneumatic scheme of the torch

Regarding the control of the pneumatic cylinders, this was done using an *NI 6008*. This board controls 2 MOSFET actuators from *Tinkerkit*, which in turn controls the power that activates each of the solenoids of the valve. The *NI 6008* is connected to a PC, through which it is possible to start the system. Additionally, after setting the parameters (frequency and duty cycle) on the PC, the activation of the pneumatic system can also be done through an analogue port of the Arduino, that controls the movement table, by introducing the G code line "M42 P5 S255" to start the system and "M42 P5 S0" to stop the system.

The introduction of duty cycle control is of great importance. Since deformation occurs in the first moments of the contact, with this functionality it is possible to decrease the unnecessary contact time between the hammer and the workpiece, which consequently decreases the time that it is being dragged, and prevents it from stick to the workpiece.

Intending to cool the entire nozzle and consequently the shielding gas, this torch also comprises a cooling system, in the form of a cooling coil that surrounds the welding

nozzle. This coil is then connected to a system that contains a pump to circulate coolant liquid through the coil, and a heat pump that performs the cooling of the liquid. To ensure continuity between the nozzle and the copper tube coil, the components were brazed with a filler material containing 60 wt.% of Ag and 40 wt.% of Cu, which is a material with high thermal conductivity, thus facilitating the heat transfer between the liquid and the torch. In Figure 3.15 is presented the designed CAD of the torch.

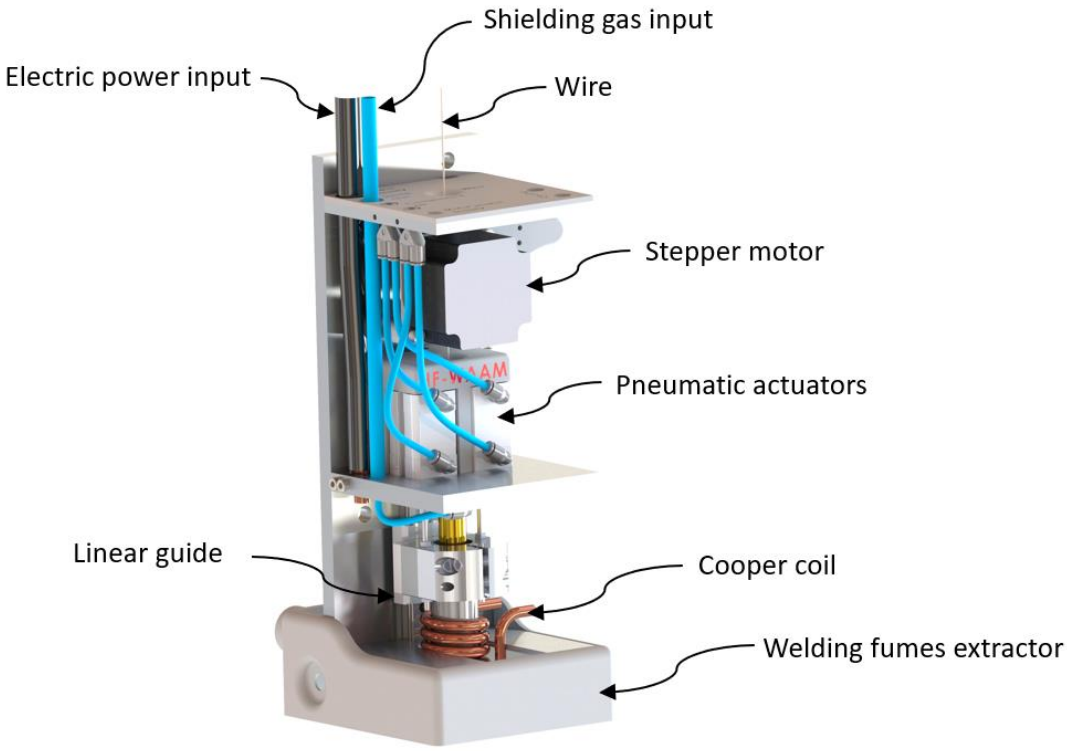

Figure 3.15 – Final CAD model of the torch. A video of the system can be seen here: video

3.4 Summary

A customized and flexible moving equipment, with 3 degrees of freedom and a working envelop of 2.50 x 1.40 x 1.25 m, was designed, produced and validated.

A customized DED-arc torch with the concept of a multi-feed device was designed and produced. Different inputs were decoupled to be controlled independently. A fully functional prototype was designed and manufactured, and this included the two new variants of the DED-Arc process: Hot Forging and Indirect-Cooling.

This part of the work was of major importance since it allowed to have a piece of equipment sufficiently versatile and controllable for research, which was not available in the market. This customized equipment supported almost all subsequent experimental developments, assuming a strategic rule for this thesis.

4

Chapter 4
Characterization of the forging mechanism

4.1 Introduction

This chapter describes the characterization of the forging mechanism. The new process parameters introduced by the hot forging variant are presented in section §4.2. Section §4.3 describes the kinematic and dynamic characterization of the forging device in which the maximum hammer speed, impact force and deformation rate, during forging, were calculated. Finally, section §4.4 presents the validation of the hot forging mechanism and its ability to produce multi-bead layers.

4.2 Forging process parameters

The introduction of forging during the deposition also introduces an additional set of process parameters that may influence the material metallurgic, mechanic, and geometric properties. This set of parameters are: the forging force, F_F [N]; forging frequency, F_f [Hz]; distance to arc centre, DAC [mm]; hammer geometry. The DAC, can be controlled by changing the hammer diameters. During this work, 3 hammers with different diameters were designed and produced as shown in Figure 4.1.

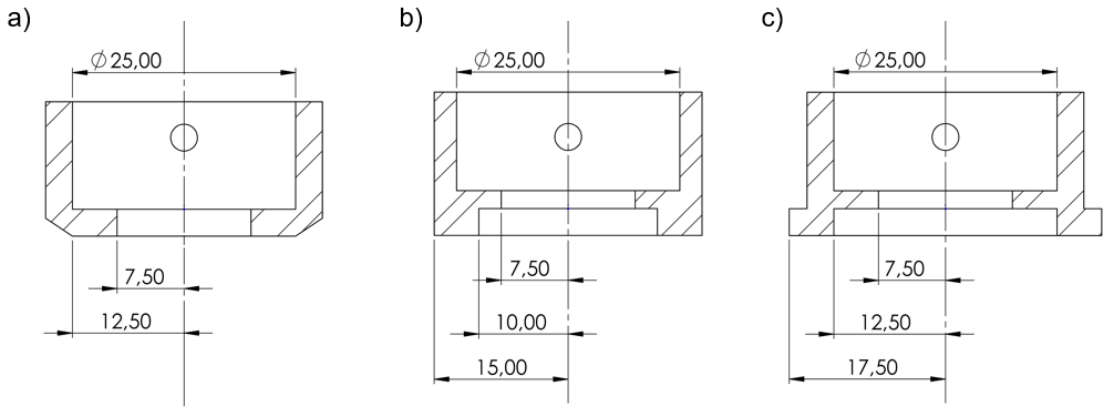

Figure 4.1 –Cross-section drawing of the hammers with a DAC of (a) 7.5 mm, (b) 10 mm (c) and 12.5 mm

The area forged in each hammer stroke depends on the bottom surface geometry of the hammer and the forging step, F_s [mm], (i.e., the distance in millimetres travelled by the hammer in one cycle); which is a function of the forging frequency, F_f [Hz], and travel speed, *TS* [mm/s]. Thus, the forging step is given by the following equation:

$$F_s = \frac{1}{F_f} \times TS \qquad \text{Eq. 4.1}$$

For a circular crown hammer shape, the forging step must be lower than the crown thickness to avoid leaving unforged areas between steps. To determine the applied pressure, it is necessary to identify the forged area during each cycle. For this particular geometry, the area forged is represented in Figure 4.2 and can be estimated by equations 4.2, 4.3, and 4.4, where: R_m [mm] is the hammer internal radius, L_w [mm] the arc length, *W* [mm] the bead width, and β [º] the angle of the arc half-length.

$$A = F_s \times L_w \qquad \text{Eq. 4.2}$$

$$L_w = \frac{2\pi R_m \times 2\beta}{360} \qquad \text{Eq. 4.3}$$

$$\beta = \sin^{-1}\left(\frac{W}{2R_m}\right)$$ Eq. 4.4

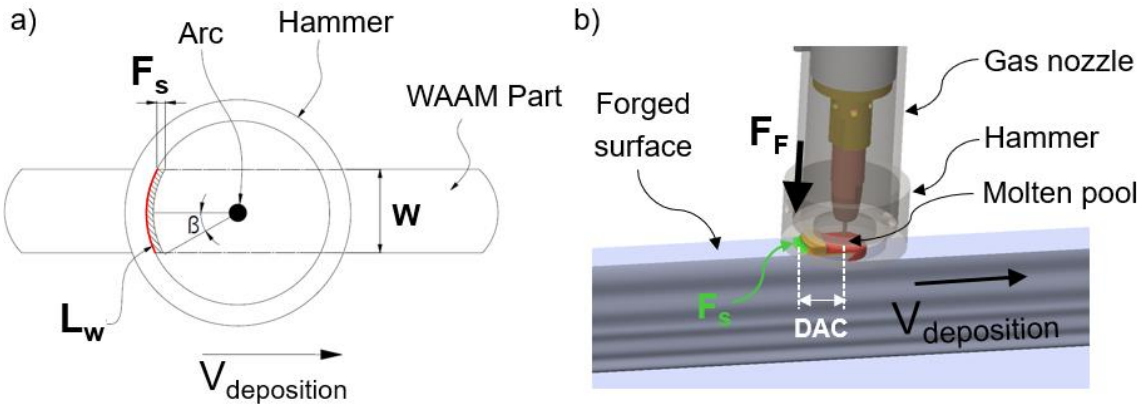

Figure 4.2 - Schematic representation of the forged area at each step: a) top view (2D), b) isometric view (3D)

4.3 Kinematic and dynamic characterization

The speed of the hammer when it touches the deposited material is an important variable of the forging process, as it determines the kinetic energy carried by the hammer, that is later absorbed by the part in the form of plastic deformation. Moreover, the speed of the hammer also determines the forging force. The theoretical final speed of the hammer can be calculated using the equations of the uniformly accelerated motion.

Thus, for the calculation of the hammer speed, and considering the actual system, with two pneumatic actuators with a cylinder radius of 6 mm, the theoretical force exerted by them can be calculated with the equation 4.5, as a function of the pneumatic cylinders radius and the pressure of the compressed air.

$$F = 2(P \cdot 10^6 \cdot \pi \cdot r^2)$$ Eq. 4.5

Where: *r* [m] is the pneumatic cylinders radius, *P* [MPa] is the pressure of the compressed air, and *F* [N] the resultant force.

Considering the static force exerted by the actuators, the acceleration of the hammer during its descent movement can be calculated using the Newton's second law, with a mass of the moving parts of 0.435 kg.

$$F = m \cdot a$$ Eq. 4.6

Where: *m* [kg] is the mass of the moving components, *a* [m/s^2] is the acceleration, and *F* [N] the resultant force exerted by the pneumatic actuators.

Therefore, the uniformly accelerated motion equations can be used to calculate the speed of the hammer at a given moment during its descent, through the equation 4.7. It was also considered that in the downward movement of the hammer, the acceleration of gravity contributes to the movement, so the value of 9.81 m/s^2 was added to the value of the acceleration calculated with equation 4.6.

$$v_f = \sqrt[2]{v_i^2 + 2a\Delta s} \qquad \text{Eq. 4.7}$$

Where: v_i [m/s] is the initial hammer speed (it is null, since the hammer always starts from a resting position), *a* [m/s^2] is the acceleration, Δs [m] is the distance travelled by the hammer and v_f [m/s] is the hammer speed after traveling the distance Δs.

Figure 4.3 shows the calculated and experimental data of hammer speed as a function of the distance travelled. A considerable difference exists between experimental and theoretical values. This result shows that the hammer acceleration is difficult to compute due to the unknown friction in the moving parts and the unknown real dynamic pressure inside the pneumatic cylinders.

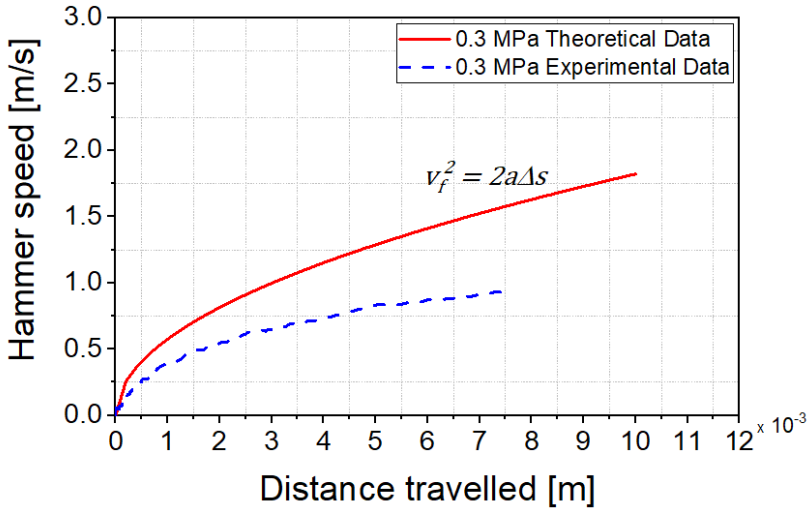

Figure 4.3 - Theoretical and experimental data of hammer speed curve as a function of distance travelled at 0.3 MPa

Therefore, an alternative approach to measure the final speed of the hammer is needed. The velocity was experimentally measured, and the dynamic characterization of the forging mechanism was performed by high-speed imaging. The acquisition of the images was obtained during the vertical movement of the forging system, when a sample was being produced. This method was chosen over others, as it allows the simultaneous evaluation of several factors, such as: the material strain rate, the estimation of the impact force, and the evaluation of the overall performance of the forging system.

For this purpose, a Photron FASTCAM Mini WX50 high-speed camera system was used with the capacity to record from 50 frames per second (fps) at 2048 x 2048 pixels up to 67,500 fps at 256 x 32 pixels. The camera was also equipped with a Nikon AF IKKOR 28-105 mm macro lens. Filming with high-speed cameras requires a greater amount of light as the higher the frame rate, the shorter is the shutter duration, therefore, four 100 W LED floodlights from V-TAC were used to ensure the required levels of lighting. The setup of the high-speed recording system is presented in Figure 4.4.

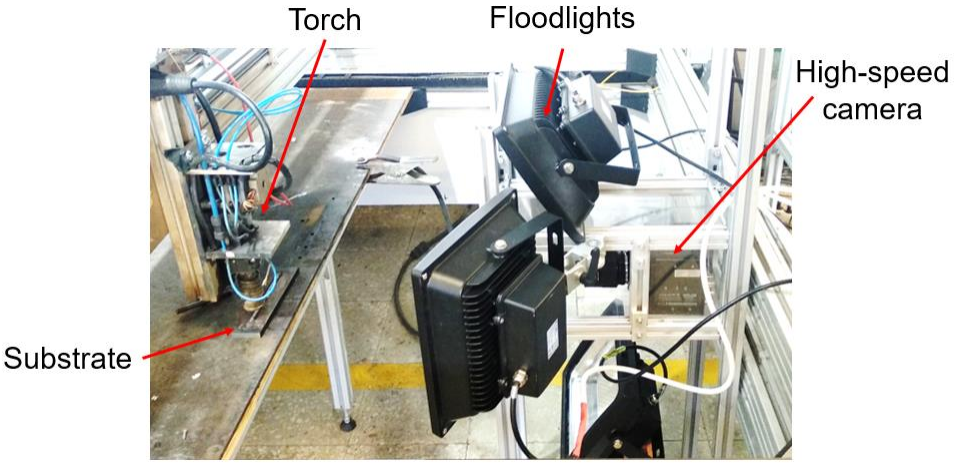

Figure 4.4 - High-speed camera setup

With the increase of the frame acquisition rate, the resolution in pixels of the acquired images decreases, that in this case corresponds to a decrease in the spatial resolution, i. e., the minimum amount of movement that the high-speed camera can distinguish. In practice, the spatial resolution can be expressed through the physical distance that each pixel represents, and it depends on the resolution, lens, zoom and distance from the camera setup to the torch. At higher frame rates the active zone of the camera sensor is a rectangle, therefore, to ensure the maximum spatial resolution possible, the camera was positioned with the longest side of the sensor aligned with the vertical direction.

To process the data obtained with the high-speed camera, a Python software (*vide* Appendix B) was developed in which each acquired frame is binarized with a threshold function and the position in pixels of a mark that moves together with the forging system is acquired. The data obtained are then converted into position (mm) and time (s).

Preliminary tests were performed with the frame rates presented in Table 4.1. From these tests it was possible to conclude that at 5,000 fps the temporal resolution of 0.2 ms is not able to clearly describe the impact between the hammer and the part. Additionally, between 12,500 and 30,000 fps, the spatial resolution is constant and therefore it is always preferred to use the 30,000 fps, which increases the temporal resolution without compromising the spatial resolution.

Table 4.1 - Spatial and temporal resolution of the high-speed camera setup at different frame rates

Frames per second (fps)	5,000	10,000	12,500	20,000	30,000
Resolution [px]	768 x 512	512 x 256	256 x 256	256 x 128	256 x 96
Spatial resolution [mm]	0.0255	0.0382	0.066	0.066	0.066
Temporal resolution [ms]	0.20	0.10	0.08	0.05	0.03

Figure 4.5 shows the results for the acquisition rates of 10,000 fps and 30,000 fps. This acquisition was obtained during the production of 316 LSi stainless steel samples with the same parameters used in Chapter 5. From these preliminary tests, it is observed that under these conditions the best compromise between spatial and temporal resolution is obtained when using an acquisition rate of 10,000 fps, since with higher acquisition rates the spatial resolution is too small and does not allow the correct definition of the position-time curve during the impact between the hammer and the part to be forged. Thus, all the following tests were performed with the acquisition rate of 10,000 fps.

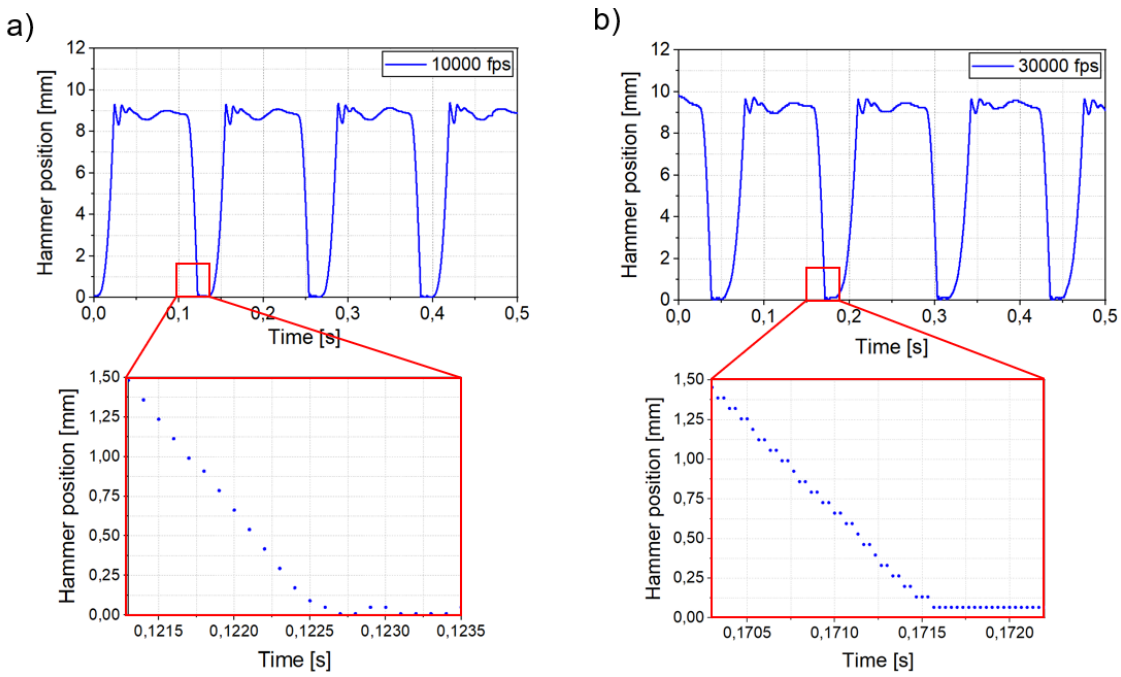

Figure 4.5 - Hammer position along the time during the deposition and forging of a sample, acquired at: a) 10000 fps, b) 30000 fps

From the acquired data (Figure 4.6 c)), it was observed that the impact contact between the hammer and the part occurs almost instantaneously during a very short period (δt). The material deformation starts when the hammer comes into contact with the as-deposited layer, at an average speed computed by $V = \Delta y/\Delta t$. During this initial deformation, the deposited material loses its natural convex shape and accommodates to the planar surface of the hammer, increasing the contact area and therefore the

resistance the material imposes to the hammer movement (Figure 4.6 a)). With the increase of this resistance during δt, the hammer starts to decelerate until it comes into contact with the previously deformed material which is at a lower temperature and acts as a stop for the hammer (stage 3).

The last stage of the deformation is critical in the process, since it is at this stage of deformation, when the hammer decelerates, that the hammer kinetic energy is transferred to the part in production. It must be noticed that the forging force is not a static force, resulting from the static pressure provided by the pneumatic actuators; it is rather an impact force, resulting from the almost instantaneous impact of the mass of the hammer into the deposited material. Consequently, the forging force is considerably higher than the actuating force of the pneumatic actuators.

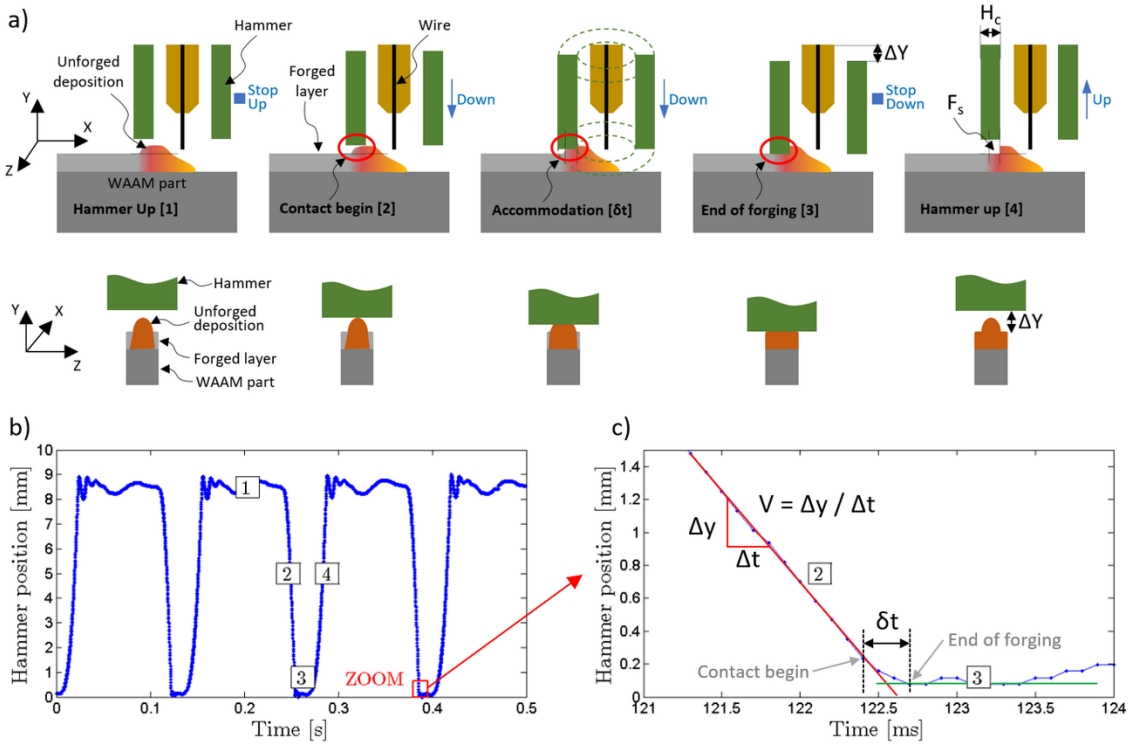

Figure 4.6 - Dynamics of the in-situ hot forging DED-arc during a deposition with forging at F_f = 8 Hz and a duty cycle of 20%. a) Schematic representation of the movement of the hammer during forging, b) Hammer position along the time during the deposition and forging of a sample acquired at 10,000 fps, c) Zoom of b)

4.3.1 Impact force

The impact forging force depends on the hammer speed before contact (V = Δy/Δt) and the impact time, δt, and it can be estimated by using the principle of impulse and momentum (equation 4.8).

$$I = \Delta P = m \cdot \Delta v = F_{avg} \cdot \delta t \quad \text{Eq. 4.8}$$

Where: I [N·s] is the impulse, P [N·s] is the momentum, m [kg] is the mass of the moving hammer parts, Δv [m/s] is the difference between the initial and final velocity of the forging hammer, F_{avg} [N] is the average force during the impact (forging), and δt [s] is the time duration of the impact.

To calculate the average impact force and evaluate the factors that influence it, several samples were produced in which the pressure applied to the pneumatic actuators and the forging frequency were varied, the remaining deposition parameters were maintained constant and are the same used in Chapter 5.

The measurements of δt [s] and V [m/s] were obtained from the data acquired with the high-speed camera, as shown in Figure 4.6 c). The measurements were performed in three consecutive hammer strikes and the average value was calculated. Since the final speed of the hammer is zero, the speed variation (Δv) during the impact is, in absolute value, equal to the speed at which the hammer reaches the part (V).

The results for the measurements, and the calculated average impact force are presented in Table 4.2. For these calculations, a mass of 0.435 kg for the moving components was considered.

Table 4.2 - Hammer speed variation, impact time and average impact force for the stainless steel 316LSi and aluminium 1070 alloy samples

Sample	Δv [m/s]	δt [ms]	F_{avg} [N]
316 LSi with 0.5 MPa and 8 Hz	1.169	0.300	1,695
316 LSi with 0.3 MPa and 8 Hz	0.917	0.300	1,330
316 LSi with 0.3 MPa and 4 Hz	0.901	0.633	653
ER1070 with 0.3 MPa and 8 Hz	0.905	0.533	739
ER1070 with 0.3 MPa and 4 Hz	0.878	0.566	675
ER1070 with 0.3 MPa and 2 Hz	0.889	0.666	587

The results demonstrate, as expected, that both the pressure in the pneumatic actuators and the forging frequency have an influence on the average impact force. It is shown

that the decrease in pressure only has an influence on the speed at which the hammer reaches the part to be forged, with no influence on the duration of the impact.

Additionally, it showed that the forging frequency only has influence on the duration of the impact. In fact, by doubling the frequency there is only half the material to be deformed at each impact, so the impact time is shorter. The influence of the forging frequency on the duration of the impact can also be explained based on the fact that it is directly related to the forging step (Equation 4.1). The lower the forging frequency, the higher the forging step, which means that a greater volume of material is forged for each hammer strike, and therefore, the impact time increases.

As expected, it is also observed that the average impact force also depends on the properties of the forged material, and not only on the forging parameters, since in the stainless steel 316LSi, with the increase of the forging frequency to double, the impac force also doubled, whereas in the aluminium 1070, the same frequency variation only causes an increase of about 10% in impact force.

With the forging system operating in a stable regime, it was expected that the forging frequency does not have any influence on the hammer speed. Actually, this result allows to confirm the capacity of repeatability of the developed system.

4.3.2 Calculation of true strain during hot forging DED-arc

Since hot forging operates in the plastic regime, at constant volume, the calculation of the true strain was chosen instead of the engineering strain.

Using the coordinate system defined in Figure 4.6 for the cross section of the sample: the forging mechanism acts along the Y axis; there are no constraints on the material flow on the Z axis; and the material already deposited along the X axis works as a constraint to the material to be deformed.

Therefore, it was expected the true strain to be almost null along the X axis and to be opposite in the Y and Z axis. However, to confirm, the height and width measurements of the sample layers were performed before and after forging to calculate the true strain in Y and Z axis, respectively (equation 4.9), and by the law of conservation of volume in plastic regime (equation 4.10) the extension in X was obtained. The equivalent true strain was calculated with the equation 4.11. The computed values for the true strain in each axis and the equivalent true strain are shown in Table 4.3.

$$\varepsilon = \ln\left(\frac{l}{l_0}\right) \qquad \text{Eq. 4.9}$$

Where: l [mm] is layer heigh or width after hot forging, l_0 [mm] is layer heigh or width before hot forging and ε is the true strain.

$$d\varepsilon_x + d\varepsilon_y + d\varepsilon_z = 0 \quad \text{Eq. 4.10}$$

Where: $d\varepsilon_x$, $d\varepsilon_y$ and $d\varepsilon_z$ are the true strain of a layer along the X, Y and Z axis respectively.

$$d\bar{\varepsilon}^p = \sqrt[2]{\frac{2}{3}\left(d\varepsilon_x{}^2 + d\varepsilon_y{}^2 + d\varepsilon_z{}^2\right)} \quad \text{Eq. 4.11}$$

Where: $d\varepsilon_x$, $d\varepsilon_y$ and $d\varepsilon_z$ are the true strain of a layer along the X, Y and Z axis respectively, and $d\bar{\varepsilon}^p$ is the equivalent true strain.

Table 4.3 - True strain in the X, Y and Z axis, and equivalent true strain in the stainless steel 316LSi sample

	316 LSi
$d\varepsilon_x$	0.026
$d\varepsilon_y$	0.272
$d\varepsilon_z$	-0.298
$d\bar{\varepsilon}^p$	0.370

As can be seen in Table 4.3, the calculated true strain values for the Y and Z axes are similar in absolute value, as expected, which results in a true strain near zero in the X axis. The fact that the true strain values for the X is not exactly zero may be due to the uncertainty of the measurements, particularly in the measurement of the sample width.

In fact, due to the typical waviness of DED-arc walls, the measurement of width for the purpose of calculating the true strain is uncertain. Thus, and once the results confirm the assumptions presented above, the equivalent true strain for the samples was calculated with the true strain of the Y axis, considering that the extension in Z is the opposite of the Y axis, and that in the X axis is null.

Therefor the equivalent strain achieved in the stainless steel 316LSi was of 0.38, considering an average layer height of 1.67 mm and 1.24 mm before and after the hot forging respectively.

4.3.3 Flow stress curves of stainless steel 316LSi under forging conditions

In order to obtain the stress-strain curve of the material under forging conditions it was calculated the true strain rate of during the process. Considering the particular case of the stainless steel 316LSi, with the previously calculated true strain of 0.38, through the data obtained with the high-speed camera, it was verified that after the contact between the hammer and the part (approximately in the last 0.4 mm of the downward movement of the hammer) the hammer takes an average time to stop of 5.83 µs, which corresponds to an average true strain rate of 660 s^{-1}.

Thus, considering the calculated strain rate value, the chemical composition of the material, and assuming that the final microstructure of the deposited materials contains 90 % austenite and 10 % ferrite [132], the stress-strain curves presented in Figure 4.7 b) were obtained using the *JMatPro* software.

In order to place the stress applied by the hammer on the stress-strain curves, it was necessary to estimate the area over which the hammer applies the impulse force. Considering that for this set of parameters, the width of a deposition is approximately 6 mm and that the forging step is of 0.75 mm, by equation 4.2, the area projected on which the hammer acts is 4.54 mm^2. Considering that the average force calculated was of 1,695 N, the average stress applied by the hammer is of 371.7 MPa.

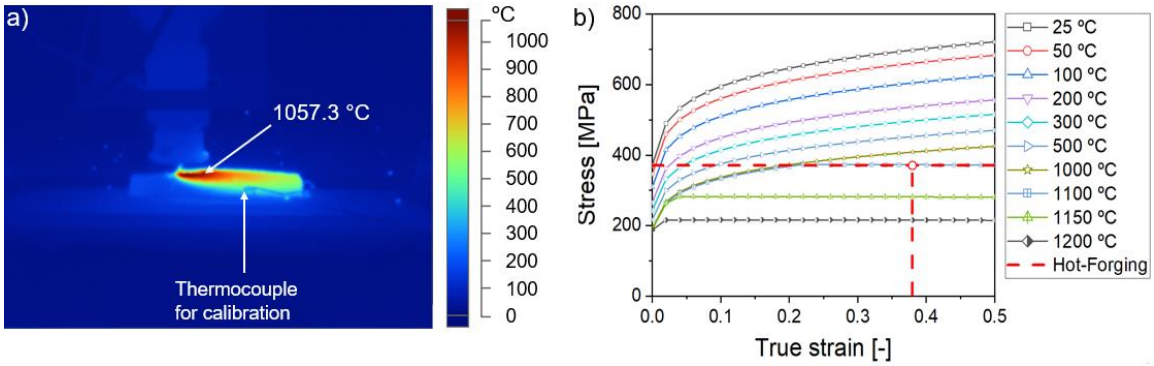

Figure 4.7 – (a) Thermogram obtained during the deposition of the 10th layer showing the forging temperature, (b) stress-strain curves at various temperatures for the stainless steel 316LSi at a strain rate of 660 s^{-1} (obtained from *JMatPro* software)

It is important to notice that the calculated area corresponds to the surface area after forging, and that this area is not constant throughout the forging process, but increases as the material is forged, and therefore the calculated value can be considered an upper bound. Additionally, as it can be seen in Figure 4.8, during forging the maximum force value is greater than the calculated mean value and therefore the calculated force value is a lower bound, thus resulting in the calculated stress value being a lower bound of the actual value.

It is also observed that, for this material, when deformed with a strain rate of 660 s^{-1}, below the temperature of 1100 °C the mechanism of work hardening prevails over the dynamic recrystallization that may occur, while for temperatures above this value it is found that from a certain strain the dynamic recrystallization prevails.

Thus, from Figure 4.7, it is possible to state with certainty that the developed system can act on the part in production, causing a plastic deformation with a strain of at least 10 % for temperatures equal to or greater than 500 °C. Moreover, using the stress-strain curves, and considering the interaction of the horizontal line of the stress applied by the hammer with the vertical line of the measured true strain, it is possible to estimate the temperature at which the material was forged. In this case, it was verified that the forging took place with the material at around 1100 °C. This temperature was also confirmed using thermography, in which it was measured a forging temperature of about 1057 °C thus validating the temperature estimated through the flow stress curves.

The fundamental principles of the developed forging system are similar to the commercial powered drop hammers, where the downstroke, in addition to gravity, is also accelerated by steam or compressed air. The pulse loads resulting from the hammer-part impact can take different shapes depending on: the load transferred from the hammer to the forged material, the size and shape of the part and the material properties and temperature [133], however, they often have a maximum strength value considerably higher than the average strength value, since these impulse loads are usually short-term with high intensities that does not change the direction of its action and has only one maximum, during the pulse duration δt.

A typical form of a load pulse that occurs in a powered drop hammer forging process is shown in Figure 4.8.

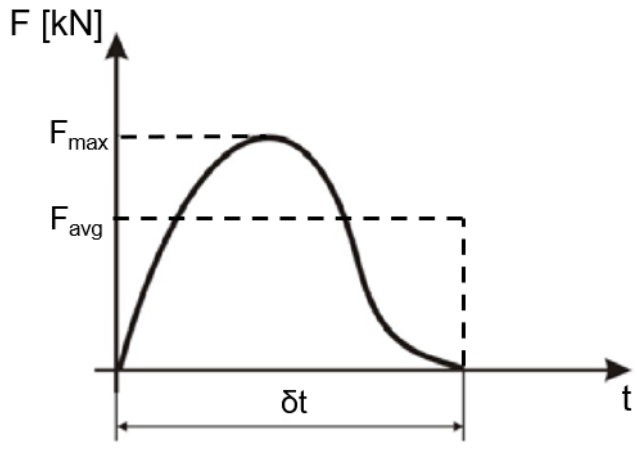

Figure 4.8 - Single load impulse representation powered drop hammers, adapted from: [133]

4.4 Hot forging system validation in multi-layers

Since DED-arc is a process that builds up a part with a complex geometry through the deposition of weld beads on a layer-by-layer basis, it is also important to assure that the hot forging mechanism is not only possible to implement in single bead but also in multi-bead parts.

To validate the forging system ability to produce multi-bead layers, a sample of stainless steel 316LSi was produced according to the configuration shown in Figure 4.9 a), where each bead is numbered according to its deposition order. For example, bead B2:3 corresponds to the third deposition of the second layer. Additionally, the length of the first layer was 100 mm and the following layers were consecutively reduced to 75 mm and 50 mm, in order to allow the individual evaluation of each layer. Figure 4.9 b) shows a photograph of the piece produced.

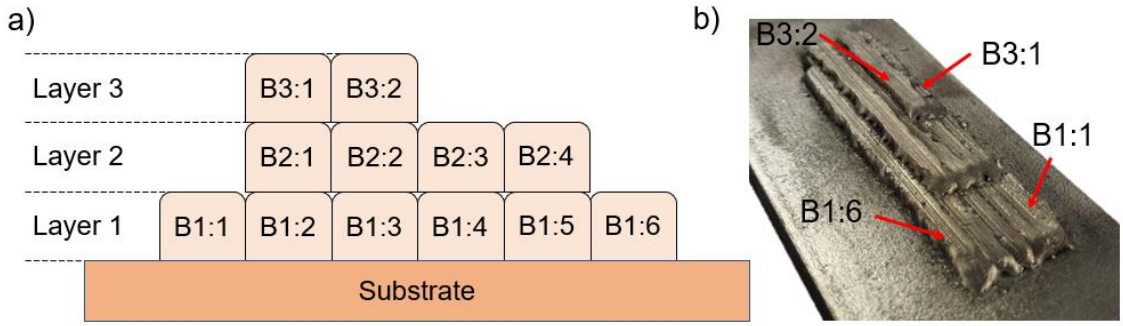

Figure 4.9 - Multi-bead sample produced with the hot forging system: a) deposition configuration; b) photograph of the produced sample

One of the most important parameters in multi-bead deposition is the amount of overlap between adjacent beads. The definition of this parameter was made based on the bibliography, in particular the work of Donghong Ding et al. [134], which states that the optimal distance between the center of consecutive depositions (d_{center}) is equal to 73.8 % of the width of a single bead. Therefore, the width of a single bead deposited with hot forging was used as reference. Additionally, preliminary tests were also carried out in which this value was varied, it was verified that for lower values, the appearance of the stair effect occurs (where the layers are cumulatively overlapping) and for higher values, a void between adjacent layers is formed occasionally, with no connection between them.

Also during the preliminary tests, it was observed that the different heat flow conditions between the deposition of the first bead and the remaining beads of each layer is sufficiently different to considerably affect the forging conditions. In the first deposition of each layer, most of the heat is dissipated in a vertical orientation to the previous deposited layer or substrate, while in the deposition of the second and consecutive beads the heat flow occurs vertically in the same way, but also in the horizontal direction to the

previous deposited bead. As a result, the heat dissipation of the first bead of each layer is more constrained than for the remaining beads of the same layer, which changed the temperature at which the material was forged by the hammer, with the first bead being forged at a higher temperature than that of the remaining beads.

Since the forging parameters (*P* and F_f) are constant throughout the entire sample, the difference in the forging temperature between the first and the remaining beads turns into differences in the amount of plastic deformation promoted by the hammer, resulting in a height difference between adjacent beads and therefore an uneven upper surface.

Additionally, without any kind of correction, this effect causes the deposition of the second bead to be excessively overlapped with the first, creating a stair effect, that propagates along several beads within the same layer, making the deposition unfeasible. To solve this, the deposition parameters of the first bead of each layer were changed in order to lower their heat input and equalize the forging temperature between the depositions, which results in a more homogeneous plastic deformation within the same layer.

In Table 4.4 are presented the process parameter used to deposit the material.

The remaining process parameters were kept constant throughout all the depositions, where 99.999% pure Argon was used as a shielding gas with a flow rate of 15 L/min, and the dwell time between the deposition of each bead was of 60 s. Regarding the forging parameter, the hammer had a distance to arc center (DAC) of 10 mm, the forging pressure was 0.5 MPa, the forging frequency was 8 Hz, and the duty cycle was 20%.

Table 4.4 - Process parameters for multi-bead part deposition

	TS [mm/min]	WFS [m/min]	Arc voltage [V]	CTWD [mm]	d_{center} [mm]
B1:1, B2:1 and B3:1	420	4	21	8	4.75
Remaining beads	300	4	21	8	4.75

The variation of the travel speed in the first deposition allowed to attenuate the stair effect and enabled the production of the full part, however, it was not completely eliminated. The sample was sectioned in three distinct zones, as showed in Figure 4.10. In all the three deposited layers the stair effect between the first and second beads is visible, but unlike when all layers were deposited with the same parameters, it does not propagate. This effect is particularly notable between the first and third bead, while from the third bead and forward the height was constant.

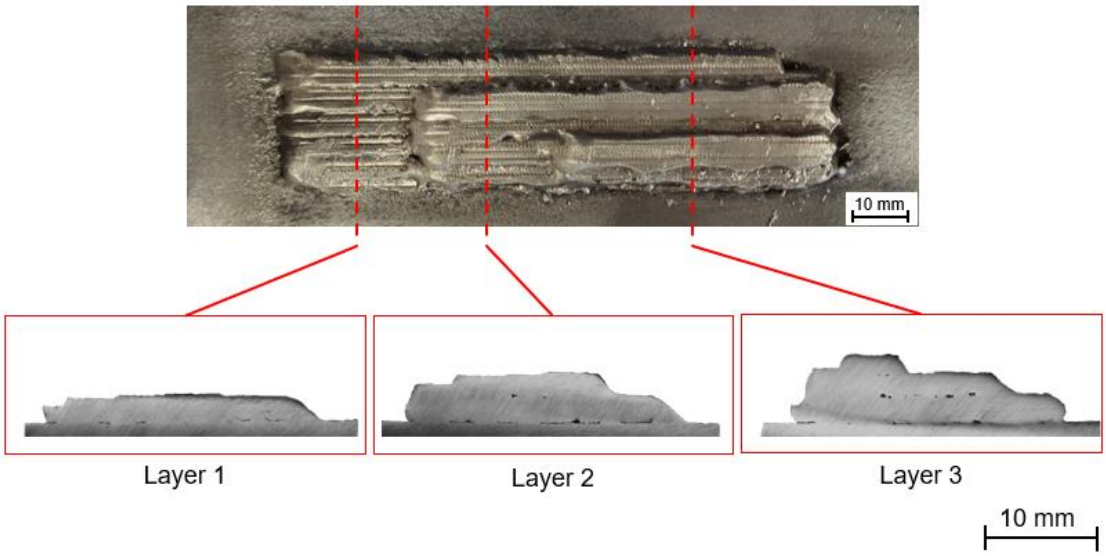

Figure 4.10 - Top view of the produced samples and sections of zones where there are only one layer deposited, two layers deposited, and three layers deposited

Additionally, in the cross sections of the sample, it was also observed the presence of several lack of fusion defects between superposed layers, however no lack of connection between side-by-side beads was observed.

However, this type of defects is also quite common in multi-bead conventional DED-arc, which typically result from a wrong choice of the overlapping distance. Since, the deposition conditions with hot forging are quite different from the ones with conventional DED-arc, the optimal overlapping distance value of 73.8 % of the width of a single bead, established by Donghong Ding et al. [134], is not suitable for the deposition with hot forging, requiring an adjustment of parameters to mitigate the lack of fusion.

To conclude, it has been shown that the use of hot forging during deposition does not hinder the deposition of side-by-side beads and despite the lack of fusion defects, these do not represent an extra difficulty to those that already exist in the deposition trough conventional DED-arc. The hot forging further adds the fact that it promotes a relatively flat top surface. This flat surface add several advantages to the process, particularly, the reduction of the difficulty of coupling probes to perform non-destructive tests such as the ultrasonic, eddy currents or other inspection methods. Additionally, any component that is built by depositing a series of overlapping beads is usually subjected to a machining process to remove the scallops [134]. With the flat upper surface promoted by the hot forging, the amount of material that needs to be removed is considerably less than the one that would be removed in a part produced by conventional DED-arc.

4.5 Summary

In chapter 4, the average impact force exerted by the hammer on the part during forging was calculated for different forging conditions, where it was concluded that:

- Both the pressure and the forging frequency have an influence on the average impact force;

- A decrease in pressure of 0.2 MPa promotes a decrease in the speed at which the hammer reaches the part, reducing the average impact force from 1,698 to 1,330 N;

- An increase of the forging frequency from 4 to 8 Hz decreases the duration of the impact and increase the average impact force from 653 to 1330 N in the stainless steel 316LSi and from 675 to 739 N in the aluminium 1070;

The flow stress curves for stainless steel 316L under forging conditions were obtained and compared with the pressure exerted by the hammer on the material, and it was verified that the hot forging can perform plastic deformation with a strain of at least 10 % when forging the material at temperatures equal to or greater than 500 °C.

Lastly, it was also verified that the hot forging system does not impose additional difficulties with regard to the production of multi-bead and multi-layer parts, instead it adds a flat upper surface that facilitates the subsequent application of tests non-destructive and reduces the amount of material removed in the case of further machining finishing operations.

5

Chapter 5
Evaluation of the forging effect in different materials

5.1 Introduction

This chapter presents and discusses the results of hot forged additive manufactured samples produced in different materials. For each one, two sets of samples were produced, one with hot forging and the other as-built, to assess the hammer effect in the parts characteristics. These comprise geometrical, microstructural, mechanical and electrical properties. Stainless steel 316 LSi was studied in-depth due to its industrial and economic importance, but other materials were studied to evaluate the feasibility of HF-DED-arc in each specific material, though a less detailed characterization was performed.

5.2 Materials and methods

5.2.1 Materials and characterization methods

Since this is a new variant of DED-arc with similarities to other ones but with a major difference in terms of applied load and mode of application, several materials were studied to understand which characteristics of the materials can be enhanced or hindered when processed by HF-DED-arc. For that, a detailed characterization was carried out on stainless steel 316 LSi and several other materials, with different properties and industrially relevant, aiming to assess the applicability of the new variant to manufacture components by AM.

The effects of forging materials are well known from the literature [135]. Cold forging improves the mechanical properties of the material by hardening it at room temperature, while with hot forging, optimal yield strength, and high ductility are achieved by hardening the material at high temperatures that are usually higher than 70 % of the fusion temperature [136].

During hot forging of a material there are two main concurrent microstructural mechanisms that determine the material microstructure, the dynamic recovery and dynamic recrystallization, that prevents the accumulation of defects (dislocations) generated during deformation [137,138]. The dynamic recovery is a softening mechanism that reduces the dislocations density. Thus, in order to improve material strength, the dynamic recrystallization must be predominant [139].

Although those are the same mechanisms that govern microstructural changes during the application of hot forging in DED-arc, there are other factors that when combined with forging can influence the material microstructure, such as the repeated thermal cycles, cooling rates, and percentage of the previous layer that is remelted.

Therefore, the material selection considered thermal and mechanical properties, such as: thermal conductivity, melting temperature, yield stress, ultimate tensile strength and elongation at break. Studied materials were:

- Stainless steel 316L (ER316 LSi);
- Mild steel (ER70S-6);
- Stainless steel 410 (ER410 NiMo);
- Aluminium 1070 (ER1070);
- Inconel 625 (ERNiCrMo-3);
- Monel 400 (ERNiCu7);
- Copper—aluminium alloy (ERCuAl-A2);

The chemical composition of each material is depicted in Table 5.1 and mechanical and thermal properties are shown in Table 5.2.

Table 5.1 - Chemical composition of the wires used (wt. %) [140]

	C	Si	Mn	Cr	Ni	Ti	Mo	Nb	Cu	Fe	Al
ER316 LSi	0.02	0.8	1.8	18.5	12.5	--	2.6	--	--	Bal.	--
ER70S-6	0.10	0.9	1.5	0.03	--	--	--	--	0.20	Bal.	--
ER410 NiMo	0.05	0.6	0.6	13.5	4.50	--	0.5	--	--	Bal.	--
ER1070	--	<0.2	--	--	--	--	--	--	<0.1	--	Bal.
ER NiCrMo3	0.10	0.5	0.5	21.5	Bal.	0.40	9.0	3.5	0.5	5.0	0.4
ER NiCu7	0.15	1.3	3.5	--	65.0	2.00	--	--	Bal.	2.5	1.3
ERCuAl-A2	--	--	<1.0	--	<1.0	--	--	--	Bal.	1	8

Table 5.2 - Mechanical and thermal properties of the deposited materials [140]

	YTS (MPa)	UTS (MPa)	Elongation at Break (%)	Thermal Conductivity (W/m K)	Melting temperature range (˚C)
ER316 LSi	248	538	50	15	1375-1400
ER70S-6	420	528	28	54	1425-1540
ER410 NiMo	1076	1363	25	25	1480-1530
ER1070	84	118	23	229	640-655
ER NiCrMo-3	468	928	48	9.8	1290-1350
ER NiCu7	215	600	44	21.8	1300-1400
ERCuAl-A2	200	475	35	83	1053-1100

The samples were prepared for metallography and microhardness test as described in Appendix A. The metallographic analysis was conducted using a Leica DMI 5000 M inverted optical microscope to verify the existence of significant changes in the microstructure. The grain size of the samples was measured using the open-source software *Image J.*

X-ray diffraction was performed at beamline P07 High Energy Materials Science (HEMS) of Petra III/DESY, using a wavelength of 0.1426 Å (87.1 keV) and an incident beam of 1 × 1 mm. A Perkin-Elmer detector, with a pixel size of 200 x 200 µm, was placed at 1.40 m from the sample. LaB6 powder was used for calibration. The raw 2D Debbye-Scherrer images provide qualitative information on the grain size and texture of the analysed material

Microhardness indentations were performed along the vertical direction in the middle of the sample's section, using a Mitutoyo HM-112 Micro-Vickers Hardness testing machine. The distance between each indentation was of 1 mm for all the samples. Since the

materials presented different hardness values, the load was adapted for each material, in order to increase the test accuracy. For the aluminium alloy a load of 0.2 kg, and for the remaining tested materials the load was of 0.5 kg. All the indentations were performed with a load period of 10 s.

Uniaxial tensile and compression tests were performed on an Autograph Shimadzu machine model AG500Kng equipped with a Shimadzu load cell SFL-50kN AG with a total capacity of 50 kN. A crosshead displacement speed of 0.01 mm/s was imposed, and the tests were performed at room temperature. For both tensile and compression tests, three specimens for each condition were evaluated to assess the reproducibility of the parts mechanical properties. The fracture surfaces of both as-built and hot forged samples were analysed by a TM3030 Plus Voltage Tabletop Scanning Electron Microscope (SEM) at an acceleration voltage of 15 keV.

A Fluke TI400 thermographic infrared camera was used to monitor the temperature of the parts during fabrication. The camera had an accuracy of ± 2 %, a measurement limit of 1200 °C, a refresh rate of 9 Hz, and a resolution of 320 × 240 pixel. The emissivity was calibrated for each analysed material by placing thermocouples on the surface of the sample visible in the thermography and adjusting the emissivity value until the temperature measured with the thermocouples match the temperature measured with the thermography. The temperature was measured at any point during the build-up using the acquisition software SmartView.

Eddy current measurements were performed to access the microstructural homogeneity and variations on processed materials [98]. It was used an absolute helical shielded EC probe, with 3 mm diameter, operating in bridge mode and Olympus Nortec 500C impedance measurement equipment. A customized probe positioning system with a precision of 0.125 mm was used, and the measurements were obtained along a vertical line in the centre of the cross-section with a sample rate of 4 kHz.

In all samples the test frequency was set at 350 kHz, and the angle at 219º in order to align the variation in electrical conductivity with the imaginary axis. The gain was changed for each material to maximize the output signal. To convert the output signal into %IACS, measurements in standard materials with electrical conductivity like the one of the materials under test were performed to obtain the calibration equation.

5.2.2 Processing

For each material, an optimization of processing parameters was carried out aiming to obtain a stable deposition with constant power and deformation, and without defects visible to the naked eye.

It was also aimed to minimizing the wire feed speed to not increase the penetration depth of the layers, thus avoiding remelting the entire area of the microstructure affected by

the forging. Additionally, wire feed speed significantly affects the temperature distribution along the part, and therefore the forging temperature of the material, thus the choice of the deposition parameters was also conditioned by this, and the main criterion for choosing the parameters was to obtain a constant and uniform deformation along each layer.

After this optimization, two sets of samples were produced in each material with the same process parameters: one set with hot forging and the other without.

The samples were manufactured with a *PRO MIG 3200* power source from *KEMPY* with a length of 100 mm each, with 10 layers. Argon 99.99 % was used as shielding gas. The deposition strategy was the Zig-Zag, i.e. consecutive layers were deposited in opposite directions, to avoid the difference in height between the beginning and end of the part. The remaining process parameters used to produce the samples are shown in Table 5.3.

Table 5.3 - Process parameters for the deposited materials

Material	ER316 LSi	ER70S-6	ER410 NiMo	ER1070	ER NiCrMo3	ER NiCu7	ERCuAl-A2
DED-arc parameters							
WFS [m/min]	4	3	4	4	3	4	4
Current RMS [A]	83.5	72.9	83.2	36.3	62.0	86.4	71.7
TS [m/min]	0.36	0.36	0.36	0.36	0.36	0.36	0.36
GFR [L/min]	15	15	15	20	15	15	15
Welding mode	CW	CW	CW	PW	CW	CW	CW
Interlayer Time [s]	60	90	6	30	60	6	15
Voltage [V]	19	19	19	19	19	19	19
CTWD [mm]	8	8	8	10	8	8	7
Forging parameters							
DAC [mm]	12.5	12.5	12.5	10	10	12.5	12.5
Frequency [Hz]	8	8	8	8	8	8	8
Duty cycle [%]	20	20	20	20	20	20	20
Pressure [MPa]	-	0.5	0.5	0.5	0.5	0.5	0.5

CW – Continuous wave

PW – Pulsed wave

CTWD – Contact tip to work distance

DAC – Distance to arc centre

5.3 Results and discussion

The results are organised and presented per material. For each one, the results of microscopy, hardness and conductivity measurements are presented and discussed. Stainless steel 316LSi was studied in-depth while the others were characterised in a less detailed way.

5.3.1 In-depth study of the forging effect on structural and mechanical properties of the 316LSi stainless steel

In order to evaluate the effect of hot forging on the material structural and mechanical properties, three samples with different forging forces were manufactured with 316LSi stainless steel.

The material was deposited on a mild steel substrate with a thickness of 8 mm. The process parameters used to deposit and deform the material are shown in Table 5.3. Additionally, the samples were intentionally repeated without the use of shielding gas to promote the formation of pores, and thus characterize the feasibility of the hot forging variant in collapsing and reducing porosity in the parts. Figure 5.1 shows the overall aspect of the samples.

With a one-way strategy, i.e. all the layers deposited in the same direction, wherein the torch always returned to the same starting point, it is commonly observed a difference in height between the beginning and end of the deposition. This occurs due to rapid cooling and the small amount of heat accumulated at the beginning of the deposited layer, in opposition to a large amount of heat accumulated at the end of each deposited layer. Therefore, the samples were produced with this strategy to evaluate whether the hot forging was able to mitigate this feature.

It was evident that the hammer has a considerable impact on the bead geometry as it flattens the layers along its length, thereby diminishing this feature that needs inline parametric correction and assists deposition of the subsequent layer. The flat-top surfaces in this variant are achieved due to the constant effect of the hammer. Since deformation is occurring always at the same distance of the electric arc, the material temperature and deformation conditions are kept constant through the deposition. Furthermore, the forging step in the deposition was 0.6 mm.

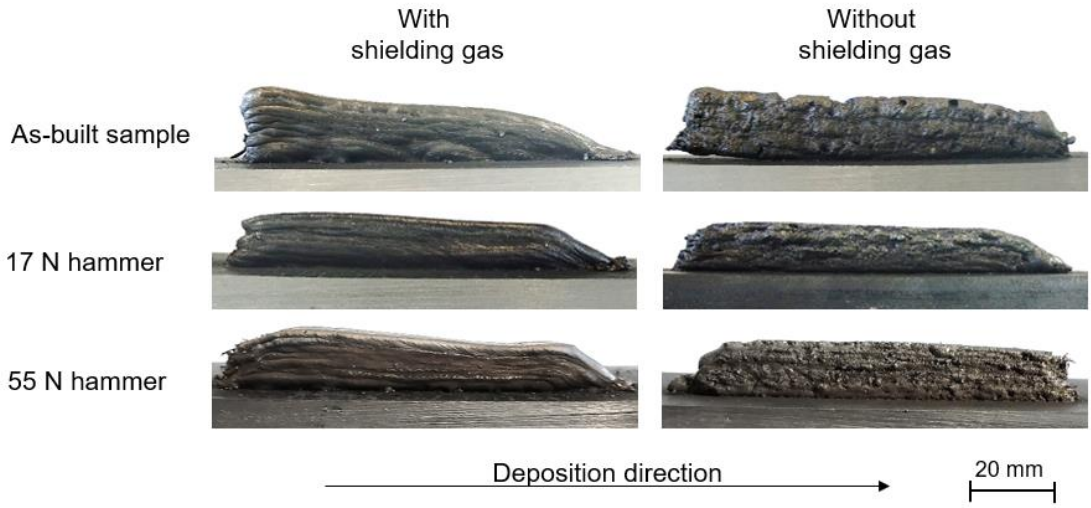

Figure 5.1 Overall aspect of the samples produced with different forging parameters

The macrographs of the cross-sections removed from each of the samples produced with shielding gas are shown in Figure 5.2. The effects of the hammer are evident: the layers are wider and thinner when the forging forces increase, and this is particularly evident for the sample in which the hammer applied a force of 55 N.

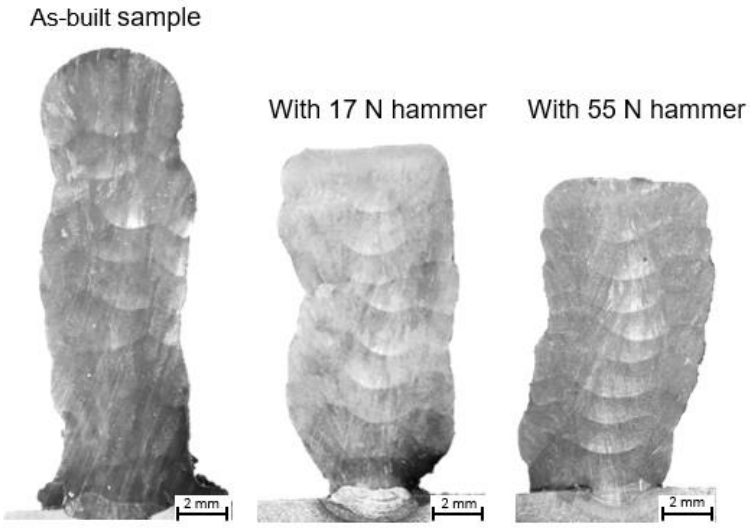

Figure 5.2 - Cross-section of the samples produced with different forging loads and shielding gas Ar 99.99%

The width and height of each part were measured. The respective average and standard deviation values are shown in Figure 5.3 where the part dimensions are compared to the as-built (control) specimen. The height of the layers decreases at higher forging forces, while the width increase because of volume conservation in the plastic deformation domain. An equivalent true strain of 0.21 and 0.33 was calculated for the 17 N and 55 N hot forged samples, respectively, according to equation 4.11.

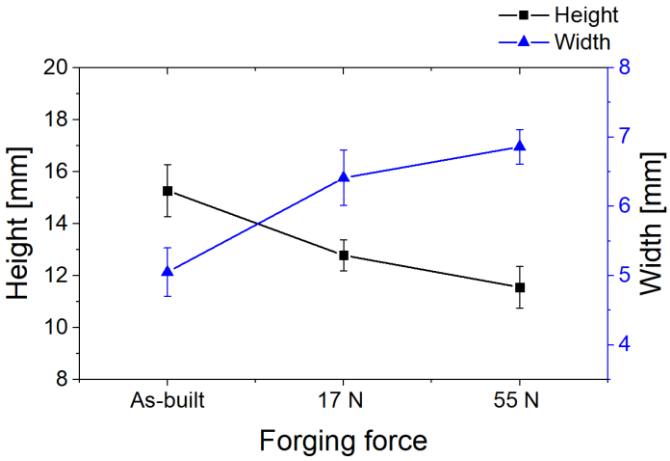

Figure 5.3 - Height and width measurements of each sample

Samples without shielding gas were intentionally produced to induce the formation of pores and access the effect of hot forging in this porosity.

In the as-built parts, most porosities had a spherical geometry. The hot forging was seen to reduce the number of pores in the central zone of the sample. Due to the curvature exhibited by the as-built beads, the central zone deforms first and the pores tend to migrate to the borders.

Increasing the forging force, the pores become oval and at a forging force of 55 N, it was observed that several pores were fully collapsed (Figure 5.4). Despite having collapsed, it was observed by microscopy, that the conditions used did not allow the complete connection of the end sides of the pores.

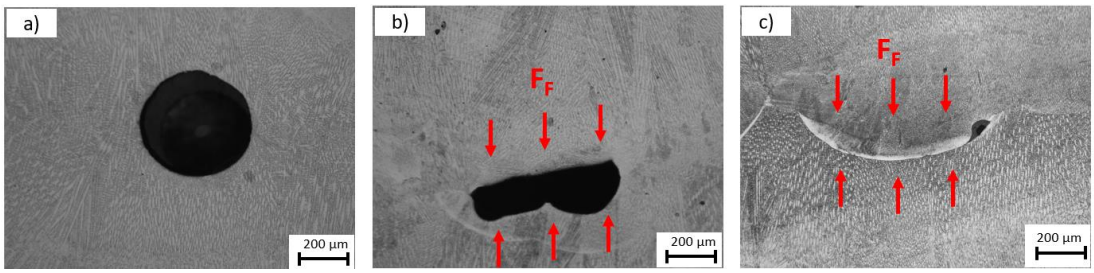

Figure 5.4 – Examples of pores in as-built parts a), with a 17 N forging force b) and c) with a 55 N forging force

Microstructure

The grain size and morphology are determined by the solidification conditions during the liquidus/solidus temperature range. In non-equilibrium solidification, as observed in additive manufacturing, the parameters that mostly affect the solidification microstructure include the temperature gradient (G), solidification rate (R), undercooling (ΔT), and alloy composition [141]. In DED-arc of 316L stainless steel, a cellular or columnar-dendritic structure is commonly observed, and that occurs when G is low and/or R is high [142].

A dendritic structure grows in the direction of heat flow and perpendicularly to the isotherms. Secondary arms are insipient due to the rapid cooling.

Figure 5.5 shows optical micrographs of transverse sections of each sample. Primary austenite (γ) dendrites are observed with some δ ferrite in the interdendritic spaces. This structure results from a short cooling time that limits the δ to γ diffusion-controlled transformation [142]. The micrographs also show the competitive grain growth between layers which modify the dendrites size and orientation. When hot forging was applied, this epitaxial grain growth is no longer visible, dendrites broke resulting in a decrease in grain size.

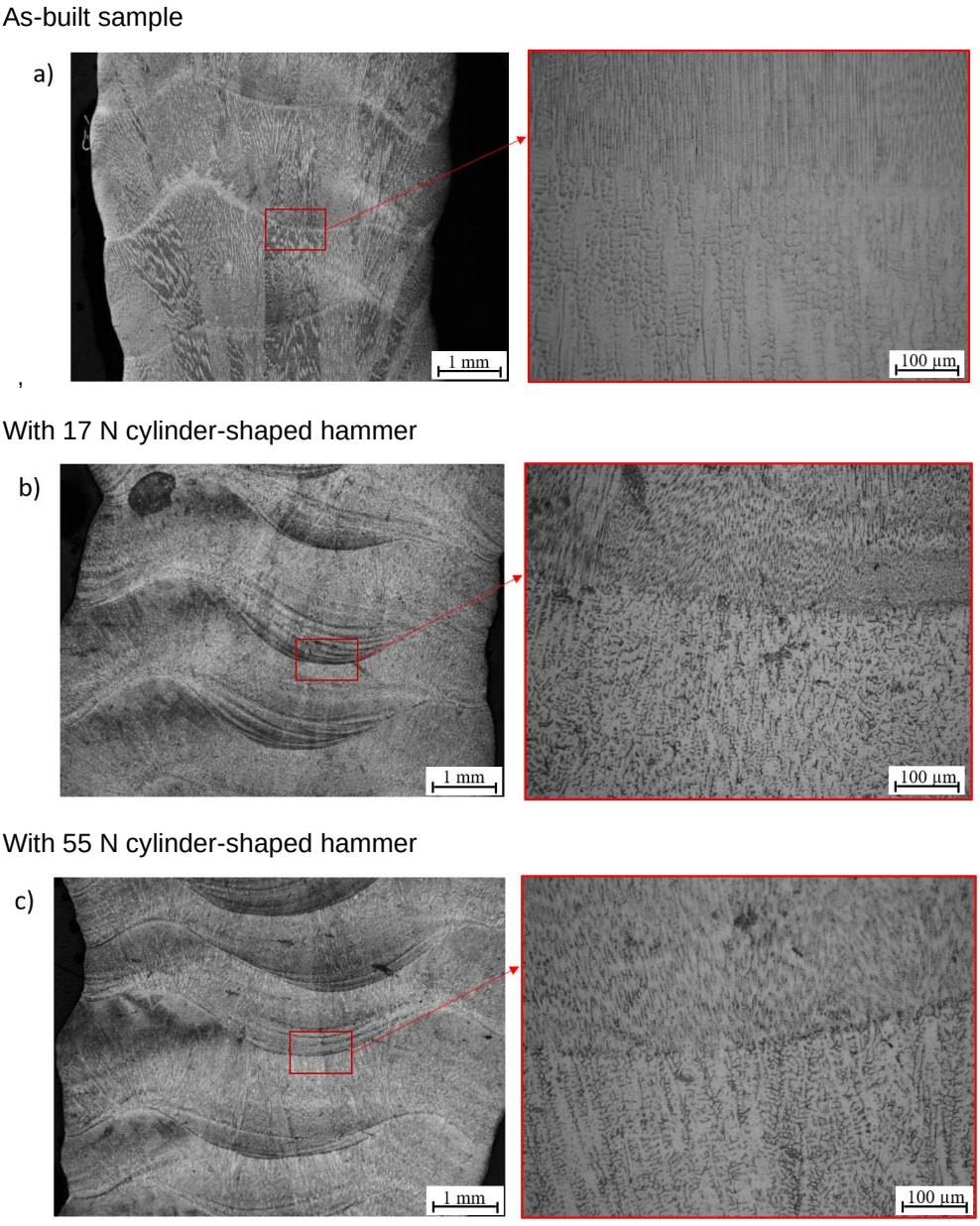

Figure 5.5 – (a) Micrographs of the as-built, (b) hot forged with 17 N cylinder-shaped hammer, (c) hot forged with 55 N cylinder-shaped hammer

On both the as-built and hot forged samples, each layer presented the same grain growth pattern with a fine cellular dendritic structure at the bottom, that develops into a coarse dendritic structure with secondary arms near the fusion line at the top of the layer (Figure 5.6). In DED-arc, most of the heat is dissipated through the previously deposited layers, and thus, the cooling rate decreases from the bottom to the top of the layer, which promotes a finer microstructure at the bottom, due to the insufficient time to form dendrites with secondary arms, and a coarser one at the top [50]. Additionally, the top region of each layer is also refined by the subsequent layer.

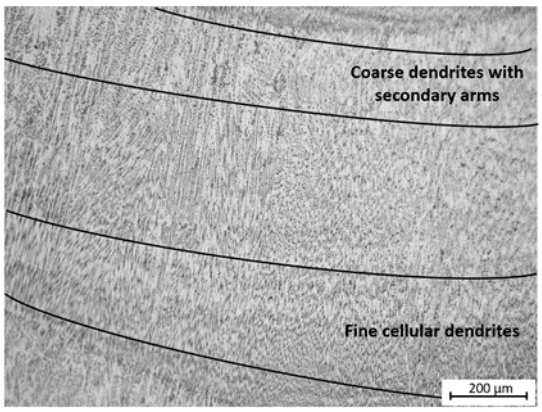

Figure 5.6 - Micrograph of the as-built sample, in which regions with fine and coarser dendrites developed within a single deposited layer are highlighted

The quantitative evaluation of the effect of the hot forging on the microstructure of the parts was made by measuring the grain size. With the software *Image J*, average dendrite arm spacing was measured in groups of 5 consecutive dendrites arms. The methodology was repeated seven times to obtain an average and standard deviation value for each analysed sample.

From the comparison of both secondary and primary dendrite arm spacing, (SDAS) and (PDAS), respectively, it is seen that hot forging promoted a finer solidification structure with smaller primary and secondary dendrite arm spacings (Figure 5.7). However, although there is a clear difference between the as-built sample and the hot forged samples, the increase in the forging force, from 17 N to 55 N, did not cause significant changes in the grain size and morphology.

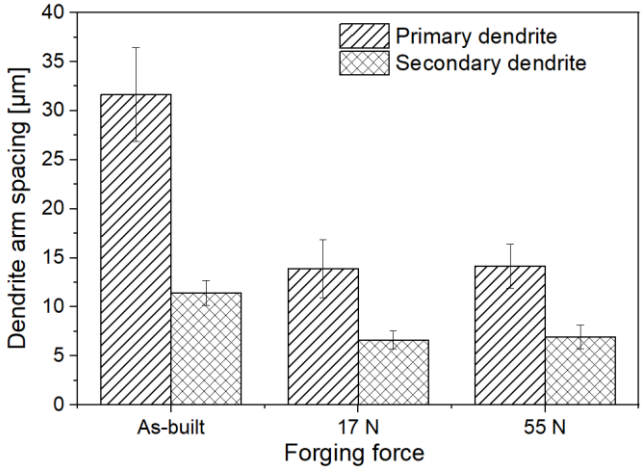

Figure 5.7 - Primary dendrite arm spacing and secondary dendrite arm spacing measured in each sample

In HF- DED-arc, grain refinement due to forging causes the presence of more heterogeneous nucleation sites. As a result, upon solidification, more grains form, and the grain size of the layer is reduced. The high-temperature plastic deformation induced by the HF- DED-arc variant results in a grain refinement effect, which in turn contributes to increase the strength of the parts.

Vickers microhardness tests were performed in as-built and 55 N hot forged samples and are shown in Figure 5.8.

In agreement with the observed in the microstructure, the hot forged sample has higher hardness values due to the finer microstructure, with an average increase of 11 HV. Additionally, the last layer of the hot forged sample shows a sharp increase in the hardness value due to the refined microstructure induced during the hot forging.

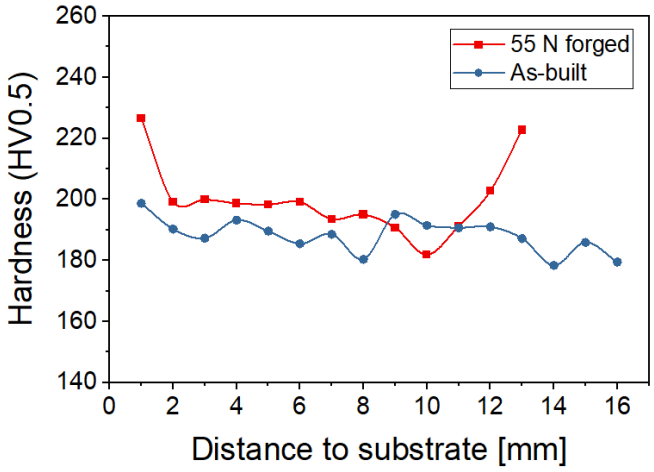

Figure 5.8 - Microhardness profiles of the as-built (blue) and 55 N forged (red) stainless steel 316LSi samples

X-ray diffraction Synchrotron

The 2D Debbye-Scherrer diffraction rings of the as-built and hot forged samples are depicted in Figure 5.9. By analysing the Debye-Scherrer Rings of the as-built sample, spotty diffraction rings with high intensity at different azimuthal angles are visible. This is indicative of a material with large grain size and a marked texture. Both the grain size and texture occur in the as-built sample since the solidification microstructure is continuous (columnar grains) through the height of the wall.

Opposite to this, in the hot forged sample, continuous diffraction rings were observed, indicating a more isotropic fine-grained microstructure with no significant texture, in good agreement with the observed in the microscopic analysis. Thus, it is possible to confirm the effect of hot forging on the material anisotropy, where by refining the microstructure, a more isotropic microstructure is also obtained, with isotropic mechanical properties.

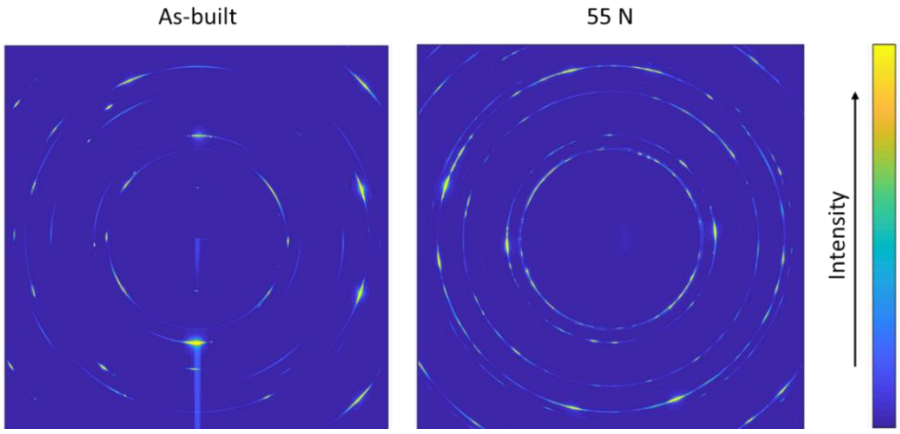

Figure 5.9 - 2D Debbye-Scherrer diffraction patterns of the as-built (left) and hot forged (right) samples.

Mechanical properties and fracture surface

Mechanical properties were evaluated in specimens removed from the as-built and 55 N hammered samples in the vertical direction and prepared for tensile tests. Stress-strain curves are depicted in Figure 5.10. The average values for the ultimate tensile strength (UTS) of the as-built and hot forged samples, were of 574 and 622 MPa, respectively, while the elongation varied from 32.5 to 27.9 %. The samples produced with the hot forging exhibited on average an increase in the UTS of 8.6 % and a decrease of 13.9 % in the elongation. Additionally, the yield strength also increased from 360 to 450 MPa with the application of hot forging during the deposition.

These results are in agreement with the Hall-Petch equation, which states that smaller grain size, as observed in the forged samples, results in a higher yield stress [143], as evidenced in the tensile tests depicted in Figure 5.10. The grain size reduction increases the number of grain boundaries that difficult the dislocation slip, and thus, increases the material strength. It should also be noticed that the increase in the UTS is accompanied

by a decrease of elongation, a measure of ductility, which is again in agreement with the effect of grain size on the mechanical properties of most engineering materials [144].

Nevertheless, it must be emphasized the small loss of ductility observed, which does not prevent the use of 316LSi stainless steel in most industrial applications where ductility is required. Additionally, the as-built samples have mechanical properties that do not comply with the ASTM A666-15 standard [5], while with the increase in the UTS, at the expense of a slight decrease in ductility, the values obtained for the sample hot forged with 55 N are between the values stipulated by the standard for the AISI 316 LSi cold rolled to its 1/16 and 1/8 hard conditions.

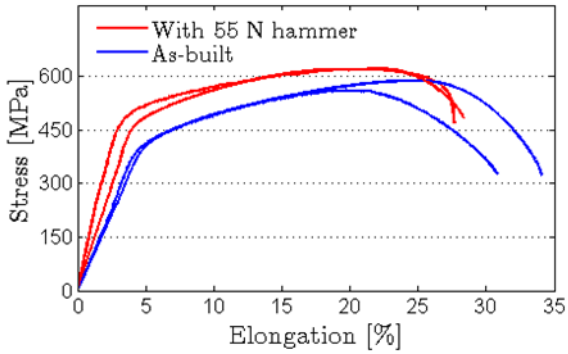

Figure 5.10 - Uniaxial tensile stress-elongation curves for the as-built and 55 N hammered samples

The fracture surfaces of the as-built and forged at 55 N were observed in a scanning electron microscopy (SEM), and are depicted in Figure 5.11. Fractography analysis reveals that both specimens have a ductile fracture, consisting of well-developed dimples over the entire fracture surface. The average dimple diameter of both samples was of 2.4 μm, in the as-built sample and of 1.2 μm in the hot forged sample with a hammer force of 55 N. These results are in good agreement with what was observed in the microstructure, where a decrease in the grain size of about 50% was measured. The fact that the size of the dimples does not match with the width of the previously measured dendrites is due to the plastic deformation that occurs during the tensile test, increasing their length and reducing the section. These results confirm that the hot forging during deposition promotes a grain size reduction resulting in an increase of the grain boundary density and thus improved mechanical properties.

Contamination of the part by the hammer was never seen with the techniques used: optical and scanning electron microscopies, and x-ray diffraction.

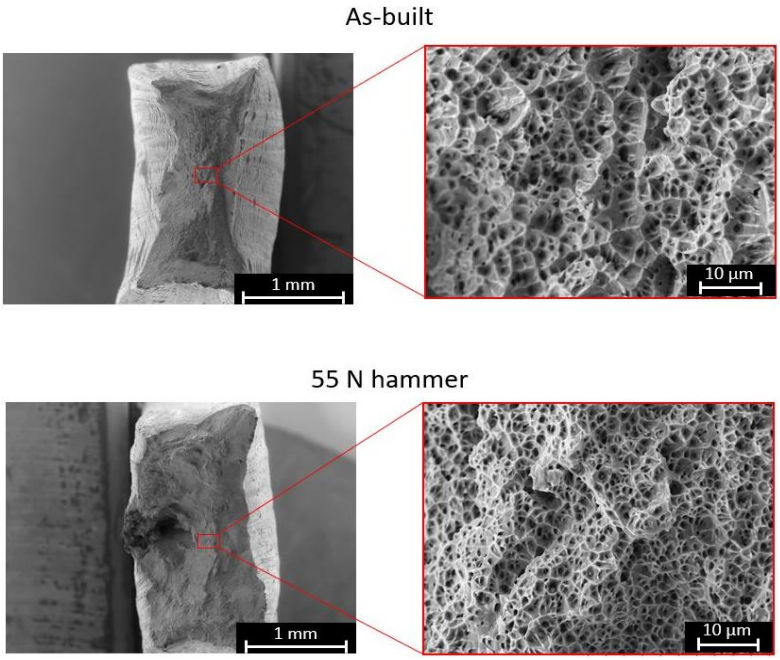

Figure 5.11 - Fracture surface from uniaxial tensile test specimen for the as-built and 55 N hammer

Electrical conductivity measurements

Figure 5.12 depicts the electrical conductivity profiles along the height of the parts, showing that the finer microstructure of hot forged sample does not significantly affect the electrical conductivity of this alloy.

Moreover, it is possible to observe a pattern in the electrical conductivity of the deposited material, where local maximums are recurrently found on the layers interface. This pattern is due to the variation of the microstructure within a layer where an increase in grain size is observed between the lower zone and the upper zone. Additionally, this pattern is more pronounced in the as-built sample, which means that forging allows for greater homogenization of the microstructure of each layer.

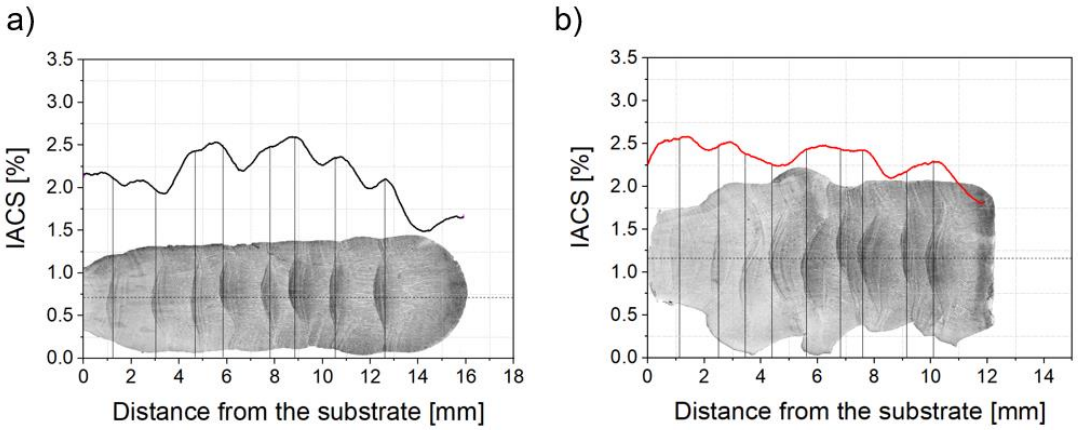

Figure 5.12 - Electrical conductivity profiles of the 316LSi sample a) as-built and b) with hot forging

5.3.2 Mild steel - ER70S-6

A regular stable deposition of the material was observed with a residual amount of spatter generated. The deformation promoted by the hot forging was constant and homogeneous throughout each layer achieving an equivalent true strain of 0.22 calculated with equation 4.11, when considering an average layer height before and after forging of 1.43 and 1.21 mm, respectively.

The last layer had a maximum depth of 0.9 mm due to forging without remelting (Figure 5.13).

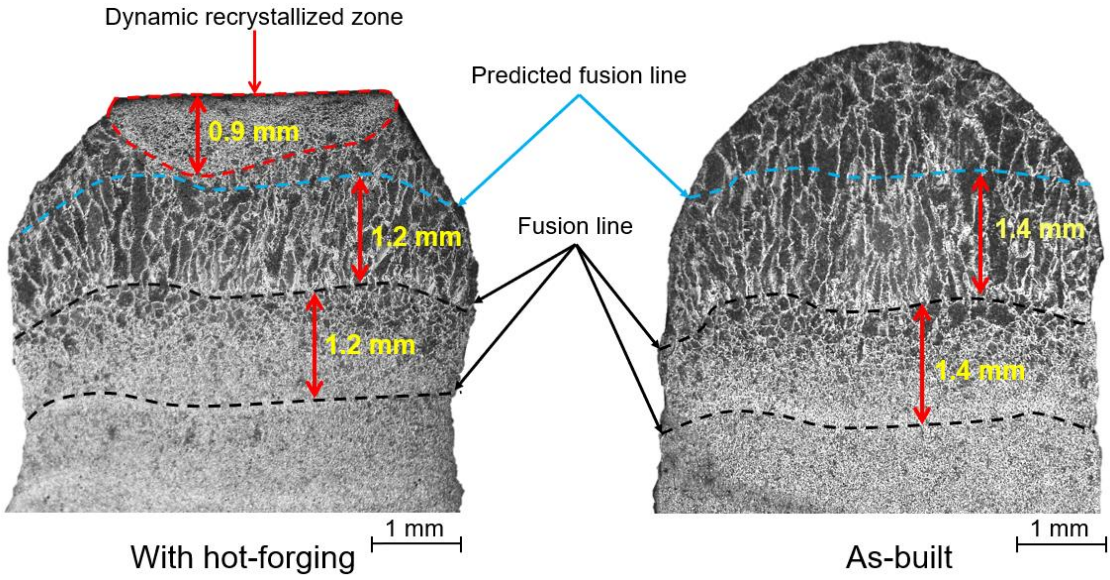

Figure 5.13 - Macrography of the top layers of mild steel samples as-built and with hot forging

The solidification structure is similar in both samples, apart from the recrystallization effect in hot forged sample with grain refinement.

During cooling, prior austenite grains transform according to the phase diagram into ferrite and perlite. Primary ferrite form at the previous austenitic grain boundaries with a polygonal morphology (allotriomorphic ferrite) and the remaining austenite transform into perlite or a mixture of perlite and bainite. Widmansttaten ferrite is observed developing from the grain boundaries into de grains suggesting the cooling rate is high.

Analysing the second last layer, it is also verified that the size of the prior austenite grains are similar in both samples, which indicates that the deformation induced in the sample with hot forging is insufficient to increase the number of nucleation sites. Figure 5.14 shows a micrograph of the heat affected zone.

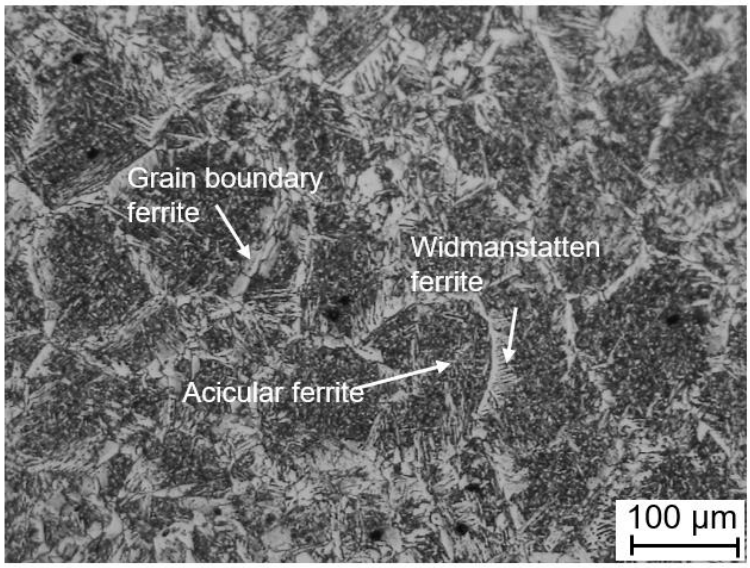

Figure 5.14 - Micrograph of the heat affected zone of the second last layer of the sample with hot forging

The layers below (Figure 5.15) have similar microstructures in both samples constituted by polygonal ferrite with perlite in the grain boundaries [145]. As-built samples had an average grain size of 11.8 ± 1.0 µm, and the hot forged ones of 11.0 ± 0.8 µm.

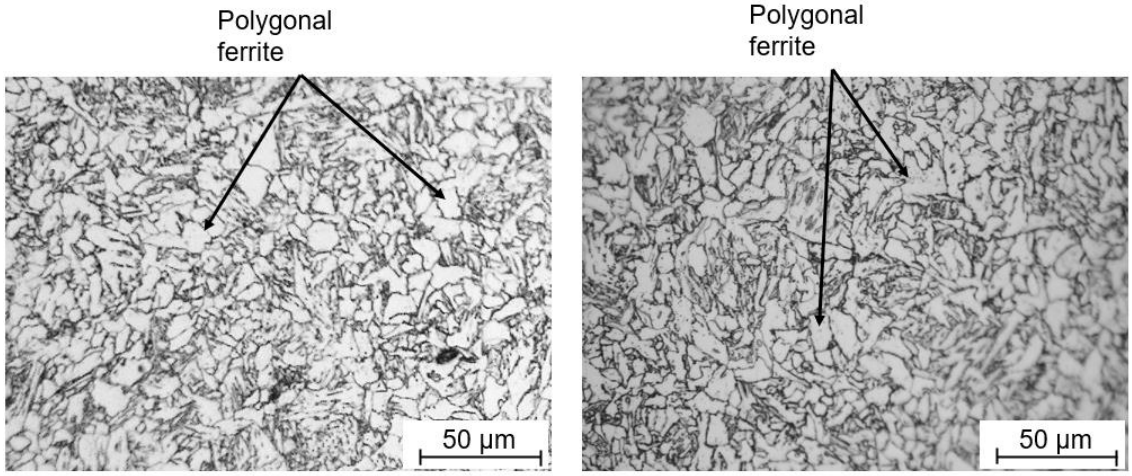

Figure 5.15 - Micrograph of the 7th layer of the samples produced a) with hot forging and b) as-built

The hardness profile of both samples is depicted Figure 5.16. The results showed a hardness average value for the as-built sample of 198 HV, and 206 HV in the sample undergoing forging.

Even though hardness is similar in both processing conditions, there is a slight increase in the sample with forging. Valleys are due to overlap of melted layers with full recovery of previous hardening effect and grain growth.

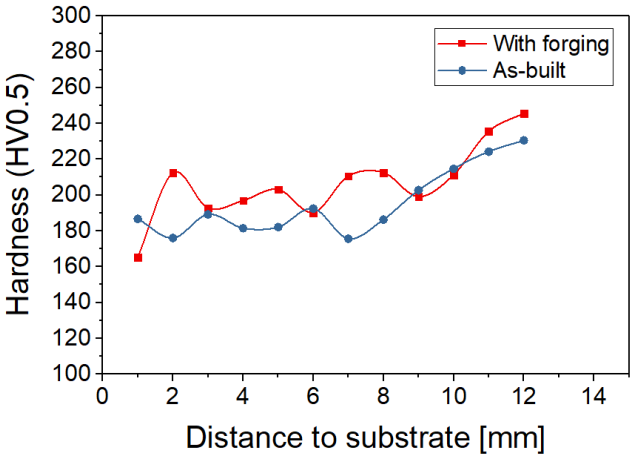

Figure 5.16 - Microhardness profiles of the as-built (blue) and forged (red) samples of mild steel

Figure 5.17 shows the results of the electrical conductivity measurements for the samples manufactured with the mild steel. There are no noticeable differences in electrical conductivity between both samples, despite the differences discussed above.

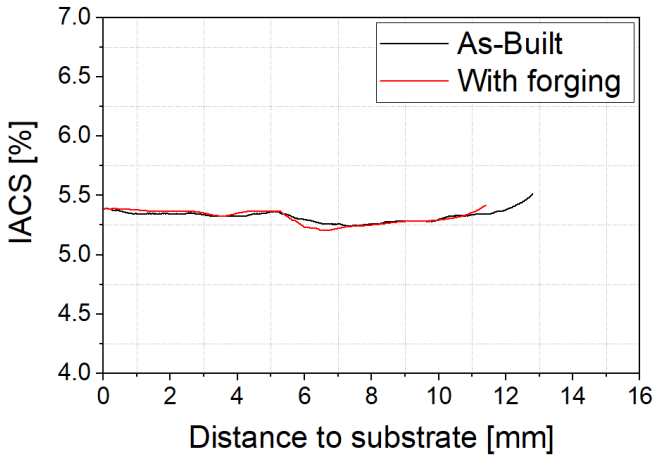

Figure 5.17 - Electrical conductivity of the mild steel samples

5.3.3 Stainless steel - ER410 NiMo

Arc welding of martensitic stainless steels is usually difficult due to cracking mechanisms, especially cold cracking [146]. However, in DED-arc these are not present because of two major reasons: the part is free, thus residual stresses are lower than in a confined weld bead and hydrogen content from decomposition of oils and dirt is also very low or non existent. So, after the optimization of parameters a stable material deposition was observed in both samples.

Regarding the material microstructure, there is also the possibility of delta ferrite formation during welding, which is detrimental to the toughness behaviour of martensitic steels and to other mechanical properties such as creep and ductility [147,148].

The formation of σ phase is another shortcoming that can be prevented reducing the heat input to increase the cooling rate [149]. Figure 5.18 shows the cross sections of the produced samples.

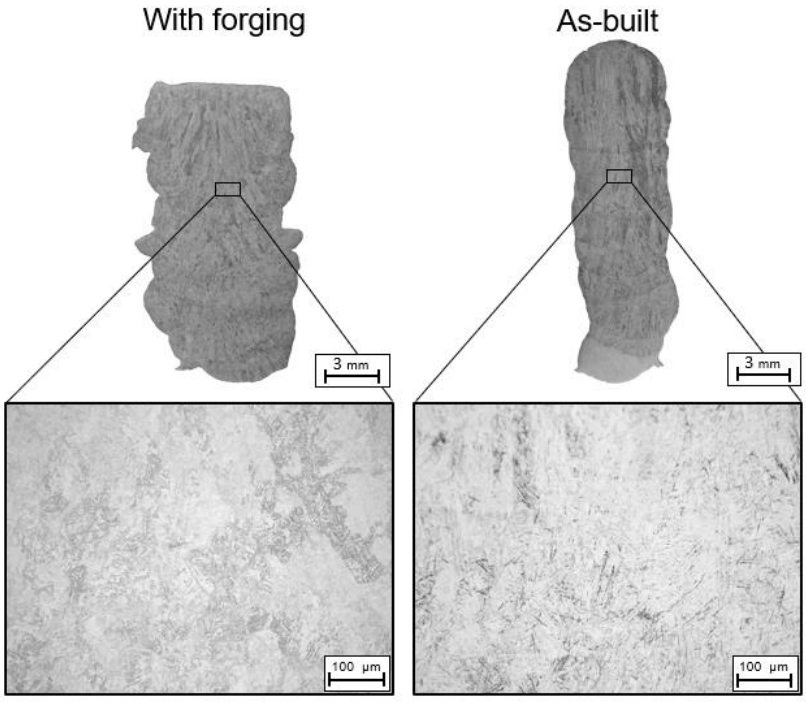

Figure 5.18 - Macrography and micrographs of the stainless steel 410 samples

In this case the as-built sample is thin, and in both samples a homogeneous martensitic microstructure was observed, with an average grain size of 35.9 ± 8.3 µm in the as-built sample, and of 36.4 ± 6.0 µm in the forged one.

Another major observation is the absence of a refined microstructure between deposited layers due to dynamic recrystallization, though the equivalent strain of 0.42, considering an average layer height before and after forging of 1.735 and 1.25 mm, respectively.

The hot workability of a material is associated with the generation of dislocations and deformation defects while dynamic recovery and dynamic recrystallization inhibit the accumulation of these defects. In most martensitic stainless steels, hot working is performed in the stability region of austenitic phase, where dynamic recrystallization is dominant over dynamic recovery [137,138,150]. According to Manohar et al. [151], the mechanism of dynamic recovery is mostly influenced by the phase stacking fault energy (SFE). In phases with high SFE, such as ferrite, dynamic recovery occurs easily and is predominant while in low SFE phases such as austenite, recovery is slow.

As it can be seen from the Fe-Cr equilibrium phase diagram with 0.05 % of Carbon shown in Figure 5.19, and considering that the used material has 13.5 % of Cr, it is observed that during cooling it is not expected the material to be only in austenite phase, always having some ferrite phase.

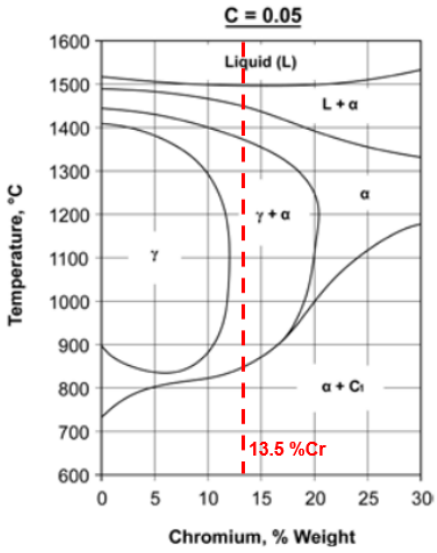

Figure 5.19 - Fe-Cr phase diagram (adapted from [137])

Other authors have reported that the safe region for hot deformation in 410 stainless steel is in the temperature range 1000 – 1125 °C with a strain rate between 0.001-10 s^{-1}, and that the grain size remains almost unchangeable at strain rates higher than the steady state flow [134].

Hardness was almost the same in both samples, as depicted in Figure 5.20, 355 HV for the hot forged sample and 350 HV for the as-built one, suggesting the presence of martensite.

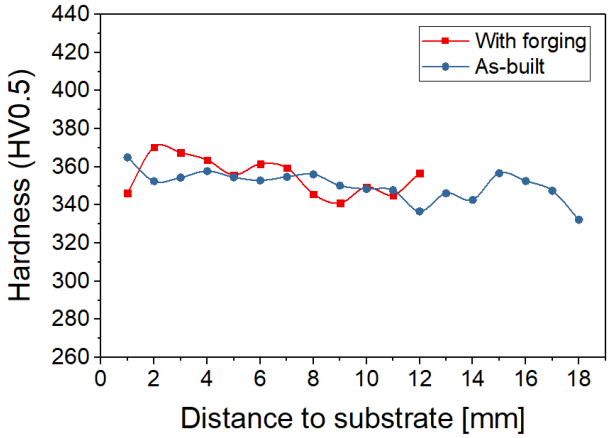

Figure 5.20 - Microhardness profiles of the as-built (blue) and forged (red) samples of stainless steel 410

The results of the measurement of electrical conductivity shown in Figure 5.21 confirm the observations performed on the microstructure of the material, in which a great homogeneity was observed throughout the entire sample, and no differences promoted by forging were noticed. Although it is possible to observe a slight tendency for the forged sample to have a higher conductivity than the as-built sample, the absolute variation in conductivity is less than 0.1 %IACS, which is within the error of the measurement.

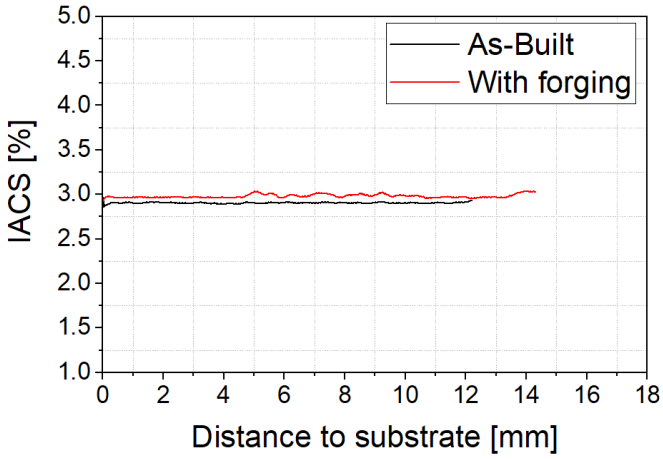

Figure 5.21 - Electrical conductivity of the stainless steel 410 samples

Thus, it can be concluded that for this particular material, hot working where dynamic recrystallization can occur has a very narrow range and that, under the conditions used, dynamic recovery is the dominant softening mechanism. So, the application of hot forging on DED-arc of this material with the aim to improve its microstructural and mechanical properties is not viable.

5.3.4 Aluminium 1070 alloy – ER1070

The deposition of the 1070 aluminium alloy is usually associated with 3 main issues: the excessive grain growth, that is not recovered since there are no solid state transformations in this material hindering the mechanical properties [152]; the formation of large amounts of porosity that is related to hydrogen and oxygen sources, and therefore requires good gas shielding and cleaning of wire and substrate surfaces; and also the high deformations caused by the generation of residual stresses that occur due to the high coefficient of thermal expansion of the material [153]. Among these, the hot forging during DED-arc may be particularly beneficial in preventing the excessive grain growth and reducing the porosity.

In the produced samples, the deposition has remained stable with a continuous material transfer over the various layers. However, the formation of porosities was not avoided

When producing the sample with forging, it was observed a constant deformation along the length of each layer, resulting in a flat top surface. An equivalent true strain of 0.17 was calculated for the hot forged sample, considering an average layer height before and after forging of 1.72 and 1.51 mm, respectively. The low value of true strain indicates that the material is being forged at low temperatures, and that despite the smaller diameter of the hammer tip used, where the forging occurs at 10 mm from the electric arc, the rapid cooling of the material due to the high thermal conductivity, originates that forging occurs at a low temperature.

However, the effect of the forging was clearly seen in several pores, where a change in pores morphology was observed, transforming the sphere-shaped pores into ellipsoidal ones. Additionally, in the centre of the sample with forging, a zone where the density and size of the porosity is considerably lower than that observed in the as-built sample (Figure 5.22). This is due to the way the stresses develop inside the part during forging. As explained in the previous section, the material located in the centre of the sample is only subjected to compressive forces, which explains the greater efficiency of the hammer in reducing porosity in the centre of the sample.

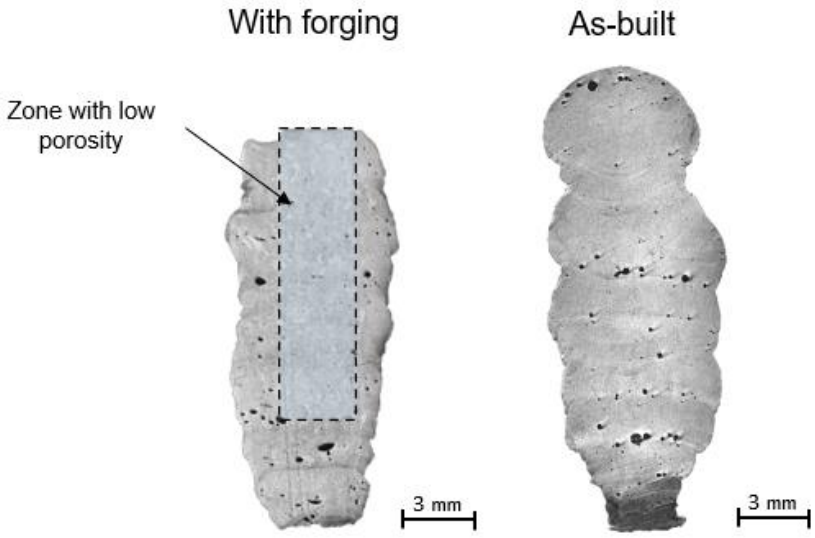

Figure 5.22 - Macrograph of samples in aluminium 1070 alloy

The aluminium 1070 alloy has no transformations in solid state, thus, it is prone to form large columnar grains during solidification, depending on the heat input and thus, on the time for cooling that determines the morphology and microstructure in the solid state. Since epitaxial grain growth requires low undercooling to occur, columnar grains grow epitaxially from the previous layer grains in a directional solidification along with the heat flow direction. In DED-arc the heat flows mostly downwards in the vertical direction, and the nucleation on the columnar grains of the previous layer, allows a continuous columnar grain growth throughout multiple layers [154].

This directional solidification structure with elongated grains oriented along the building direction causes anisotropy of the mechanical properties in DED-arc parts. With the vertical direction exhibiting lower yield (YS) and ultimate tensile strengths (UTS) than the horizontal direction. The anisotropy also affects the ductility which is lower in the horizontal direction [56,57,155].

To avoid epitaxial and directional grain growth in DED-arc of aluminium alloys, several researchers have approached different methodologies such as, chemical inoculation [156], the use of switchback welding technique [154] or cold forging with hammer or high-pressure inter-pass rolling [76].

Regarding the high pressure inter pass rolling on aluminium alloys, it was found that the coarse oriented grain structures can be refined to grain sizes of less than 10 μm when rolled with a 45 kN load. According to Gu et al. [76] the microstructure refinement is due to the occurrence of recrystallization during the DED-arc re-heating process.

The microstructure observed in both manufactured samples differ in morphology, from a columnar grain in the as-built sample to an equiaxed grain in the hot forged sample, particularly in the region of the fusion line between layers as it can be observed in Figure

5.23. The measurements of the grain size showed an average width of the epitaxial grain of 308.2 ± 95.3 µm, while the equiaxed grain had an average size of 234.5 ± 30.8 µm.

Grain sizes similar to those of high pressure inter-pass rolling have not been achieved, since the amount of dislocations introduced by cold rolling is much higher than those introduced during hot forging, but it was concluded that hot forging induces sufficient deformation to promote recrystallization and nucleation of equiaxial grains.

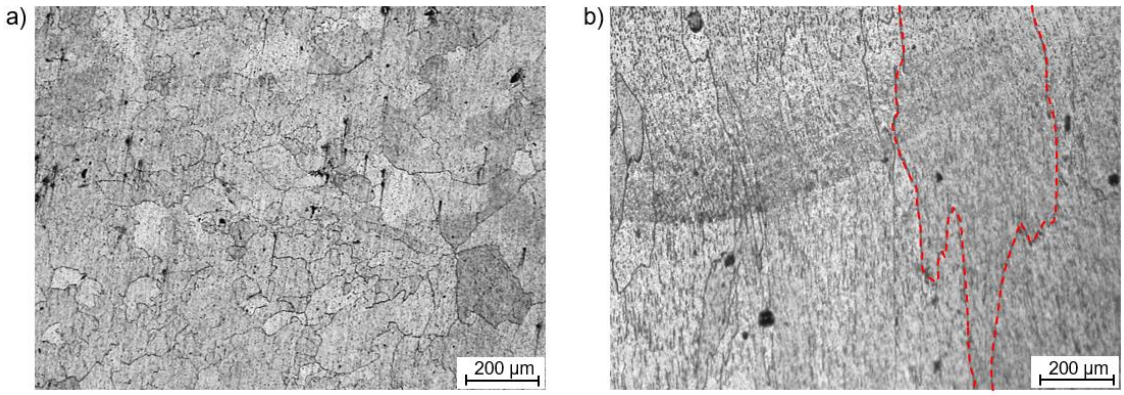

Figure 5.23 - Micrographs of the aluminium 1070 alloy samples a) with hot forging and b) as-built

Despite the differences observed in grain size and morphology, these were not seen in the material hardness where in both samples a Vickers hardness of approximately 23 HV was measured (Figure 5.24).

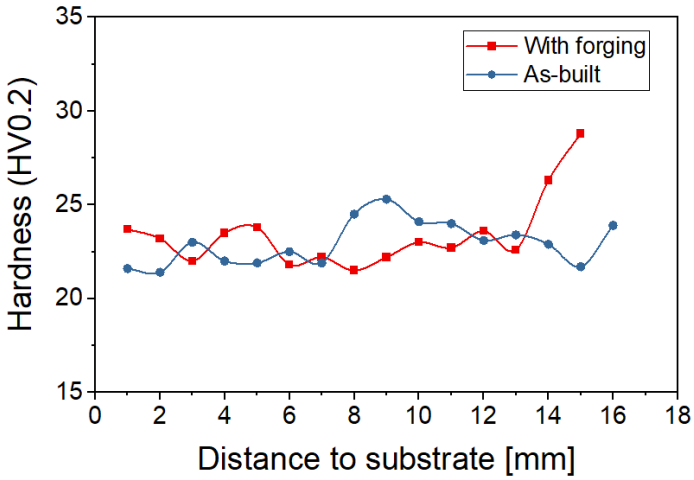

Figure 5.24 - Microhardness profiles of the as-built (blue) and forged (red) samples of aluminium 1070

The decrease in grain size caused by plastic deformation during hot forging promotes a reduction in the electrical conductivity of the material, eventually due to the content of dislocations and other barriers to electron diffusion into the material. As can be seen in Figure 5.25, the electrical conductivity of the forged sample is consistently lower than the

conductivity of the as-built sample by about 2 %IACS, with the exception of the centre of the sample where was detected a variation caused by the large porosities present in the as-built sample.

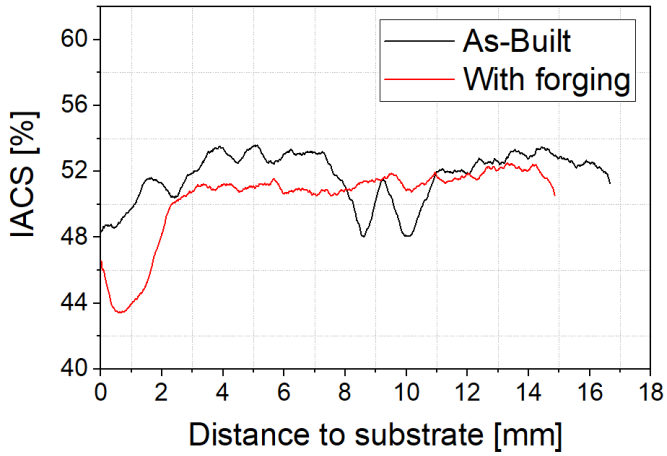

Figure 5.25 - Electrical conductivity of the aluminium 1070 samples

5.3.5 Inconel 625 - ER NiCrMo-3

In the deposition of Inconel 625 a constant and stable deposition of material was achieved throughout the different layers and no defects were detected.

Hot forging induced deformation was also constant and homogeneous throughout the multiple layers. The average layer height of the samples with hot forging was of 1.14 mm and without was of 1.36 mm, therefore the calculated equivalent true strain was 0.22, according to equation 4.11. Figure 5.26 shows the cross section of the produced samples.

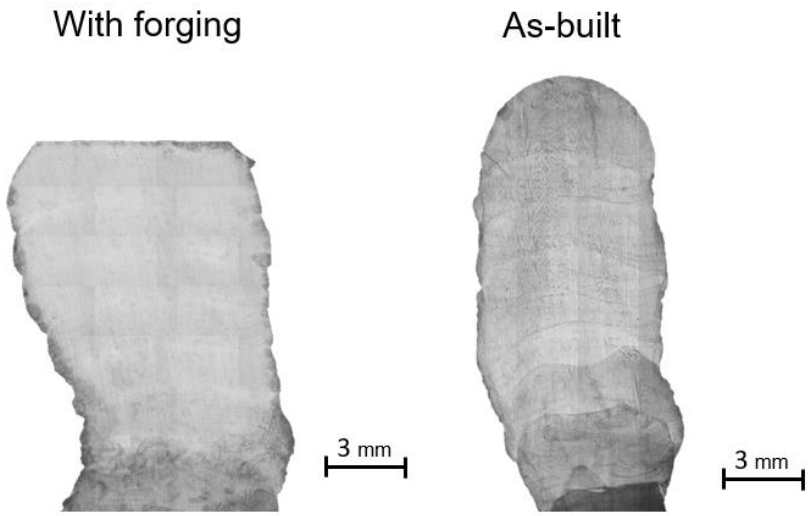

Figure 5.26 - Macrographs of the Inconel 625 samples

In the last layer of the sample produced with hot forging it was observed a region where dynamic recrystallization occurred due to the hot forging, with a maximum depth of about 0.67 mm (Figure 5.27).

The as built sample also shows a different microstructure in the upper zone of the last layer. However, this microstructure continues to be columnar dendritic as in the overall sample and this differentiation results from the change in the solidification conditions, as it still presents large grains.

As shown in Figure 5.27 c) and d), the microstructure of both samples is constituted by elongated grains with columnar dendrites typically observed in DED-arc [157]. On the hot forged sample, a dendritic structure with a primary dendrite arm spacing (PDAS) of 8.7 ± 1.8 µm was observed while the as-built sample microstructure revealed a dendritic structure with a primary dendrite spacing of 14.7 ± 1.0 µm.

Similar to what was observed in the microstructure of the stainless steel 316LSi, these structural changes in the primary dendrite sizes are related to the increase of the nucleation sites created in the dynamic recrystallized zone induced by hot forging, which increases the competitive grain growth, thus forming a refined columnar dendritic structure [157].

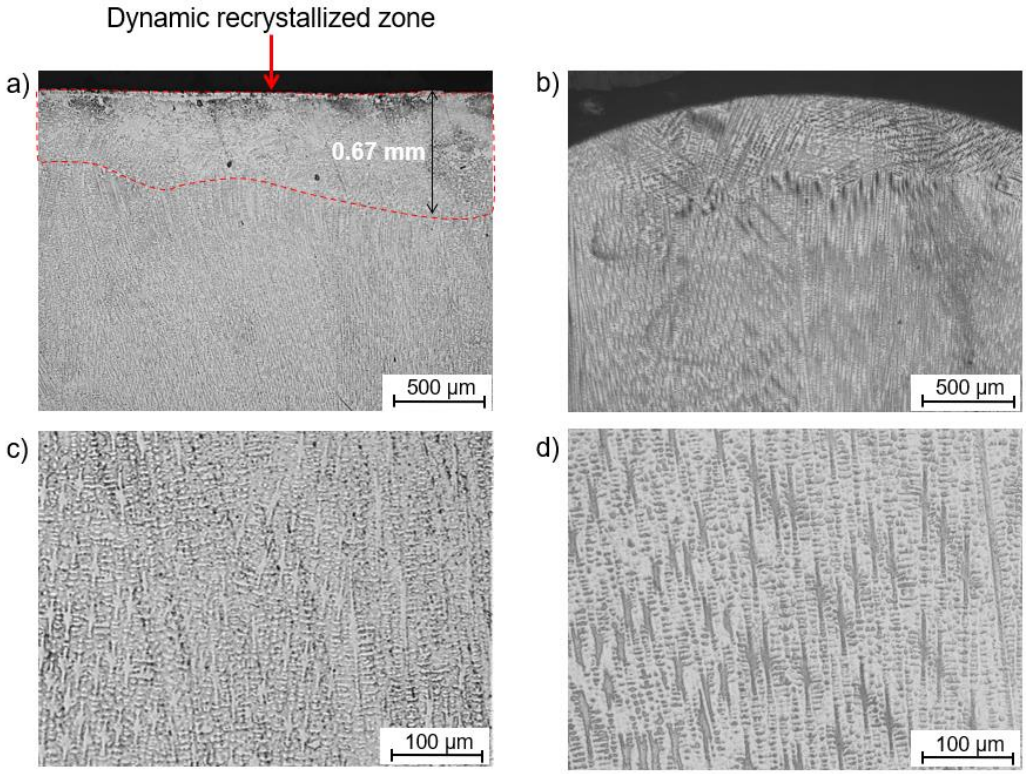

Figure 5.27 - Micrographs of the Inconel 625 samples produced by hot forging DED-arc in: a) last layer and c) 5th layer, and of the as-built samples in the b) last layer and d) 5th layer

Identification of inter-layer regions where dynamic recrystallization may have occurred was not possible through optical microscopy, so Electron Backscatter Diffraction (EBSD)

analysis was carried out and the results are shown in Figure 5.28. With the EBSD data the Grain Orientation Spread (GOS) was computed with the open source *MTEX Tolbox* developed for the *Matlab* software. The GOS is a parameter that expresses the average of the misorientation angles to the grain mean orientation, and it is used to average this misorientation angle for each grain separately. Thus, higher GOS values are indicators of grains with more misorientations than those with lower GOS values. Since, recrystallized grains normally contain lower dislocation density and consequently lower GOS than the deformed grains [158], this parameter allows to distinguish the grains affected by hot forging from the non-affected ones.

It was observed that in the sample with forging, large columnar grains present higher GOS values than those grains in the as-built sample. This is an indicator that the deformation caused by forging produces defects as dislocations. During deposition of the following layer, dislocations move, rearrange in a recrystallized structure increasing the nucleation sites for the new solidification structure.

In the hot forged sample, small grains were observed near the fusion line, with a very low internal deformation rate expressed by the GOS parameter, as shown in Figure 5.28 a) and c).

It is also noticed that there is a crystallographic continuity between successive layers in both samples, *e.g*. epitaxial grain growth, which shows that hot forging was not sufficient to cause enough dynamic recrystallization to prevent the epitaxial grain growth between layers.

Moreover, the difference between the grains aspect ratio in the hot forged and in the as-built sample due to the increase of the nucleation sites is evident, while in the hot forged sample the grains are considerably finer.

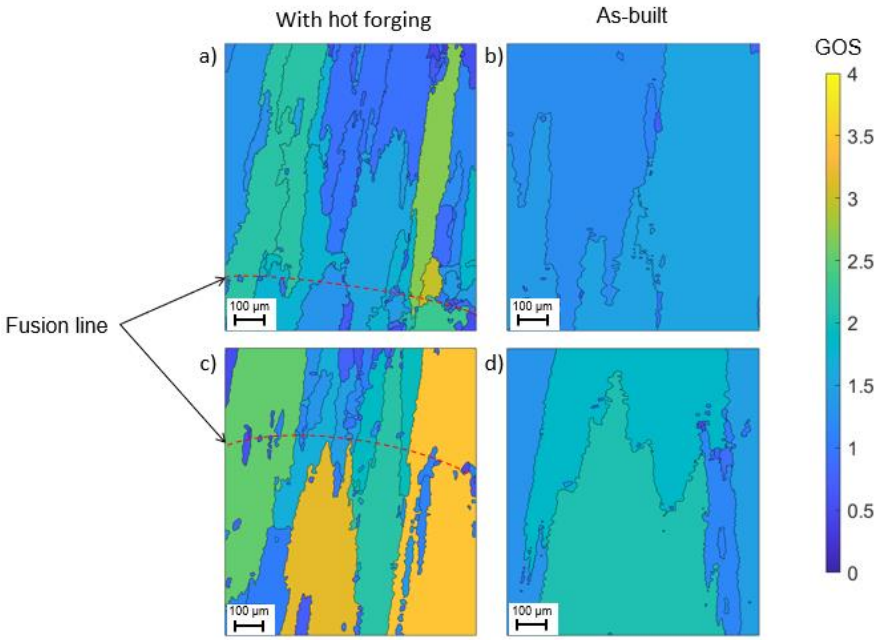

Figure 5.28 - EBSD maps showing the GOS distribution of the Inconel 625 samples produced with hot forging and as-built, in a) and b) top of the sample and c) and d) in the 5th Layer

As it can be seen in Figure 5.29, despite the visible difference in the microstructure, there was no influence of the forging on the hardness of the material, except for the last layer where a recrystallized microstructure was observed.

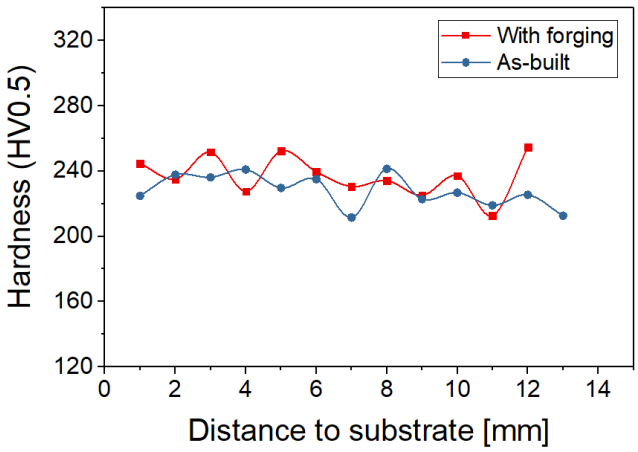

Figure 5.29 - Microhardness profiles of the as-built (blue) and forged (red) samples of Inconel 625

Measurements of electrical conductivity (Figure 5.30) showed a high level of microstructural homogeneity in both samples throughout the height, as well as within each layer, and between the hot forged and as-built samples no significant variations were observed, so hot forging does not affect the material electrical conductivity.

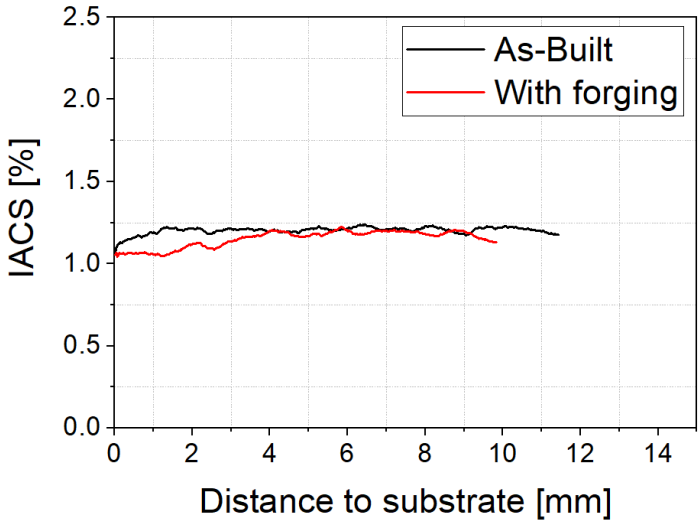

Figure 5.30 - Electrical conductivity of the Inconel 625 samples

5.3.6 Monel 400 - ER NiCu7

The deposition of the material with the DED-arc was performed, however, a significant amount of spatter was formed during drop detachment. In fact, welding of Monel alloys, using MIG, the relatively low fluidity of the liquid makes drop detachment unstable, and therefore the spatter formation occurs. When the arc is interrupted and re-established, it strikes in a very intense way, causing the drop to deviate, instead of joining the molten pool.

Regarding the hot forged sample, deformation was achieved throughout all layers, however there was a slight irregularity of this deformation, promoting a flat but uneven upper surface. It was also noticed that the amount of spatter increased in the sample with hot forging when compared to the as-built one. This fact is due to the torch vibration caused by the hammer, that further promotes the irregular detachment of the drops causing it to deviate from the molten pool. Since the molten drops randomly deviate from the molten pool, its size is changing constantly, and the temperature of the material being forged also varies. Thus, heterogeneities in the deformation throughout the layer deposition occur (Figure 5.31). Additionally, this vibration caused by forging can also contribute to the refinement of the microstructure, as it is known from welding technology. The vibration of the molten pool increases the nucleation sites and consequently a finer structure is formed due to the competitive grain growth [159,160].

Moreover, by equation 4.11, the calculated equivalent true strain on the hot forged sample was of 0.38, considering an average layer height of 1.65 mm before forging and of 1.23 mm after forging.

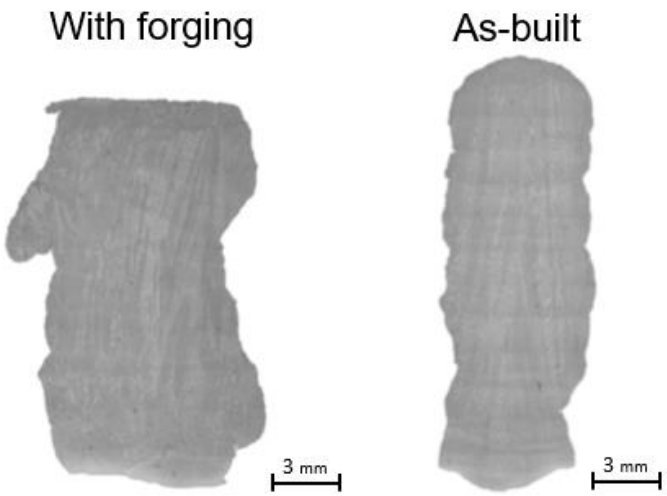

Figure 5.31 – Macrographs of the cross sections of the Monel 400 samples

The microstructure of the samples revealed the potential regarding the application of hot forging, since the last layer shows a region of dynamic recrystallization with a depth of about 1.2 mm, as shown in Figure 5.32. Moreover, a region with a recrystallized microstructure was also identified between layers.

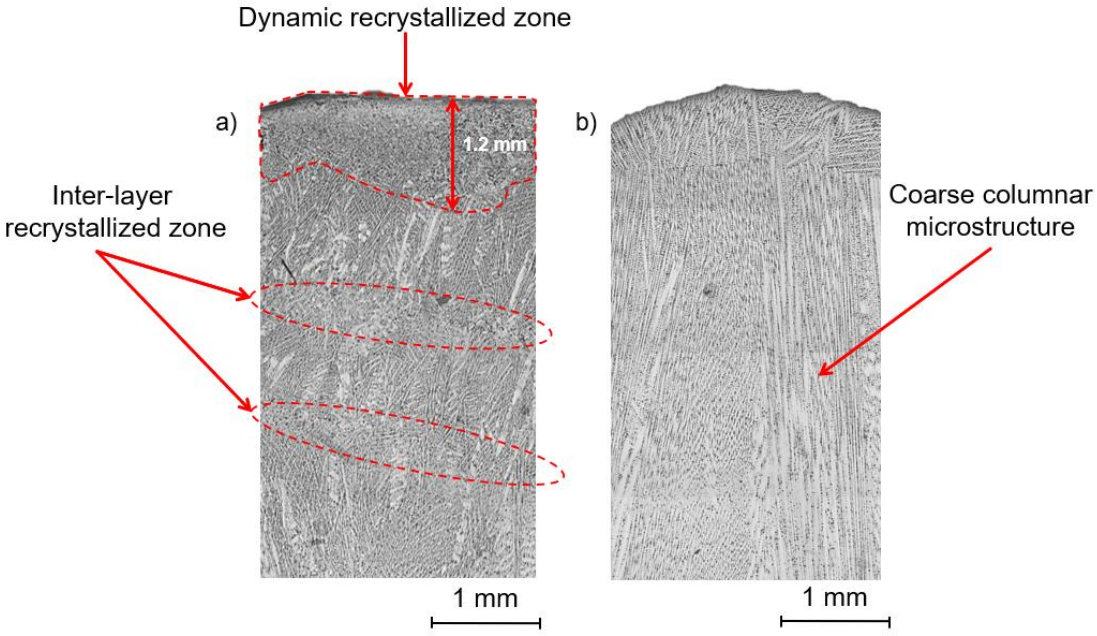

Figure 5.32 – Micrographics of the top in a) hot forged and b) as-built Monel 400 samples

Since the average height of a layer on the hot forged samples is about 1.2 mm, practically all the deposited material on that layer was dynamically recrystallized. During the deposition of the subsequent layer, part of the dynamic recrystallized zone is not remelted and remains on the final microstructure of the sample. This recrystallized microstructure between layers, prevents the growth of large columnar grains between

successive layers, inhibiting the epitaxial grain growth that was observed in the as-built sample, as shown in Figure 5.33.

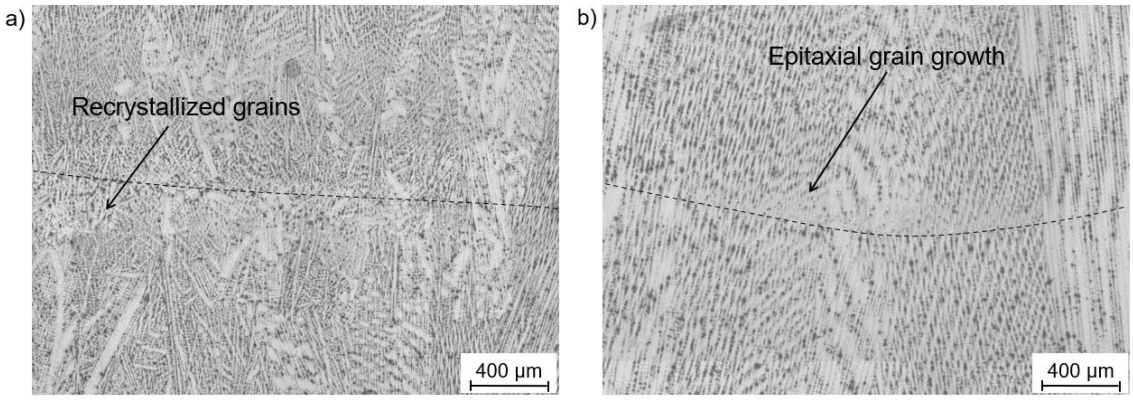

Figure 5.33 - Micrographs of the fusion zone of the Monel 400 sample a) with hot forging and b) as-built

The hardness profile acquired in a line in the centre of the sample (Figure 5.34) showed no difference throughout the height of both samples, except in the last layer, where it is possible to observe an increase in hardness due to the presence of a recrystallized microstructure.

Hardness measurements were performed, selectively, in the hot forged sample in the recrystallized microstructure between layers where a consistent value of 143 HV was measured, while in the remaining area of the layer the hardness was on average of 131 HV.

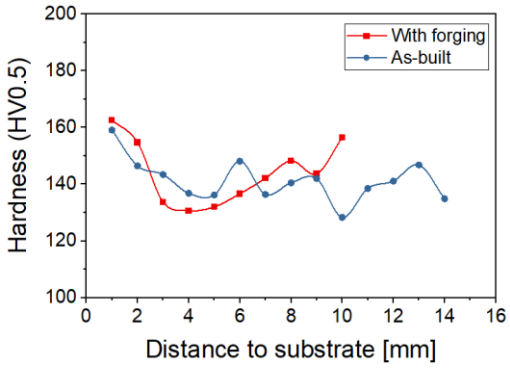

Figure 5.34 - Microhardness profile of the as-built (blue) and forged (red) samples of Monel 400

The electrical conductivity measurement results show consistently a higher electrical conductivity value for the as-built sample, the absolute variation in conductivity is less than 0.2 %IACS (Figure 5.35). Although the hot forged sample has a more refined microstructure than the as-built, this difference in grain size does not greatly affect the material conductivity. Moreover, it is possible to observe that the recrystallization zones do not promote a macroscopic heterogeneity on the material electrical conductivity.

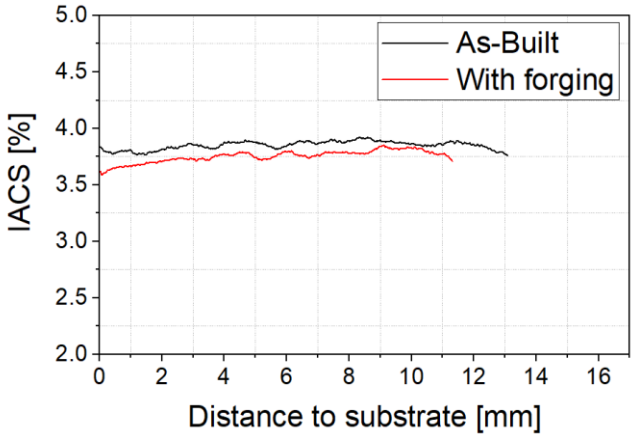

Figure 5.35 - Electrical conductivity of the Monel 400 samples

5.3.7 Copper aluminium alloy - ERCuAl-A2

The Cu-Al alloy was studied due to its potential applications in conductive components, where a good anti-corrosion, anti-wearing and electrical conductivity properties are required, such as in the production of batteries or embedded electrical circuits. Despite these, additive manufacturing of this alloy was not yet reported.

Although the production of copper-aluminium alloys parts by DED-arc is not common in the bibliography, the deposition had a stable material transfer throughout the successive layers and spatter formation was not observed. No internal defects were seen on the parts produced. When hot forging was performed, the deformation was constant throughout each layer, resulting in a flat top surface. An equivalent true strain of 0.17 was calculated for the hot forged sample, considering an average layer height before and after forging of 1.45 and 1.27 mm, respectively.

This Cu-Al alloy mainly consists of copper with 8.5 wt. % of aluminium, however, it also contains a small addition of iron. To analyse the microstructure of the samples, it is important to note that the binary diagram of the alloy is not affected by iron additions of this amount, since iron appears as fine precipitates homogeneously distributed throughout the structure. Thus, the iron acts only as a grain refiner during solidification improving the mechanical properties of the Cu-Al alloy [161].

Looking at the macrographs (Figure 5.36), it was observed that in the as-built sample, the epitaxial growth of prior β grains is favoured, forming large columnar grains that extend over almost the entire height of the sample. The presence of this type of microstructure is associated with anisotropy in mechanical properties [162]. Moreover, it was also observed that hot forging partially inhibits the epitaxial growth of prior β grains.

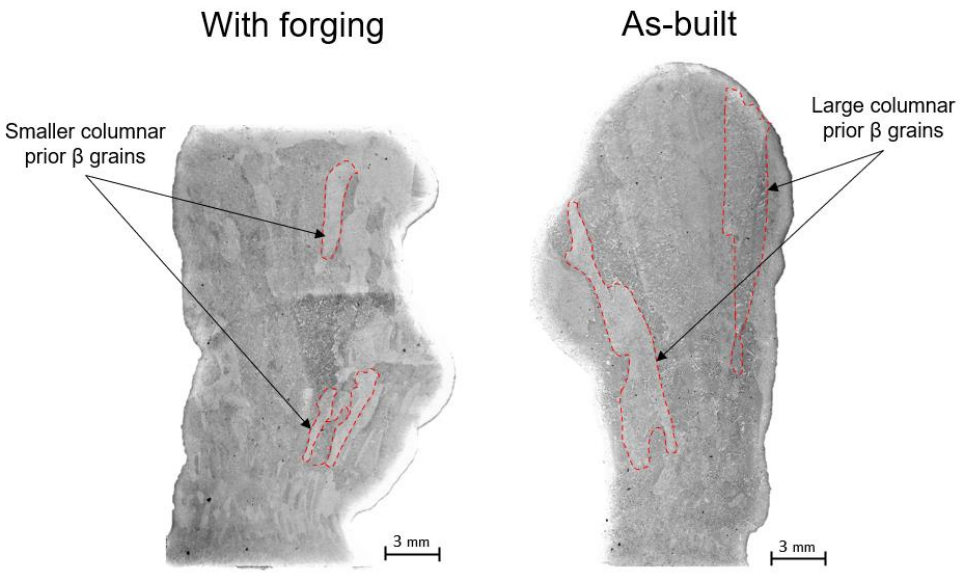

Figure 5.36 – Micrographs of the Cu-Al alloy samples

The microstructure observed in both samples was characterized by a cellular-dendritic morphology, with columnar α phase (white zone) with β phase in the spaces (dark zone) [163], as shown in Figure 5.37.

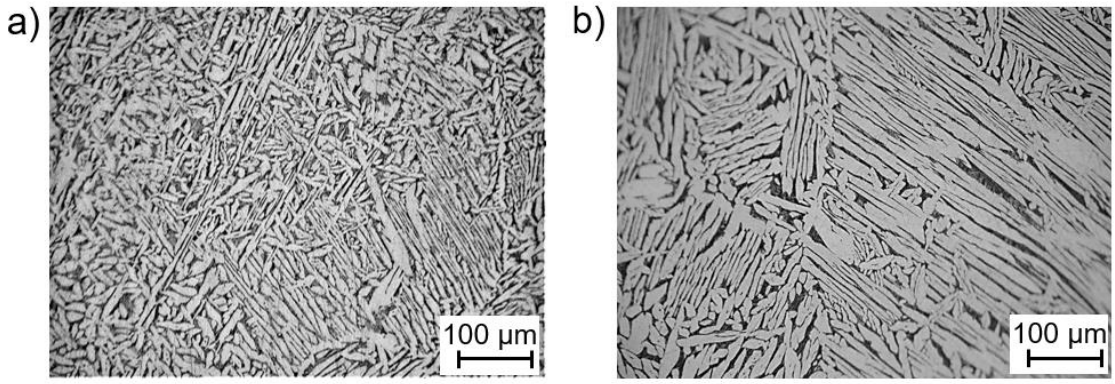

Figure 5.37 - Micrographs of the fusion zone of the Cu-Al alloy sample a) with hot forging and b) as-built

The average grain width measured was of 23.2 ± 5.2 µm and 11.4 ± 2.3 µm for the as-built and the forged samples, respectively. Thus, by inhibiting the epitaxial prior β grain growth the hot forging also reduces the consequent microstructure that is formed during cooling. Another observed feature is that the forged sample has a higher β phase fraction, which can be seen in the micrographs but also in the diffractograms depicted in Figure 5.38.

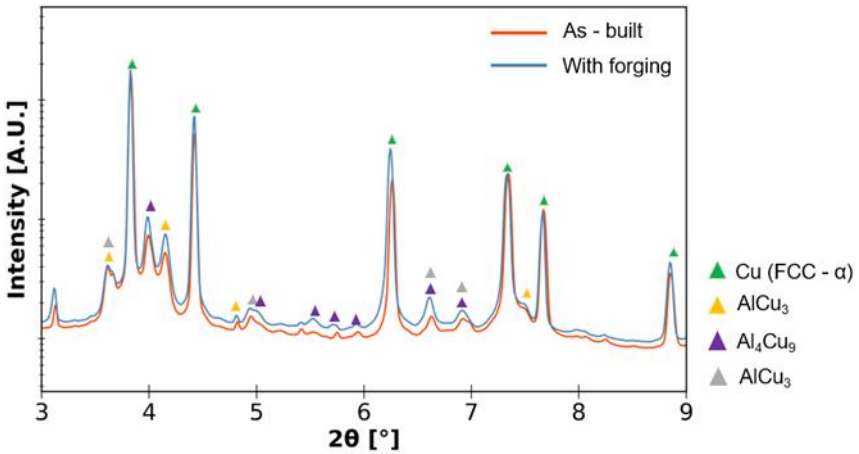

Figure 5.38 - Diffractogram of as-built and hot forged sample

X-ray synchrotron radiation also shows that the hot forging operation has no effect on the identified phases. However, from the 2D Debbye-Sherrer diffractograms it can be observed that the as-built part has a coarser and textured microstructure, while the hot forged one has a homogeneous more isotropic fine- grained microstructure with almost no texture (Figure 5.39).

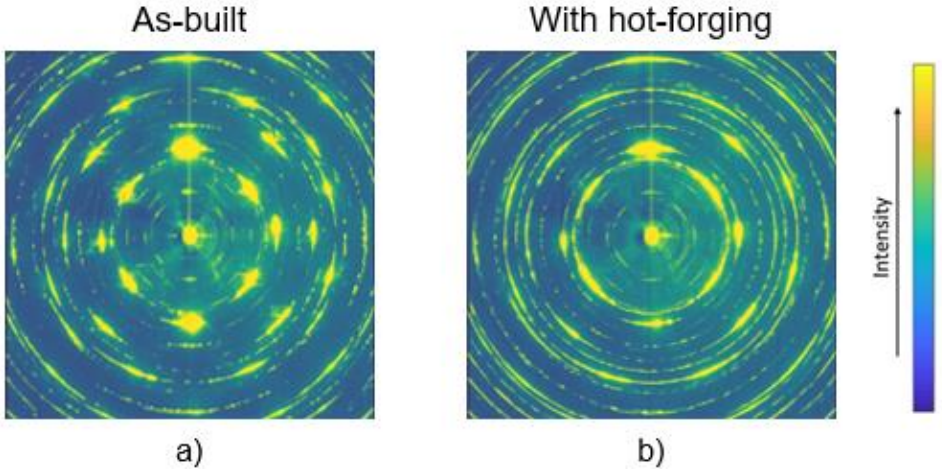

Figure 5.39 - 2D Debbye-Scherrer patters of samples: as-built (a) and hot forged (b).

The hardness values were 145 ± 5.87 HV and 155 ± 8.85 HV for the as-built and the forged samples respectively, as shown in Figure 5.40, which agrees with the microscopic features described above. The increase of β phase fraction may explain the slight increase in hardness despite the significant reduction of grain size. Additionally, the measurements on the last layer of the sample with forging presented a much higher hardness value (+25 HV) than those observed in the as-built sample. This occurs because unlike on the other layers the last one is not subjected to the multiple reheating cycles, caused by the subsequent depositions, and therefore the refined microstructure induced during the hot forging are still present in the material.

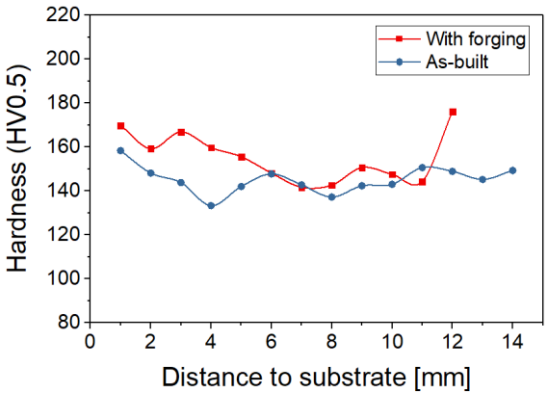

Figure 5.40 - Microhardness profiles of the as-built (blue) and hot forged (red) samples

Since copper aluminium alloys are used in electromagnetic applications, the electrical conductivity was measured to assess, whether the effect of hot forging reduced this property. Figure 5.41 depicts the electrical conductivity profiles along the height of the parts, and there is a negligeable difference, showing that the finer microstructure of hot forged sample does not significantly affect the electric conductivity of this alloy, which can be beneficial.

The fact that this alloy has an excellent electrical conductivity, prevents to have an identification of the grain refined zones in the manufactured parts, as observed in other alloys [164].

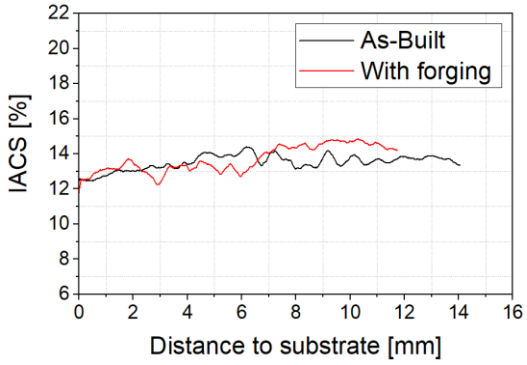

Figure 5.41 - Electrical conductivity of the Cu-Al alloy samples

Effect of the hot forging vibration on the microstructure

It is known from arc welding technology, that the vibration of the molten pool is a technique to refine the microstructure by increasing nucleation sites and consequently affecting the grain growth which may improve the mechanical properties of the weld metal [159,160]. Therefore, an additional test was performed to evaluate whether the vibration introduced by the hot forging alone is the cause of further changes in the material microstructure. For this, the diameter of the hammer was increased so that it hits the material at a temperature too low to deform it, thus producing vibration but

without deformation. The remaining process parameters were the same of the samples above.

The results showed that, in fact, part of the changes observed in the microstructure are also due to the vibrations caused by the hot forging, with the sample showing an average grain width of 18.2 ± 2.8 µm, which represents a reduction of grain size by about 21 % when compared to the as-built sample. Since these vibrations introduce a greater disturbance in the molten pool, it promotes the creation of nucleation sites, leading to a smaller grain size upon cooling. However, in this sample, continuous columnar grains were still present throughout almost the entire sample, similar to those observed in the as built samples in Figure 5.42. Although the vibration promotes a refinement of the microstructure, it does not prevent the epitaxial grain growth throughout multiple layers, thus the forging effect is dominant to prevent this grain growth contributing to reducing the microstructure anisotropy.

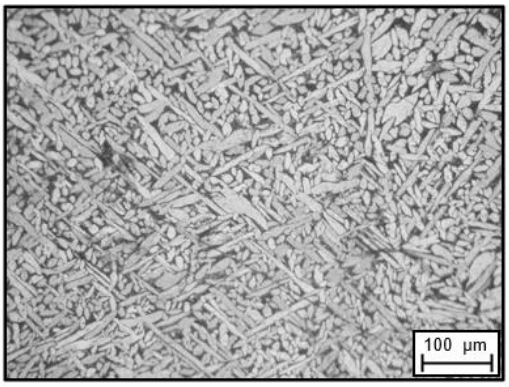

Figure 5.42 - Micrograph of the sample produced with the hot forging vibrations on Cu-Al alloy

Mechanical properties

The aim of the mechanical tests was to evaluate the mechanical properties anisotropy of the deposited material, thus compression tests were preferred over tensile, since with the production of reduced specimens it is possible to evaluate specific zones in different directions.

The results of the mechanical tests performed are in agreement with the above considerations on the microstructure. Representative compression stress-strain curves for each sample obtained at different orientations are depicted in Figure 5.43.

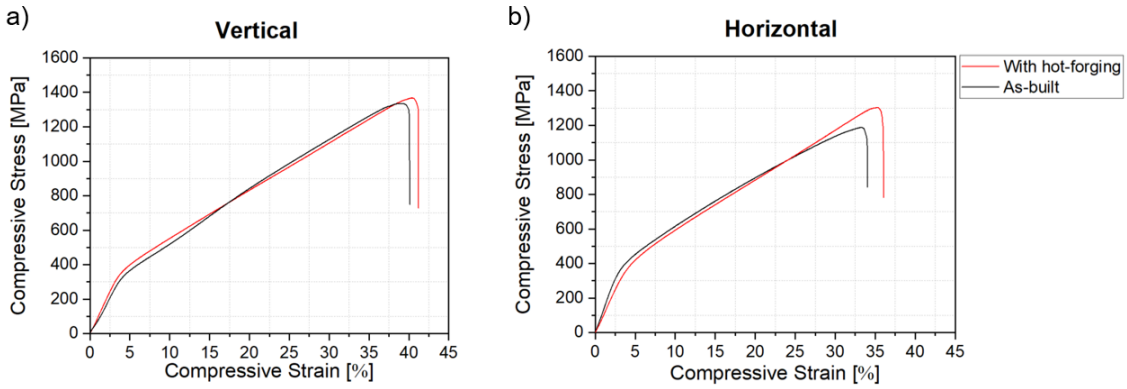

Figure 5.43 - Uniaxial compression stress-strain curves for the samples removed from horizontal a) and vertical b) directions of the as-built and hot forged samples

The summary of these compression tests is further detailed in Table 5.4. It can be observed that upon the use of hot forging during DED-arc of the Cu-Al alloy results in more isotropic mechanical properties. In particular, the yield strength of the hot forged samples is identical in the specimens obtained in the vertical and horizontal directions, while those obtained without hot forging presented a higher yield strength in the horizontal direction. The large and highly oriented grains in the samples manufactured without hot forging justify this variation. The compressive strength of the parts was also seen to show similar values in the vertical and horizontal hot forged DED-arc parts, while in the as-built sample a difference of more than 100 MPa was determined. These results further highlight the potential of hot forging DED-arc in contributing to a microstructure refinement resulting in more isotropic mechanical properties. Fracture always occurred at 45º with the applied force direction.

Table 5.4 - Summary of mechanical properties

Direction of sample removal		Yield strength [MPa]	Compressive strength [MPa]
Vertical	With hot forging	258 ± 33	1362 ± 64
	Without hot forging	245 ± 15	1334 ± 79
Horizontal	With hot forging	246 ± 13	1349 ± 42
	Without hot forging	292 ± 26	1216 ± 20

5.4 Summary of results

To summarize the results presented above, a comparison between the samples with and without forging is shown in Table 5.5, in which it is indicated whether there were, or not, differences in the results of microstructure, microhardness, and electrical conductivity tests for each of the studied materials.

On the stainless steel 316LSI and Cu-Al alloy the hot forging refines the solidification microstructure, thereby improving the mechanical strength and reducing the anisotropy.

In aluminium alloy 1070 and Monel 400 the achieved depth of dynamic recrystallization, due to the hot forging, was greater than the penetration of the following layer, which prevents the epitaxial grain growth between consecutive layers, thus reducing the microstructural anisotropy of the sample. Moreover, the effectiveness of hot forging in promoting dynamic recrystallization in mild steel and Inconel 625 materials was also verified.

The only material where there was no microstructural changes promoted by hot forging was the stainless steel 410, and this was due to the narrow temperature range and strain rate where hot forging is effective in this material.

Table 5.5 - Summary of the results in the different materials

Comparison between the as-built and hot forged samples

Material	Microstructure	Vicker's hardness	Electrical conductivity	Forging viability
ER316 LSi	✓	✓	✓	✓
ER70S-6	✓	✓	✗	✓
ER410 NiMo	✗	✗	✗	✗
ER1070	✓	✗	✓	✓
ER NiCrMo-3	✓	✗	✗	✓
ER NiCu7	✓	✓	✗	✓
ERCuAl-A2	✓	✓	✗	✓

✓ - Notable differences/ it is viable to forge the material
✗ - No differences detected/ it is not viable to forge the material
✓ - Slight difference

6

Chapter 6
Evaluation of indirect cooling on the part microstructure

6.1 Introduction

In this chapter, the results of the tests carried out with the customized torch and the cooling system are presented.

To assess its effect on the structural properties of the deposited material, as-built and hot forged samples were produced with and without the cooling system and the metallurgical characterization of the produced samples was performed.

During samples manufacturing, thermal analysis was made by thermography and thermocouples.

6.2 Materials and methods

The cooling system presented in Chapter 3 was designed with the aim of increasing the cooling rate during processing in order to prevent grain growth. Moreover, it was intended to develop a versatile and non-intrusive system, which did not added complexity to the movement system or path planning. Thus, the system was designed aiming to cool the shielding gas, that is already used during DED-arc deposition, and simultaneously cool the hammer components, allowing the system to be used either in conventional DED-arc or simultaneously with HF-DED-arc.

Thus, to evaluate the effect of the developed cooling system, two set of samples were produced, with and without cooling, to assess the influence of the cooling of the shielding gas in as-built samples, and another set with hot forging to evaluate the influence of cooling system when combined with the hot forging.

These samples were made with 1 mm diameter wires of stainless steel 316LSi and ER110S-G high strength low alloy steel (HSLA). The selection of these materials was based on the fact that 316LSi does not have solid state transformations, which means that improvements in its properties are not possible to achieve through heat treatments, while the HSLA undergoes transformations in the solid state, which makes it easier to change its properties by heat treatments, though it is a hardenable steel. The chemical composition of each material is given in Table 6.1.

Table 6.1 - Chemical composition of the deposited wires (wt. %)

	C	Si	Mn	Cr	Ni	Mo	Cu	V	Fe
ER 316LSi	0.02	0.9	1.8	18.5	12.5	2.6	--	--	Bal.
ER110S-G	0.08	0.44	1.7	0.23	1.35	0.30	0.25	0.08	Bal.

The samples manufacturing and preparation for microstructural analysis and microhardness measurements were performed with the procedure described in chapter 5.

Regarding the cooling system, the liquid used as coolant was the antifreeze G13, with freezing point of -37 ºC, which is manufactured using glycerine and is commonly used in refrigeration systems. A closed loop system was built between the cooper coil and a tank with 40 L of coolant. This tank works as a thermal mass, enabling the liquid to maintain is low temperature while circulating through the system. Moreover, the coolant was placed in a refrigerator with the capacity to achieve a temperature of approximately -25 ºC.

Thermal analysis was performed with a thermographic infrared (7.5 – 14 µm wavelength) camera Fluke TI400 to monitor the temperature of the sample, hammer and cooling

system. The camera had an accuracy of ± 2 ºC, a measurement limit of -20 to 1200 ºC, a refresh rate of 9 Hz, and a resolution of 320 × 240 pixel. The emissivity was set to 0.84, previously validated using thermocouples. The temperature was measured at any point during the build-up using the acquisition software SmartView. Additionally, both the inlet and outlet of the cooper coil were instrumented with two type-K thermocouples each.

The process parameters selected to deposit the materials were chosen based on the parameters optimised and described in chapter 5. The samples had 10 layers with a length of 100 mm each. Argon 99.99 % was used as shielding gas. The deposition strategy was the Zig-Zag. The remaining process parameters used to produce the samples are shown in Table 6.2.

Table 6.2 - Process parameters for the deposited materials

Material	ER110S-G	ER 316LSi
DED-arc parameters		
WFS [m/min]	3	4
Current RMS [A]	107.2	83.4
TS [m/min]	0.36	0.36
GFR [L/min]	15	15
Welding mode	CW	CW
Interlayer Time [s]	90	60
Voltage [V]	19	19
CTWD [mm]	8	8
Forging parameters		
DAC [mm]	12.5	12.5
Frequency [Hz]	8	8
Duty cycle [%]	50	50
Pressure [bar]	5	5

6.3 Thermal analysis

In DED-arc, one of the main concerns is the formation of directional solidification structure with elongated grains oriented along the building direction that cause anisotropy of the mechanical properties [56]. According to L. Vázquez et al. [165] fast cooling rates can avoid the coarsening of the material microstructure and therefore improve the mechanical properties isotropy. Moreover, most of the developed variants, used high-pressure air cooling systems [105], that may disturb the shielding gas, and thus its application is only viable after the deposition, or far from the torch, which does not allow to act on the cooling rates between the 800 and 500 °C. Since most of the solid state transformations occur within this temperature range, it is important to have the ability to act on these cooling rates, especially in materials as the HSLA, where the final microstructure is highly dependent of the solid state transformations.

Therefore, this work aimed to assess the effects of cooling the shielding gas and the hammer, on the thermal cycles experienced by the parts.

Figure 6.1 shows the thermograms acquired 1 s after the arc extinction of the 10th layer for the samples produced with hot forging in stainless steel 316LSi and HSLA.

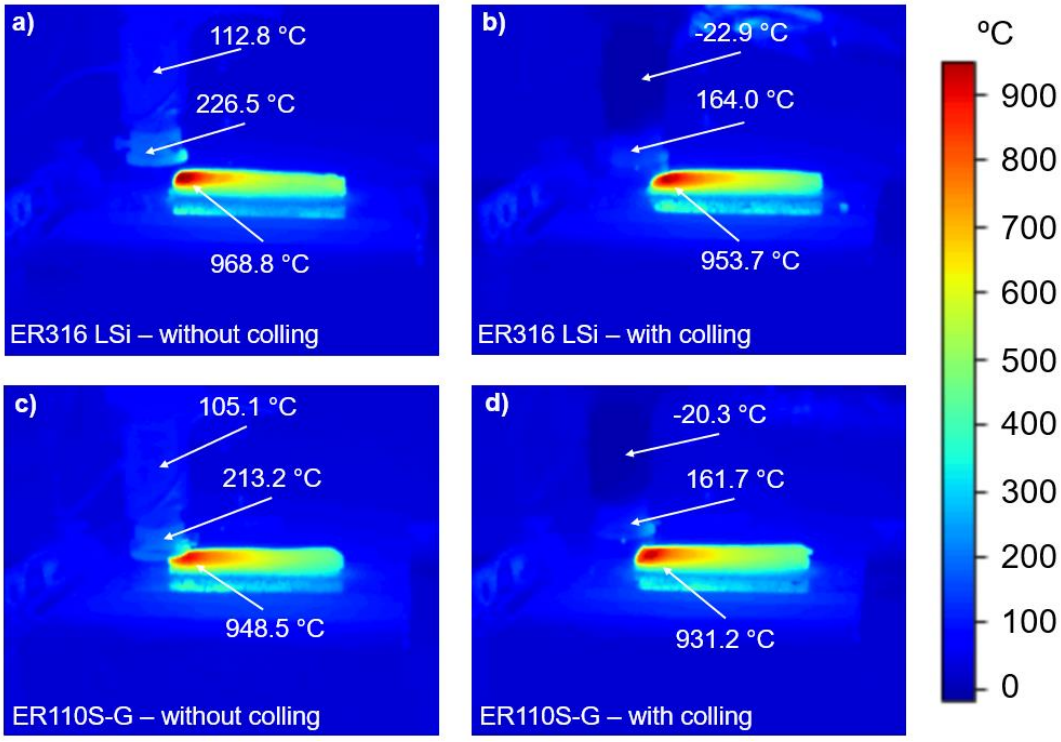

Figure 6.1 - Thermograms obtained 1s after the deposition of the 10th layer of samples produced with hot forging in: a) 316LSi without cooling; b) 316LSi with cooling; c) HSLA without cooling; d) HSLA with cooling

Through these thermograms it was possible to confirm the effect of the cooling system on the torch components during the deposition (nozzle, hammer tip and copper coil). It was verified that during hot forging the average temperature of the hammer is about 50°C lower than when the cooling system was used, while the coil, that is attached to the gas nozzle, is able to maintain the same temperature of the cooling liquid (-25 °C). Additionally, in the samples produced without the cooling system, the nozzle temperature rises to about 110 °C at the end of the deposition of the 10th layer.

The part temperatures depicted in Figure 6.1 were computed from the median of the 10 hottest points in the material and it was observed that with the cooling system the part was 15.1 °C cooler with the 316LSi and 17.3 °C with the HSLA.

Figure 6.2 depicts the evolution of the hammer temperature measured immediately after the arc extinction of each layer. It is observed that the hammer temperature difference increases until it reaches the 50 °C difference observed in thermograms. Moreover, it is also verified that from the 7th layer, the hammer temperature starts to stabilize.

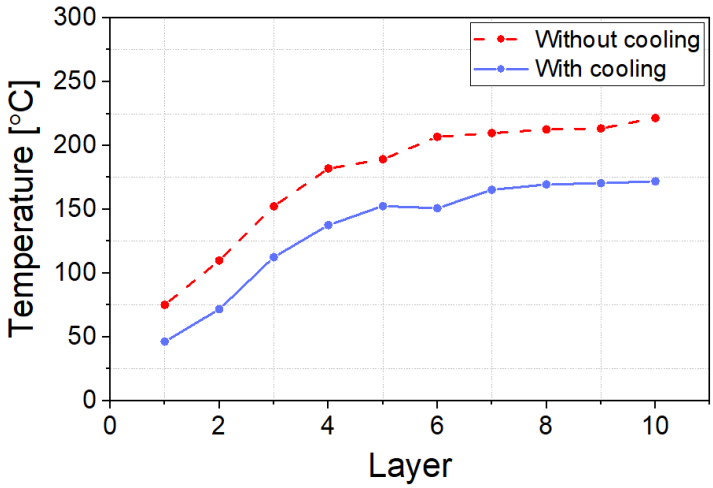

Figure 6.2 - Hammer temperature after the arc extinction of each layer of the samples produced with forging in stainless steel 316LSi

Comparing the temperature of the hammer to the temperature of the material that is forged (~1000 °C), the difference was about 800 °C without the cooling system, and 850 °C with cooling, which represent an increase of 6 %. Therefore, it is tangible that the effect of this temperature variation in the part temperature is not significant.

Furthermore, the thermal cycles experienced by the 5th layer of all the samples were also evaluated and are depicted in Figure 6.3, as well as the material cooling rates between the 800 °C and 500 °C.

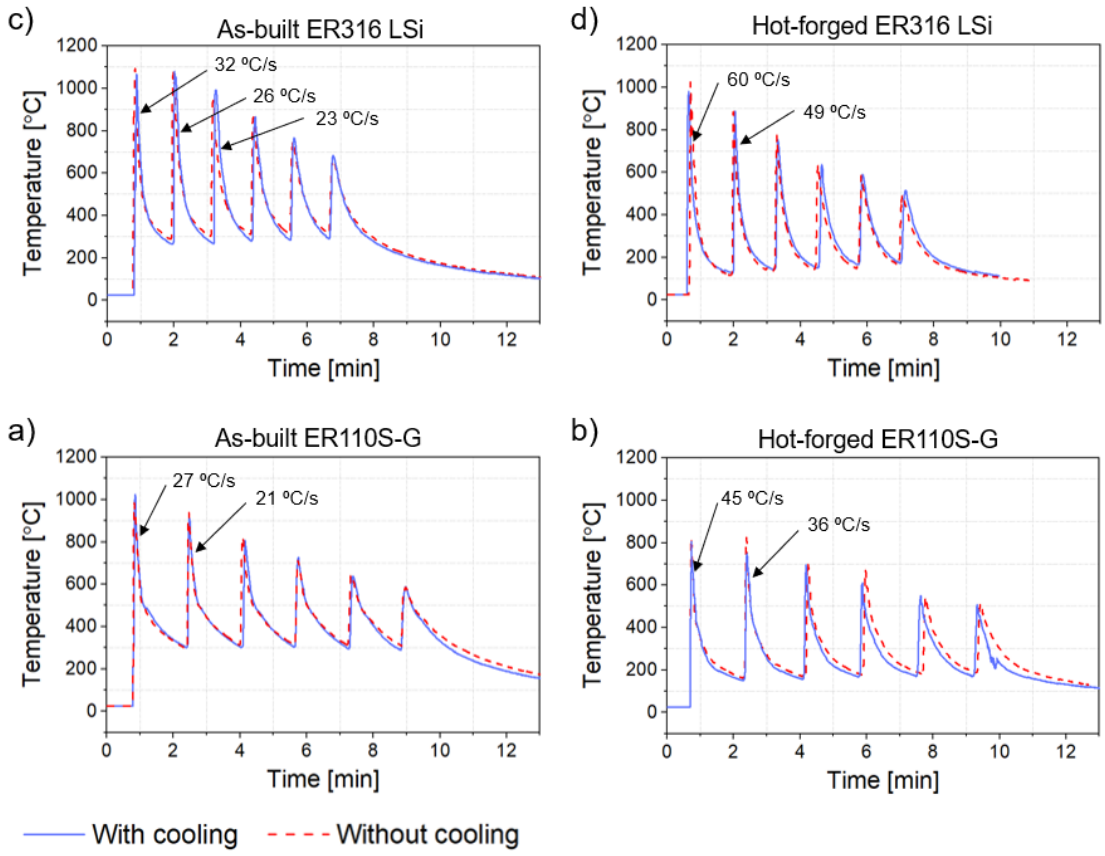

Figure 6.3 - Effect of the cooling system in the thermal cycles of the 5th layer of the samples: a) HSLA as-built; b) HSLA with hot forging; c) 316LSi as-built; d) 316LSi with hot forging

Regarding the cooling rates, this is higher in the samples with hot forged compared to the as-built ones, showing that the hammer increases the part heat dissipation. As a consequence of the higher cooling rate, the base temperature of the thermal cycles is lower than in the as-built samples, and therefore on reheating during deposition of the next layer the maximum temperature reached by the previous layer is also lower in the hot forged samples.

The heat that is removed from the part due to the hot forging occurs during the contact, in which heat from the part is transferred to the hammer, but also due to the fact that the hot forging considerably changes the wall geometry, increasing the width and reducing the height, favouring the heat flow to the previous layers. When the hot forging is applied simultaneously with the cooling system, the cooling does not just occur through the shielding gas, but also through the hammer. Since it is one of the cooled components, when it forges the part it is at a lower temperature than when it is not cooled.

Moreover, it can be seen in Figure 6.3, that with the HSLA, during the deposition of the 7th layer the maximum temperature reached by the 5th layer is approximately 800 °C for the sample without forging and 700 °C for the sample with hot forging. Similar differences

between the as-built and hot forging samples are also verified for the stainless steel 316LSi samples.

Particularly for materials with solid state transformations (as the HSLA), the fact that, due to forging, the peak temperature of the reheating cycles is lower, plays an important role in the material, as this can completely or partially inhibit the solid-state transformations that may occur, thus changing the microstructure of the material.

In addition, variations in the part thermal cycles and cooling rates, due to the use of the cooling system were not observed. To obtain significant variations in the part thermal cycles other authors have developed systems that use compressed air at 0.8 MPa, pointing directly to the part, outside of the gas nozzle during the deposition [166], or after the arc extinction [95].

Since the developed system cools the shielding gas that is already being used to protect the molten pool, the flow rate cannot be increased beyond what is typically used in welding, as this would promote instability in the molten pool and thus the formation of defects such as porosity. Thus, the flow rate used was 15 L/min, with a pressure of 0.025 MPa which is more than one order of magnitude lower than that used by those authors. However, despite the gas flow, used to cool the part, being substantively lower than that of other authors, the developed variant is the only one that by cooling the welding shielding gas acts directly on the molten pool, allowing to act during the solidification of the material while it is at high temperatures, which is not possible in the other variants. Moreover, this variant does not require an increase in the complexity of the torch path, while the variants used by other authors almost always require the need for more complex path planning, due to the need to ensure that the nozzle dedicated to cooling is always over the part.

Therefore, it was intended to verify the effectiveness to increase the thermal gradient within the molten pool and locally change the solidification structure with this simple and versatile cooling system.

To evaluate the heat exchanged by the coolant when passing through the cooper coil, the temperature of the coolant was measured with thermocouples at the coil inlet and outlet. The results for the 316LSi sample with hot forging and cooling are shown in Figure 6.4.

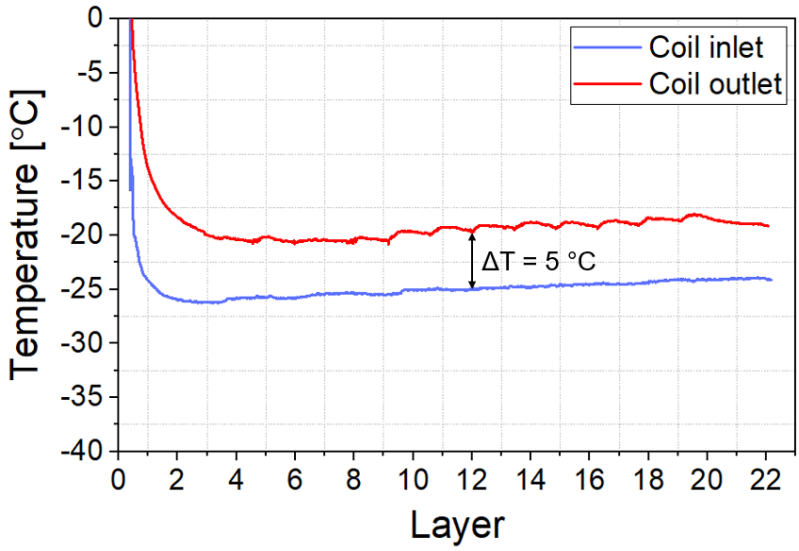

Figure 6.4 - Temperature measurement with thermocouples at coil input and output during the production of the stainless steel 316LSi hot forged sample

It can be observed that there is a constant heat transfer that lowers the liquid temperature by approximately 5 °C. This thermal energy is spent just to keep the adjacent components of the torch at a temperature below room temperature, even without the process operating.

Additionally, during the deposition, the coolant temperature at the output of the coil increases slightly, about 1 °C. This temperature variation is the one that can be considered to calculate the thermal energy that was removed from the part.

Since the flow rate of the coolant through the coil is 2.5 kg/min, the deposition duration is 0.27 min and the specific heat of the coolant liquid is 3400 J/kg ºC, by Eq. 6.1, the amount of energy exchanged by the coolant during the deposition is 2361 J.

$$Q = mC_p\Delta T \qquad \text{Eq. 6.1}$$

In case of 316LSi depositions with the set of parameters mentioned above, the heat input was of 341 J/mm and the deposition length was 100 mm, therefore, the amount of energy delivered to the part during one deposition is 34100 J. When compared to the energy absorbed by the cooling system, during one layer, it accounts only for 6.9 % of the total energy delivered to the part.

Therefore, it is possible to conclude that despite the copper coil being placed immediately above the hammer tip, the heat absorbed by the hammer was not transferred into the cooling system, due to the fact that the hammer tip is an isolated piece, which creates a thermal contact resistance between the hammer and the copper coil component.

6.4 Microstructure and microhardness

6.4.1 Stainless steel - ER316LSi

Since the microstructure of the ER316 LSi varies significantly within the same layer, as discussed in Chapter 5, all micrographs shown in Figure 6.5 were obtained in the centre of each sample, near the fusion line between the sixth and seventh layers.

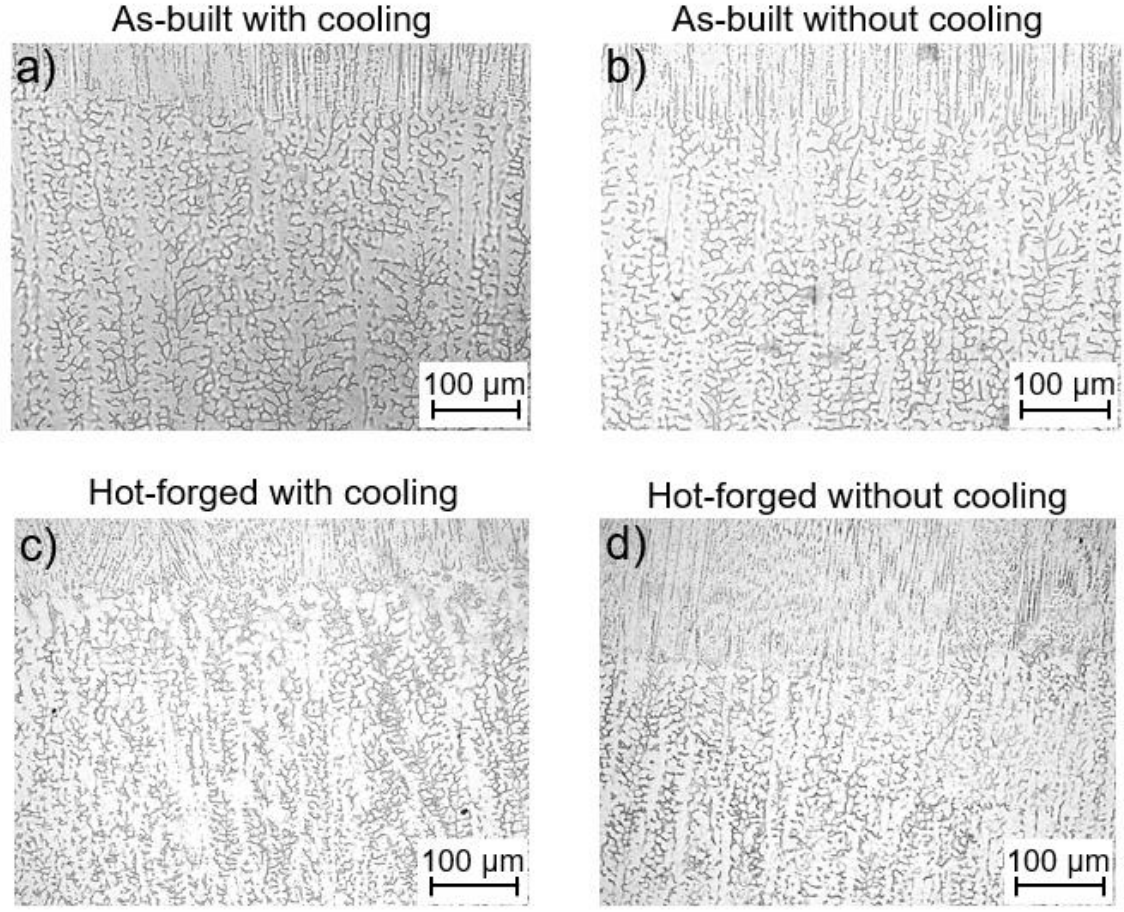

Figure 6.5 - Microstructure obtained at the top of the 6th layer of stainless steel 316LSi samples produced a) as-built with cooling, b) as-built without cooling, c) hot forged with cooling and d) hot forged without cooling

The microstructure observed in all four samples is similar to that described in Chapter 5, where the structure is mostly columnar dendritic with an orientation along the heat flow and perpendicular to the isotherms. Additionally, the structure is constituted, as expected, by primary dendrites of austenite (γ) with some δ ferrite in the interdendritic spaces [142]. Figure 6.6 depicts the results of the dendrite arm spacing measurements performed with *Image J* software.

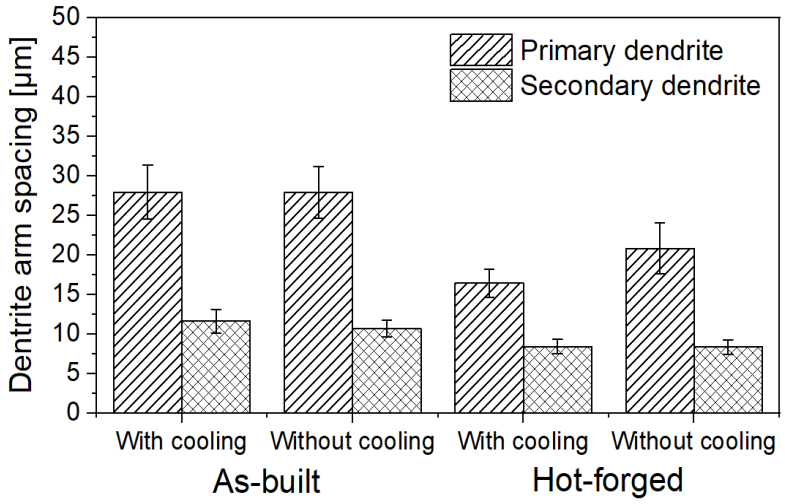

Figure 6.6 - Primary and secondary dendrite arm spacing measured in stainless steel 316LSi samples produced as-built with cooling, as-built without cooling, hot forged with cooling and hot forged without cooling

Analysing by comparison these results, it was observed that the used cooling system does not influence the size of either primary or secondary dendrite arm spacing in the as-built samples, while in the hot forged ones the cooling system has an effect of reducing the primary dendrite arm spacing from 20.8 to 16.4 µm. The results also confirm the effect of the hot forging on the samples microstructure previously observed, where the hot forged samples had less developed primary and secondary dendrite arm spacing compared to the those in the as-built samples.

As discussed earlier, the reduction in the width of the primary dendrite arm spacing promoted by forging occurs due to the increase of nucleation points. During the deposition of a layer, the microstructure develops in the direction of heat flow, forming elongated vertical grains. However, when the material is forged, the microstructure of the upper zone of the layer is refined, and it is on this finer microstructure, that the solidification of the next layer nucleates, promoting competitive grain growth and therefore a thinner microstructure.

The microhardness values measured for each 316LSi sample are showed in Figure 6.7. The measurements were performed along a vertical line in the sample centre, where the spacing between measurements was 1 mm and a load of 4.9 N was used.

The results corroborate what was observed in optical microscopy, showing a hardness increase of the hot forged samples, with an average hardness value of 208 ± 8 HV, while the as-built had an average hardness value of 187 ± 6 HV. This difference in hardness is due to the refined structure seen in the hot forged samples.

Despite the fact that it was observed a slight influence of the cooling system on the hot forged samples, this grain size variations are not sufficient to be noticed in the microhardness values.

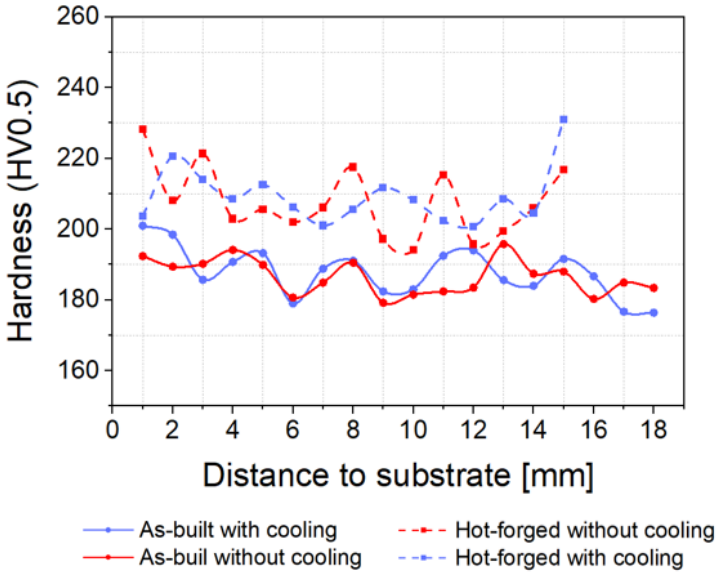

Figure 6.7 - Microhardness profiles of the 316LSi samples produced as-built with cooling, as-built without cooling, hot forged with cooling and hot forged without cooling

6.4.2 High strength low alloy steel – ER110S-G

Figure 6.8 shows representative micrographs of the samples produced in high strength low alloy steel (HSLA) obtained in the center of each sample within the 6th layer.

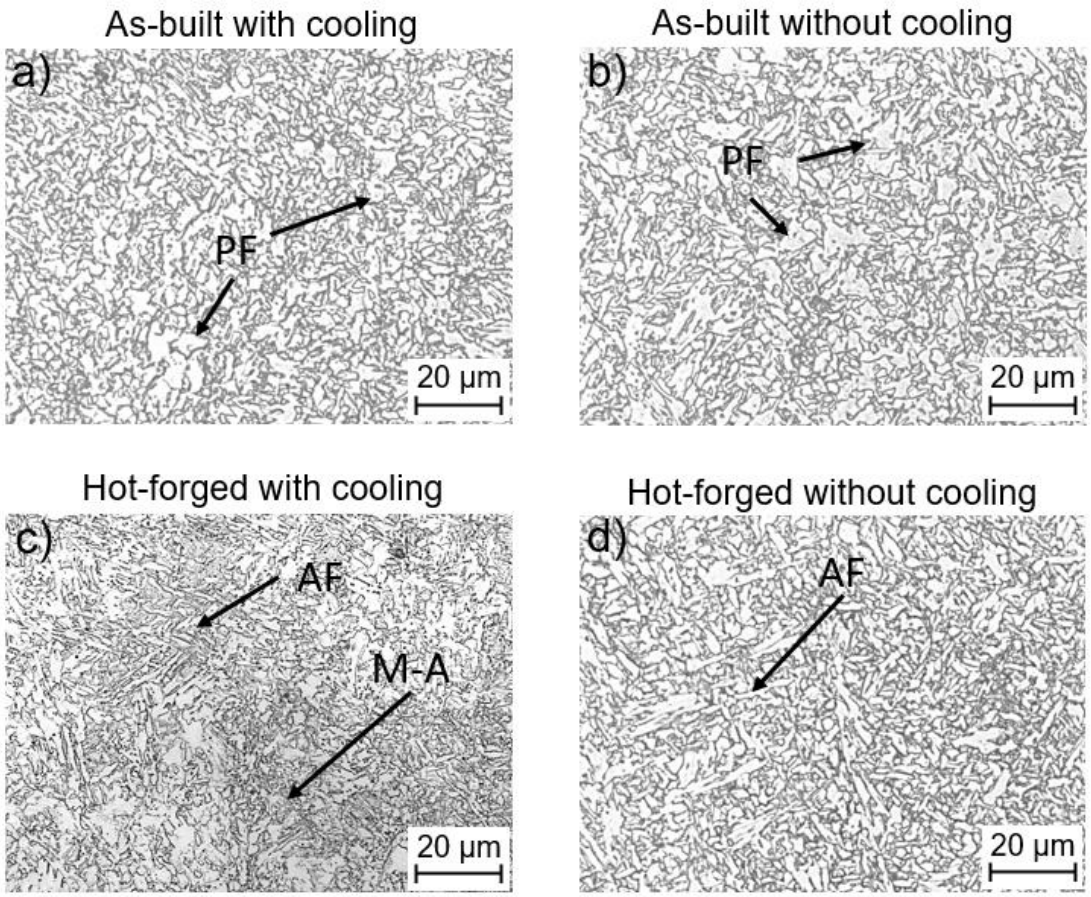

Figure 6.8 - Microstructure obtained at the top of the 6th layer of HSLA steel samples produced a) as-built with cooling, b) as-built without cooling, c) hot forged with cooling and d) hot forged without cooling

Due to the multiple thermal cycles that each layer experiences, the microstructures of the samples were similar to the reheated weld metal in the HSLA steel weldments.

In these steels, the solid-state transformations are responsible for determining the final structure of the component and occur in two temperature ranges: from 1300 to 800 °C, significant austenite grain growth occurs, while below eutectoide temperature , austenite transforms to acicular primary ferrite followed by perlite and eventually bainite [167]. In case of more severe cooling martensite can be formed.

In as-built samples, with and without the cooling system, the microstructure is mainly composed of polygonal ferrite (PF), with no significant differences, neither in morphology nor in size.

In hot forged samples the presence of acicular ferrite (AF) was observed more frequently in the samples produced with the cooling system, there were zones that resemble martensite, eventually with retained austenite (M-A).

Comparing to polygonal ferrite, the formation of acicular ferrite is usually associated with higher cooling rates [168]. However, the hot forging may also promote the recrystallization of the microstructure and increase the nucleation sites for the new austenitic grains, forming a large amount of small austenite grains. These small austenitic grains causes the transformed microstructures to be acicular ferrite dominant [169,170].

During the final stage of cooling to room temperature and depending on the carbon content and higher cooling rates, the remaining austenite can transform partially into martensite and form martensite–austenite (M–A) constituents [171].

In Figure 6.9 are depicted the microhardness values measured on the as-built and hot forged samples produced with and without cooling.

Due to the morphology of constituents, the hot forged samples had an average hardness value (329 ± 24 HV) higher than the as-built ones (280 ± 11 HV). The effect of the cooling system was not possible to identify through changes in the microhardness of the material.

Additionally, samples produced with hot forging had some zones where the hardness exceeds 350 HV, which corroborated the presence of martensite (Figure 6.9).

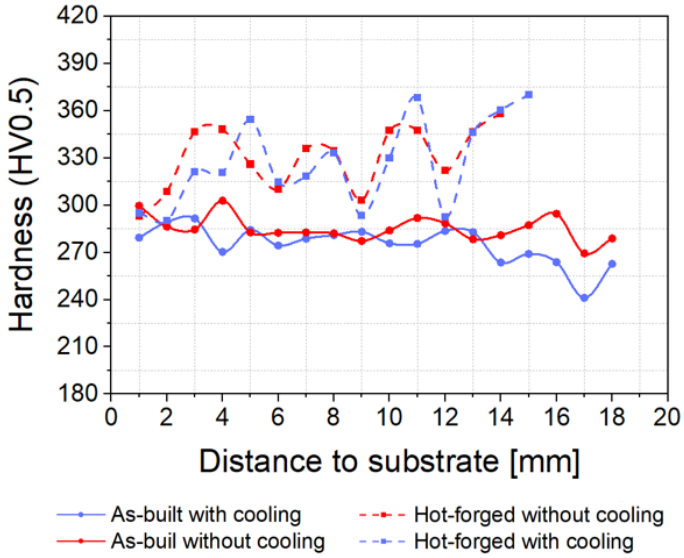

Figure 6.9 - Microhardness profiles of the HSLA steel samples produced as-built with cooling, as-built without cooling, hot forged with cooling and hot forged without cooling

6.5 Summary

The effect of the indirect cooling system on the part was evaluated through thermal analysis and metallurgical characterization of the produced samples.

From the thermal analysis, it was concluded that:

- The cooling coil is able to maintain the same temperature of the cooling liquid during several depositions.

- The cooling system lower the average temperature of the hammer by about 50 °C.

- The amount of energy exchanged by the cooling system during the deposition of one layer was of 2361 J.

- No significant variations promoted by the cooling system alone were observed on the temperature distribution of the part;

- Hot forging can change the heat flow conditions of the part, promoting higher cooling rates, and lower base and peak temperatures during the thermal cycles.

- In the stainless steel 316 LSi, the cooling promoted a reduction of the primary dendrite arm spacing on the hot forged samples

- In the HSLA steel, the cooling simultaneously with hot forging promotes the increase of the transformation of austenite into M-A constituent.

- In both materials, in the as-built samples (without hot forging) were not identified noticeable changes caused by the cooling of the shielding gas.

7

Chapter 7
Conclusions and future work

7.1 Introduction

This chapter presents the main conclusions of the research work, summarizing the knowledge acquired with the development of the prototypes, the feasibility of applying hot forging during deposition in a wide range of materials and the results of the characterization of the effects promoted by the process variant in 316 LSi samples. Several questions have been raised during this work and these are identified in future work description.

7.2 Conclusions

The primary goal of this work was to create know-how and technological innovations to improve the Directed Energy Deposition-arc process and therefore contribute to its industrialization.

In this section, the most relevant conclusions are summarized.

Hot Forging DED-arc

- The proof-of-concept showed that it is possible to take advantage of the high temperatures of the material immediately after its deposition, which allow for plastic deformation with applied forces below 35 N and obtain a constant and uniform deformation on the upper surface of the deposited layer. Thus, the hot forging variant can be incorporated into conventional moving equipment used in DED-arc with low robustness such as XYZ table or a conventional robotic arm.

- It is possible to assign the welding nozzle vertical linear movement, so that it works as a hammer, allowing to carry out the deformation of the material, without compromising the gas protection, the ability to produce parts with high complexity or the production rate of the process. Additionally, this allows for the incorporation of hot forging into a compact DED-arc torch system that can be straightforwardly attached to any moving equipment.

- The dynamic and kinematic characterization of the forging system showed that during the deposition of stainless steel 316LSi, with a pressure of 0.5 MPa applied to the pneumatic cylinders, the average impact force is of 1695 N during 0.3 ms. The stress corresponding to this force is 371.7 MPa which causes an effective true strain of 0.38 at a strain rate of 660 s^{-1}.

- In stainless steel 316LSi, the hot forging effect refines the solidification microstructure by about 50%, thereby improving the mechanical strength. Compared to the as build part, the yield strength increased from 360 to 450 MPa, the ultimate tensile strength improved from 574 to 622 MPa, while elongation to fracture reduced from 32 to 28 %. This increase in mechanical properties at expense of ductility, allows parts produced by HF-DED-arc to comply with the requirements of the ASTM A666-15 standard. The analysis of the 2D Debbye-Scherrer diffraction rings evidence a strong texture on the as-built that clearly indicating a reduction in material anisotropy.

- In mild steel and Inconel 625, the effectiveness of hot forging in promoting dynamic recrystallization on the top layer was verified. A recrystallized zone with a depth of 0.9 mm and 0.67 mm were achieved for the mild steel and Inconel 625,

respectively. In Inconel 625, the increase of microstructural nucleation sites due to hot forging, was seen to reduce the primary dendrite arm spacing from 14.7 µm to 8.7 µm.

- In aluminium 1070 and Monel 400 the achieved depth of the dynamic recrystallized zone, caused by the hot forging, was greater than the penetration depth of the subsequent layer, resulting in a recrystallized microstructure zone in between layers, which prevents the epitaxial grain growth between consecutive layers, thus reducing the microstructural anisotropy of the samples.

- In copper aluminium alloy the application of hot forging clearly refines and homogenizes the microstructure. The compressive strength measured showed a more homogeneous resistance in vertical and horizontal directions when the part was hot forged, while the as-built part has a more significant difference in both directions.

- The hot forging influences porosities, changing its morphology from sphere-shaped pores into an ellipsoid shape. In some cases, it completely collapsed the porosity.

- The flat geometry of the upper surface of each layer, left by the hot forging, also represents a significant advantage, as it simplify the coupling of ultrasonic or eddy currents probes for inspection by non-destructive tests.

- The developed customized torch for hot forging DED-arc accomplished the requirements and was adequate to produce the samples, and therefore, future parts. The developed 3D printer also proved to be suitable for the developed research.

Indirect Cooling DED-arc

- The indirect cooling system developed showed to be able to lower the average temperature of the nozzle and the hammer by about 50 °C during consecutive depositions.

- The low hammer temperature reduced the dendrite arm spacing in the 316 LSi, and increased the transformation of austenite into martensite in the HSLA steel.

- Hot forging, can change the heat flow conditions of the part, promoting higher cooling rates, and lower base and peak temperatures during the thermal cycles.

- The cooling of the shielding gas had no effect on the cooling rates nor the microstructure of both materials. The observed effects on the deposited materials are mostly due to the cooler hammer.

7.3 Future work

Considering that this work focused mainly on the development of new technological variants that would allow to mitigate typical defects in DED-arc, and that the feasibility of the proposed concepts was proven, validated, and studied in detail, particularly in the stainless steel 316LSi, several proposals for future work can be foreseen.

A detailed study is suggested using the methodology based on design of experiments, to assess the quantitative effect of the main forging parameters (forging frequency and pressure) on the depth of the recrystallized zone induced by forging, in materials such as mild steel, Inconel 625 or Monel 400, as well as on the microstructure and mechanical properties of the material.

A more detailed study focused on materials science on the dynamic recrystallization mechanisms that occur during hot forging should be of interest, as well as verifying whether forging promotes dislocations in the microstructure of the material that remain after deposition and that can give rise to static recrystallization in a subsequent heat treatment.

Another material that has a received a lot of interest by the researchers but was not possible to study in this work is titanium and its alloys, due to their application in the aeronautical and aerospace. Since during deposition with conventional DED-arc is developed a coarser and oriented microstructure, resulting in strong anisotropy of mechanical properties, as described in the literature review, the deposition of titanium alloys with HF-DED-arc technique, might be beneficial to refine the microstructure and reduce anisotropy, as it has been verified in this work in other materials.

It is also important the development numerical models that allow to simulate the deposition of material simultaneously with the deformation, thus allowing to predict the forging conditions.

Regarding the indirect cooling system, design improvements must be made, with the aim of maximizing the removal of heat from the hammer, and consequently from the part.

References

[1] X. Yao, Y. Lin, Emerging manufacturing paradigm shifts for the incoming industrial revolution, Int. J. Adv. Manuf. Technol. 85 (2016) 1665–1676. https://doi.org/10.1007/s00170-015-8076-0.

[2] M. Simons, Additive manufacturing—a revolution in progress? Insights from a multiple case study, Int. J. Adv. Manuf. Technol. 96 (2018) 735–749. https://doi.org/10.1007/s00170-018-1601-1.

[3] B. Berman, 3-D printing: The new industrial revolution, Bus. Horiz. 55 (2012) 155–162. https://doi.org/10.1016/j.bushor.2011.11.003.

[4] T.A. Rodrigues, V. Duarte, R.M. Miranda, T.G. Santos, J.P. Oliveira, Current Status and Perspectives on Wire and Arc Additive Manufacturing (WAAM), Materials (Basel). 12 (2019) 1121. https://doi.org/10.3390/ma12071121.

[5] ASTM A666-15, Standard Specification for Annealed or Cold-Worked Austenitic Stainless Steel Sheet, Strip, Plate, and Flat Bar, (2016).

[6] T. DebRoy, H.L. Wei, J.S. Zuback, T. Mukherjee, J.W. Elmer, J.O. Milewski, A.M. Beese, A. Wilson-Heid, A. De, W. Zhang, Additive manufacturing of metallic components – Process, structure and properties, Prog. Mater. Sci. 92 (2018) 112–224. https://doi.org/10.1016/j.pmatsci.2017.10.001.

[7] ISO/ASTM-52900:2015, Additive manufacturing — General principles — Terminology, (2015).

[8] N. Rodriguez, L. Vázquez, I. Huarte, E. Arruti, I. Tabernero, P. Alvarez, Wire and arc additive manufacturing: a comparison between CMT and TopTIG processes applied to stainless steel, Weld. World. 62 (2018) 1083–1096. https://doi.org/10.1007/S40194-018-0606-6.

[9] Ivántabernero, A. Paskual, P. Álvarez, A. Suárez, Study on Arc Welding Processes for High Deposition Rate Additive Manufacturing, Procedia CIRP. 68 (2018) 358–362. https://doi.org/10.1016/j.procir.2017.12.095.

[10] J. Liu, Y. Xu, Y. Ge, Z. Hou, S. Chen, Wire and arc additive manufacturing of metal components: a review of recent research developments, Int. J. Adv. Manuf. Technol. 111 (2020) 149–198. https://doi.org/10.1007/S00170-020-05966-8.

[11] O.S. Jose F, L. Quintino, Processos de soldadura, Lisbon, 1998.

[12] ASM International, Volume 6: Welding, Brazing, and Soldering, 1993.

[13] G. Mathers, The welding of aluminium and its alloys, Woodhead Publishing; 1st edition, Cambridge England, 2002.

[14] W. Aiyiti, W. Zhao, B. Lu, Y. Tang, Investigation of the overlapping parameters of MPAW-based rapid prototyping, Rapid Prototyp. J. 12 (2006) 165–172. https://doi.org/10.1108/13552540610670744.

[15] J.G. Mercado Rojas, T. Wolfe, B.A. Fleck, A.J. Qureshi, Plasma transferred arc additive manufacturing of Nickel metal matrix composites, Manuf. Lett. 18 (2018) 31–34. https://doi.org/10.1016/J.MFGLET.2018.10.001.

[16] E.A. Alberti, B.M.P. Bueno, A.S.C.M. D'Oliveira, Additive manufacturing using plasma transferred arc, Int. J. Adv. Manuf. Technol. 83 (2016) 1861–1871. https://doi.org/10.1007/s00170-015-7697-7.

[17] T. Artaza, A. Suárez, F. Veiga, I. Braceras, I. Tabernero, O. Larrañaga, A. Lamikiz, Wire arc additive manufacturing Ti6Al4V aeronautical parts using plasma arc welding: Analysis of heat-treatment processes in different atmospheres, J. Mater. Res. Technol. 9 (2020) 15454–15466. https://doi.org/10.1016/J.JMRT.2020.11.012.

[18] C. Xia, Z. Pan, S. Zhang, J. Polden, L. Wang, H. Li, Y. Xu, S. Chen, Model predictive control of layer width in wire arc additive manufacturing, J. Manuf. Process. 58 (2020) 179–186. https://doi.org/10.1016/J.JMAPRO.2020.07.060.

[19] M. Dinovitzer, X. Chen, J. Laliberte, X. Huang, H. Frei, Effect of wire and arc additive manufacturing (WAAM) process parameters on bead geometry and microstructure, Addit. Manuf. 26 (2019) 138–146. https://doi.org/10.1016/J.ADDMA.2018.12.013.

[20] M. Karmuhilan, A.K. Sood, Intelligent process model for bead geometry prediction in WAAM, Mater. Today Proc. 5 (2018) 24005–24013. https://doi.org/10.1016/J.MATPR.2018.10.193.

[21] S.W. Williams, F. Martina, A.C. Addison, J. Ding, G. Pardal, P. Colegrove, Wire + Arc Additive Manufacturing, Mater. Sci. Technol. 32 (2016) 641–647. https://doi.org/10.1179/1743284715Y.0000000073.

[22] X. Chen, C. Su, Y. Wang, A.N. Siddiquee, K. Sergey, S. Jayalakshmi, R.A. Singh, Cold Metal Transfer (CMT) Based Wire and Arc Additive Manufacture (WAAM) System, J. Surf. Investig. X-Ray, Synchrotron Neutron Tech. 12 (2019) 1278–1284. https://doi.org/10.1134/S102745101901004X.

[23] C.R. Cunningham, J.M. Flynn, A. Shokrani, V. Dhokia, S.T. Newman, Invited review article: Strategies and processes for high quality wire arc additive manufacturing, Addit. Manuf. 22 (2018) 672–686. https://doi.org/10.1016/j.addma.2018.06.020.

[24] H.E. Coules, P. Colegrove, L.D. Cozzolino, S.W. Wen, Experimental measurement of biaxial thermal stress fields caused by arc welding, J. Mater. Process. Technol. 212 (2012) 962–968. https://doi.org/10.1016/j.jmatprotec.2011.12.006.

[25] P.J. Withers, H.K.D.H. Bhadeshia, Residual stress part 2 - Nature and origins, Mater. Sci. Technol. 17 (2001) 366–375.´ https://doi.org/10.1179/026708301101510087.

[26] W.J. Sames, F.A. List, S. Pannala, R.R. Dehoff, S.S. Babu, The metallurgy and

processing science of metal additive manufacturing, Int. Mater. Rev. 61 (2016) 315–360. https://doi.org/10.1080/09506608.2015.1116649.

[27] J. Ding, P. Colegrove, J. Mehnen, S. Ganguly, P.M. Sequeira Almeida, F. Wang, S. Williams, Thermo-mechanical analysis of Wire and Arc Additive Layer Manufacturing process on large multi-layer parts, Comput. Mater. Sci. 50 (2011) 3315–3322. https://doi.org/10.1016/j.commatsci.2011.06.023.

[28] F. Martina, M.J. Roy, B.A. Szost, S. Terzi, P.A. Colegrove, S.W. Williams, P.J. Withers, J. Meyer, M. Hofmann, Residual stress of as-deposited and rolled wire+arc additive manufacturing Ti–6Al–4V components, Mater. Sci. Technol. 32 (2016) 1439–1448. https://doi.org/10.1080/02670836.2016.1142704.

[29] P.A. Colegrove, H.E. Coules, J. Fairman, F. Martina, T. Kashoob, H. Mamash, L.D. Cozzolino, Microstructure and residual stress improvement in wire and arc additively manufactured parts through high-pressure rolling, J. Mater. Process. Technol. 213 (2013) 1782–1791. https://doi.org/10.1016/j.jmatprotec.2013.04.012.

[30] N. Hoye, H.J. Li, D. Cuiuri, A. Paradowska, Measurement of residual stresses in titanium aerospace components formed via additive manufacturing, Mater. Sci. Forum. 777 (2014) 124–129. https://doi.org/10.4028/www.scientific.net/MSF.777.124.

[31] B.A. Szost, S. Terzi, F. Martina, D. Boisselier, A. Prytuliak, T. Pirling, M. Hofmann, D.J. Jarvis, A comparative study of additive manufacturing techniques: Residual stress and microstructural analysis of CLAD and WAAM printed Ti-6Al-4V components, Mater. Des. 89 (2016) 559–567. https://doi.org/10.1016/j.matdes.2015.09.115.

[32] C. Shen, M. Reid, K.D. Liss, Z. Pan, Y. Ma, D. Cuiuri, S. van Duin, H. Li, Neutron diffraction residual stress determinations in Fe3Al based iron aluminide components fabricated using wire-arc additive manufacturing (WAAM), Addit. Manuf. 29 (2019) 100774. https://doi.org/10.1016/j.addma.2019.06.025.

[33] B. Wu, Z. Pan, D. Ding, D. Cuiuri, H. Li, J. Xu, J. Norrish, A review of the wire arc additive manufacturing of metals: properties, defects and quality improvement, J. Manuf. Process. 35 (2018) 127–139. https://doi.org/10.1016/j.jmapro.2018.08.001.

[34] R. Li, J. Xiong, Influence of interlayer dwell time on stress field of thin-walled components in WAAM via numerical simulation and experimental tests, Rapid Prototyp. J. 25 (2019) 1433–1441. https://doi.org/10.1108/RPJ-03-2019-0067.

[35] M.P. Mughal, R.A. Mufti, H. Fawad, The mechanical effects of deposition patterns in welding-bflsed layered manufacturing, Proc. Inst. Mech. Eng. Part B J. Eng. Manuf. 221 (2007) 1499–1509. https://doi.org/10.1243/09544054JEM783.

[36] C. Zhang, C. Shen, X. Hua, F. Li, Y. Zhang, Y. Zhu, Influence of wire-arc additive manufacturing path planning strategy on the residual stress status in one single buildup layer, Int. J. Adv. Manuf. Technol. 111 (2020) 797–806. https://doi.org/10.1007/s00170-020-06178-w.

[37] Q. Chen, J. Liu, X. Liang, A.C. To, A level-set based continuous scanning path optimization method for reducing residual stress and deformation in metal additive manufacturing, Comput. Methods Appl. Mech. Eng. 360 (2020) 112–119. https://doi.org/10.1016/j.cma.2019.112719.

[38] R. Biswal, X. Zhang, A.K. Syed, M. Awd, J. Ding, F. Walther, S. Williams, Criticality

of porosity defects on the fatigue performance of wire + arc additive manufactured titanium alloy, Int. J. Fatigue. 122 (2019) 208–217. https://doi.org/10.1016/j.ijfatigue.2019.01.017.

[39] J.L. Gu, J.L. Ding, B.Q. Cong, J. Bai, H.M. Gu, S.W. Williams, Y.C. Zhai, The Influence of Wire Properties on the Quality and Performance of Wire+Arc Additive Manufactured Aluminium Parts, Adv. Mater. Res. 1081 (2014) 210–214. https://doi.org/10.4028/www.scientific.net/amr.1081.210.

[40] V.I. Ryazantsev, V.A. Fedoseev, Metallurgical and technological porosity of aluminium alloys in arc welding, Weld. Int. 16 (2002) 320–324. https://doi.org/10.1080/09507110209549538.

[41] D.H. Kam, T.H. Lee, D.Y. Kim, J. Kim, M. Kang, Weld quality improvement and porosity reduction mechanism of zinc coated steel using tandem gas metal arc welding (GMAW), J. Mater. Process. Technol. 294 (2021) 117–127. https://doi.org/10.1016/j.jmatprotec.2021.117127.

[42] B. Cong, J. Ding, S. Williams, Effect of arc mode in cold metal transfer process on porosity of additively manufactured Al-6.3%Cu alloy, Int. J. Adv. Manuf. Technol. 76 (2015) 1593–1606. https://doi.org/10.1007/s00170-014-6346-x.

[43] M. Arana, E. Ukar, I. Rodriguez, A. Iturrioz, P. Alvarez, Strategies to reduce porosity in Al-Mg WAAM parts and their impact on mechanical properties, Metals (Basel). 11 (2021) 524. https://doi.org/10.3390/met11030524.

[44] Y. Yehorov, L.J. da Silva, A. Scotti, Exploring the use of switchback for mitigating homoepitaxial unidirectional grain growth and porosity in WAAM of aluminium alloys, Int. J. Adv. Manuf. Technol. 104 (2019) 1581–1592. https://doi.org/10.1007/s00170-019-03959-w.

[45] J.C. Lippold, Welding Metallurgy and Weldability, Wiley Blackwell, 2014. https://onlinelibrary.wiley.com/doi/book/10.1002/9781118960332 (accessed July 18, 2021).

[46] J.R. Kennedy, A.E. Davis, A. Caballero, A. Garner, J. Donoghue, S. Williams, J. Zollinger, E. Bouzy, E.J. Pickering, P.B. Prangnell, Isomorphic grain inoculation in Ti-6Al-4V during additive manufacturing, Mater. Lett. X. 8 (2020) 100057. https://doi.org/10.1016/J.MLBLUX.2020.100057.

[47] J.R. Kennedy, A.E. Davis, A.E. Caballero, S. Williams, E.J. Pickering, P.B. Prangnell, The potential for grain refinement of Wire-Arc Additive Manufactured (WAAM) Ti-6Al-4V by ZrN and TiN inoculation, Addit. Manuf. 40 (2021) 101928. https://doi.org/10.1016/J.ADDMA.2021.101928.

[48] T.A. Rodrigues, V.R. Duarte, D. Tomás, J.A. Avila, J.D. Escobar, E. Rossinyol, N. Schell, T.G. Santos, J.P. Oliveira, In-situ strengthening of a high strength low alloy steel during Wire and Arc Additive Manufacturing (WAAM), Addit. Manuf. 34 (2020) 101200. https://doi.org/10.1016/J.ADDMA.2020.101200.

[49] S. Zhou, K. Wu, G. Yang, F. Deng, N. Hou, L. Qin, W. Wei, Grain-refining of wire arc additive manufactured aluminum alloy with Nb powder addition, Mater. Res. Express. 8 (2021) 026520. https://doi.org/10.1088/2053-1591/ABE6D5.

[50] T.A. Rodrigues, V. Duarte, J.A. Avila, T.G. Santos, R.M. Miranda, J.P. Oliveira, Wire and arc additive manufacturing of HSLA steel: Effect of thermal cycles on microstructure and mechanical properties, Addit. Manuf. 27 (2019) 440–450. https://doi.org/10.1016/J.ADDMA.2019.03.029.

[51] H.L. Wei, T. Mukherjee, T. DebRoy, Grain Growth Modeling for Additive Manufacturing of Nickel Based Superalloys, Proc. 6th Int. Conf. Recryst. Grain Growth. (2016) 265–269. https://doi.org/10.1007/978-3-319-48770-0_39.

[52] F. Yan, W. Xiong, E.J. Faierson, Grain Structure Control of Additively Manufactured Metallic Materials, Materials (Basel). 10 (2017) 1260. https://doi.org/10.3390/MA10111260.

[53] F. Wang, S. Williams, M. Rush, Morphology investigation on direct current pulsed gas tungsten arc welded additive layer manufactured Ti6Al4V alloy, Int. J. Adv. Manuf. Technol. 57 (2011) 597–603. https://doi.org/10.1007/S00170-011-3299-1.

[54] G.P. Dinda, A.K. Dasgupta, J. Mazumder, Texture control during laser deposition of nickel-based superalloy, Scr. Mater. 67 (2012) 503–506. https://doi.org/10.1016/J.SCRIPTAMAT.2012.06.014.

[55] G. Marinelli, F. Martina, S. Ganguly, S. Williams, Grain refinement in an unalloyed tantalum structure by combining Wire+Arc additive manufacturing and vertical cold rolling, Addit. Manuf. 32 (2020) 101009. https://doi.org/10.1016/j.addma.2019.101009.

[56] X. Lu, Y.F. Zhou, X.L. Xing, L.Y. Shao, Q.X. Yang, S.Y. Gao, Open-source wire and arc additive manufacturing system: formability, microstructures, and mechanical properties, Int. J. Adv. Manuf. Technol. 93 (2017) 2145–2154. https://doi.org/10.1007/S00170-017-0636-Z.

[57] Y. Kok, X.P. Tan, P. Wang, M.L.S. Nai, N.H. Loh, E. Liu, S.B. Tor, Anisotropy and heterogeneity of microstructure and mechanical properties in metal additive manufacturing: A critical review, Mater. Des. 139 (2018) 565–586. https://doi.org/10.1016/J.MATDES.2017.11.021.

[58] F. Wang, S. Williams, P. Colegrove, A.A. Antonysamy, Microstructure and Mechanical Properties of Wire and Arc Additive Manufactured Ti-6Al-4V, Metall. Mater. Trans. A. 44 (2013) 968–977. https://doi.org/10.1007/s11661-012-1444-6.

[59] V. Laghi, M. Palermo, L. Tonelli, G. Gasparini, L. Ceschini, T. Trombetti, Tensile properties and microstructural features of 304L austenitic stainless steel produced by wire-and-arc additive manufacturing, Int. J. Adv. Manuf. Technol. 106 (2020) 3693–3705. https://doi.org/10.1007/S00170-019-04868-8.

[60] L. Sun, F. Jiang, R. Huang, D. Yuan, C. Guo, J. Wang, Anisotropic mechanical properties and deformation behavior of low-carbon high-strength steel component fabricated by wire and arc additive manufacturing, Mater. Sci. Eng. A. 787 (2020) 139514. https://doi.org/10.1016/J.MSEA.2020.139514.

[61] W. Jin, C. Zhang, S. Jin, Y. Tian, D. Wellmann, W. Liu, Wire Arc Additive Manufacturing of Stainless Steels: A Review, Appl. Sci. 10 (2020) 1563. https://doi.org/10.3390/APP10051563.

[62] J. V. Gordon, C. V. Haden, H.F. Nied, R.P. Vinci, D.G. Harlow, Fatigue crack growth anisotropy, texture and residual stress in austenitic steel made by wire and arc additive manufacturing, Mater. Sci. Eng. A. 724 (2018) 431–438. https://doi.org/10.1016/J.MSEA.2018.03.075.

[63] L. Wang, J. Xue, Q. Wang, Correlation between arc mode, microstructure, and mechanical properties during wire arc additive manufacturing of 316L stainless steel, Mater. Sci. Eng. A. 751 (2019) 183–190. https://doi.org/10.1016/J.MSEA.2019.02.078.

[64] W. Wu, J. Xue, L. Wang, Z. Zhang, Y. Hu, C. Dong, Forming Process, Microstructure, and Mechanical Properties of Thin-Walled 316L Stainless Steel Using Speed-Cold-Welding Additive Manufacturing, Metals (Basel). 9 (2019) 109. https://doi.org/10.3390/MET9010109.

[65] Y. Ali, P. Henckell, J. Hildebrand, J. Reimann, J.P. Bergmann, S. Barnikol-Oettler, Wire arc additive manufacturing of hot work tool steel with CMT process, J. Mater. Process. Technol. 269 (2019) 109–116. https://doi.org/10.1016/J.JMATPROTEC.2019.01.034.

[66] A.S. Yildiz, K. Davut, B. Koc, O. Yilmaz, Wire arc additive manufacturing of high-strength low alloy steels: study of process parameters and their influence on the bead geometry and mechanical characteristics, Int. J. Adv. Manuf. Technol. 108 (2020) 3391–3404. https://doi.org/10.1007/S00170-020-05482-9.

[67] A. Ayed, A. Valencia, G. Bras, H. Bernard, P. Michaud, Y. Balcaen, J. Alexis, Effects of WAAM Process Parameters on Metallurgical and Mechanical Properties of Ti-6Al-4V Deposits, Lect. Notes Mech. Eng. (2020) 26–35. https://doi.org/10.1007/978-3-030-24247-3_4.

[68] M. Liberini, A. Astarita, G. Campatelli, A. Scippa, F. Montevecchi, G. Venturini, M. Durante, L. Boccarusso, F.M.C. Minutolo, A. Squillace, Selection of Optimal Process Parameters for Wire Arc Additive Manufacturing, Procedia CIRP. 62 (2017) 470–474. https://doi.org/10.1016/J.PROCIR.2016.06.124.

[69] P.A. Colegrove, F. Martina, M.J. Roy, B.A. Szost, S. Terzi, S.W. Williams, P.J. Withers, D. Jarvis, High pressure interpass rolling of Wire + Arc additively manufactured titanium components, Adv. Mater. Res. 996 (2014) 694–700. https://doi.org/10.4028/www.scientific.net/AMR.996.694.

[70] F. Martina, P.A. Colegrove, S.W. Williams, J. Meyer, Microstructure of Interpass Rolled Wire + Arc Additive Manufacturing Ti-6Al-4V Components, Metall. Mater. Trans. A. 46 (2015) 6103–6118. https://doi.org/10.1007/s11661-015-3172-1.

[71] J. Donoghue, A.A. Antonysamy, F. Martina, P.A. Colegrove, S.W. Williams, P.B. Prangnell, The effectiveness of combining rolling deformation with Wire-Arc Additive Manufacture on β-grain refinement and texture modification in Ti-6Al-4V, Mater. Charact. 114 (2016) 103–114. https://doi.org/10.1016/j.matchar.2016.02.001.

[72] J.R. Hönnige, P.A. Colegrove, B. Ahmad, M.E. Fitzpatrick, S. Ganguly, T.L. Lee, S.W. Williams, Residual stress and texture control in Ti-6Al-4V wire + arc additively manufactured intersections by stress relief and rolling, Mater. Des. 150 (2018) 193–205. https://doi.org/10.1016/J.MATDES.2018.03.065.

[73] F. Martina, M.J. Roy, B.A. Szost, S. Terzi, P.A. Colegrove, S.W. Williams, P.J. Withers, J. Meyer, M. Hofmann, Residual stress of as-deposited and rolled wire+arc additive manufacturing Ti–6Al–4V components, Mater. Sci. Technol. (United Kingdom). 32 (2016) 1439–1448. https://doi.org/10.1080/02670836.2016.1142704.

[74] J. Gu, J. Ding, S.W. Williams, H. Gu, P. Ma, Y. Zhai, The effect of inter-layer cold working and post-deposition heat treatment on porosity in additively manufactured aluminum alloys, J. Mater. Process. Technol. 230 (2016) 26–34. https://doi.org/10.1016/J.JMATPROTEC.2015.11.006.

[75] J. Gu, J. Ding, S.W. Williams, H. Gu, J. Bai, Y. Zhai, P. Ma, The strengthening effect of inter-layer cold working and post-deposition heat treatment on the

additively manufactured Al–6.3Cu alloy, Mater. Sci. Eng. A. 651 (2016) 18–26. https://doi.org/10.1016/J.MSEA.2015.10.101.

[76] J. Gu, X. Wang, J. Bai, J. Ding, S. Williams, Y. Zhai, K. Liu, Deformation microstructures and strengthening mechanisms for the wire+arc additively manufactured Al-Mg4.5Mn alloy with inter-layer rolling, Mater. Sci. Eng. A. 712 (2018) 292–301. https://doi.org/10.1016/J.MSEA.2017.11.113.

[77] J.R. Hönnige, P.A. Colegrove, S. Ganguly, E. Eimer, S. Kabra, S. Williams, Control of residual stress and distortion in aluminium wire + arc additive manufacture with rolling, Addit. Manuf. 22 (2018) 775–783. https://doi.org/10.1016/J.ADDMA.2018.06.015.

[78] X. Xu, S. Ganguly, J. Ding, C.E. Seow, S. Williams, Enhancing mechanical properties of wire + arc additively manufactured INCONEL 718 superalloy through in-process thermomechanical processing, Mater. Des. 160 (2018) 1042–1051. https://doi.org/10.1016/j.matdes.2018.10.038.

[79] J. Hönnige, C.E. Seow, S. Ganguly, X. Xu, S. Cabeza, H. Coules, S. Williams, Study of residual stress and microstructural evolution in as-deposited and inter-pass rolled wire plus arc additively manufactured Inconel 718 alloy after ageing treatment, Mater. Sci. Eng. A. 801 (2021) 140368. https://doi.org/10.1016/j.msea.2020.140368.

[80] Y. Xie, H. Zhang, F. Zhou, Improvement in Geometrical Accuracy and Mechanical Property for Arc-Based Additive Manufacturing Using Metamorphic Rolling Mechanism, J. Manuf. Sci. Eng. 138 (2016). https://doi.org/10.1115/1.4032079.

[81] P. Dirisu, G. Supriyo, F. Martina, X. Xu, S. Williams, Wire plus arc additive manufactured functional steel surfaces enhanced by rolling, Int. J. Fatigue. 130 (2020) 105237. https://doi.org/10.1016/j.ijfatigue.2019.105237.

[82] J.R. Hönnige, P. Colegrove, S. Williams, Improvement of microstructure and mechanical properties in Wire + Arc Additively Manufactured Ti-6Al-4V with Machine Hammer Peening, Procedia Eng. 216 (2017) 8–17. https://doi.org/10.1016/J.PROENG.2018.02.083.

[83] J.R. Hönnige, A.E. Davis, A. Ho, J.R. Kennedy, L. Neto, P. Prangnell, S. Williams, The Effectiveness of Grain Refinement by Machine Hammer Peening in High Deposition Rate Wire-Arc AM Ti-6Al-4V, Metall. Mater. Trans. A Phys. Metall. Mater. Sci. 51 (2020) 3692–3703. https://doi.org/10.1007/s11661-020-05781-6.

[84] J. Donoghue, A.E. Davis, C.S. Daniel, A. Garner, F. Martina, J. Quinta da Fonseca, P.B. Prangnell, On the observation of annealing twins during simulating β-grain refinement in Ti–6Al–4V high deposition rate AM with in-process deformation, Acta Mater. 186 (2020) 229–241. https://doi.org/10.1016/j.actamat.2020.01.009.

[85] L. Neto, S. Williams, J. Ding, J. Hönnige, F. Martina, Mechanical Properties Enhancement of Additive Manufactured Ti-6Al-4V by Machine Hammer Peening, Lect. Notes Mech. Eng. (2020) 121–132. https://doi.org/10.1007/978-981-15-0054-1_13.

[86] Y. Fu, H. Zhang, G. Wang, H. Wang, Investigation of mechanical properties for hybrid deposition and micro-rolling of bainite steel, J. Mater. Process. Technol. 250 (2017) 220–227. https://doi.org/10.1016/J.JMATPROTEC.2017.07.023.

[87] C. Xie, S. Wu, Y. Yu, H. Zhang, Y. Hu, M. Zhang, G. Wang, Defect-correlated fatigue resistance of additively manufactured Al-Mg4.5Mn alloy with in situ micro-

rolling, J. Mater. Process. Technol. 291 (2021) 117039. https://doi.org/10.1016/J.JMATPROTEC.2020.117039.

[88] H.O. Zhang, W. Rui, L. Liye, G.L. Wang, HDMR technology for the aircraft metal part, Rapid Prototyp. J. 22 (2016) 857–863. https://doi.org/10.1108/RPJ-05-2015-0047.

[89] A.K. Maurya, J.T. Yeom, S.W. Kang, C.H. Park, J.K. Hong, N.S. Reddy, Optimization of hybrid manufacturing process combining forging and wire-arc additive manufactured Ti-6Al-4V through hot deformation characterization, J. Alloys Compd. 894 (2022) 162453. https://doi.org/10.1016/J.JALLCOM.2021.162453.

[90] J.P. Oliveira, T.G. Santos, R.M. Miranda, Revisiting fundamental welding concepts to improve additive manufacturing: From theory to practice, Prog. Mater. Sci. 107 (2020) 100590. https://doi.org/10.1016/j.pmatsci.2019.100590.

[91] F. Montevecchi, G. Venturini, N. Grossi, A. Scippa, G. Campatelli, Idle time selection for wire-arc additive manufacturing: A finite element-based technique, Addit. Manuf. 21 (2018) 479–486. https://doi.org/10.1016/J.ADDMA.2018.01.007.

[92] H. Geng, J. Li, J. Xiong, X. Lin, Optimisation of interpass temperature and heat input for wire and arc additive manufacturing 5A06 aluminium alloy, Sci. Technol. Weld. Join. 22 (2017) 472–483. https://doi.org/10.1080/13621718.2016.1259031.

[93] F. Li, S. Chen, J. Shi, Y. Zhao, H. Tian, F. Li, S. Chen, J. Shi, Y. Zhao, H. Tian, Thermoelectric Cooling-Aided Bead Geometry Regulation in Wire and Arc-Based Additive Manufacturing of Thin-Walled Structures, Appl. Sci. 8 (2018) 207. https://doi.org/10.3390/app8020207.

[94] J. Shi, F. Li, S. Chen, Y. Zhao, H. Tian, Effect of in-process active cooling on forming quality and efficiency of tandem GMAW–based additive manufacturing, Int. J. Adv. Manuf. Technol. 101 (2019) 1349–1356. https://doi.org/10.1007/s00170-018-2927-4.

[95] C. Ma, C. Li, Y. Yan, Y. Liu, X. Wu, D. Li, Y. Han, H. Jin, F. Zhang, Investigation of the in-situ gas cooling of carbon steel during wire and arc additive manufacturing, J. Manuf. Process. 67 (2021) 461–477. https://doi.org/10.1016/j.jmapro.2021.05.022.

[96] D. Ding, B. Wu, Z. Pan, Z. Qiu, H. Li, Wire arc additive manufacturing of Ti6AL4V using active interpass cooling, Mater. Manuf. Process. 35 (2020) 845–851. https://doi.org/10.1080/10426914.2020.1732414.

[97] B. Wu, Z. Pan, G. Chen, D. Ding, L. Yuan, D. Cuiuri, H. Li, Mitigation of thermal distortion in wire arc additively manufactured Ti6Al4V part using active interpass cooling, Sci. Technol. Weld. Join. 24 (2019) 484–494. https://doi.org/10.1080/13621718.2019.1580439.

[98] B. Wu, Z. Pan, D. Ding, D. Cuiuri, H. Li, Z. Fei, The effects of forced interpass cooling on the material properties of wire arc additively manufactured Ti6Al4V alloy, J. Mater. Process. Technol. 258 (2018) 97–105. https://doi.org/10.1016/J.JMATPROTEC.2018.03.024.

[99] W. Hackenhaar, F. Montevecchi, A. Scippa, G. Campatelli, Air-cooling influence on wire arc additive manufactured surfaces, Key Eng. Mater. 813 (2019) 241–247. https://doi.org/10.4028/www.scientific.net/KEM.813.241.

[100] N. Kozamernik, D. Bračun, D. Klobčar, WAAM system with interpass temperature

control and forced cooling for near-net-shape printing of small metal components, Int. J. Adv. Manuf. Technol. 110 (2020) 1955–1968. https://doi.org/10.1007/s00170-020-05958-8.

[101] B. Wang, G. Yang, S. Zhou, C. Cui, L. Qin, Effects of on-line vortex cooling on the microstructure and mechanical properties of wire arc additively manufactured al-mg alloy, Metals (Basel). 10 (2020) 1–15. https://doi.org/10.3390/met10081004.

[102] V.T. Le, D.S. Mai, H. Paris, Influences of the compressed dry air-based active cooling on external and internal qualities of wire-arc additive manufactured thin-walled SS308L components, J. Manuf. Process. 62 (2021) 18–27. https://doi.org/10.1016/j.jmapro.2020.11.046.

[103] L.J. da Silva, D.M. Souza, D.B. de Araújo, R.P. Reis, A. Scotti, Concept and validation of an active cooling technique to mitigate heat accumulation in WAAM, Int. J. Adv. Manuf. Technol. 107 (2020) 2513–2523. https://doi.org/10.1007/s00170-020-05201-4.

[104] F.M. Scotti, F.R. Teixeira, L.J. da Silva, D.B. de Araújo, R.P. Reis, A. Scotti, Thermal management in WAAM through the CMT Advanced process and an active cooling technique, J. Manuf. Process. 57 (2020) 23–35. https://doi.org/10.1016/j.jmapro.2020.06.007.

[105] U. Reisgen, R. Sharma, S. Mann, L. Oster, Increasing the manufacturing efficiency of WAAM by advanced cooling strategies, Weld. World. 64 (2020) 1409–1416. https://doi.org/10.1007/s40194-020-00930-2.

[106] X. Bai, H. Zhang, G. Wang, Modeling of the moving induction heating used as secondary heat source in weld-based additive manufacturing, Int. J. Adv. Manuf. Technol. 77 (2015) 717–727. https://doi.org/10.1007/s00170-014-6475-2.

[107] Z. Li, C. Liu, T. Xu, L. Ji, D. Wang, J. Lu, S. Ma, H. Fan, Reducing arc heat input and obtaining equiaxed grains by hot-wire method during arc additive manufacturing titanium alloy, Mater. Sci. Eng. A. 742 (2019) 287–294. https://doi.org/10.1016/j.msea.2018.11.022.

[108] K. Kothari, R. Radhakrishnan, N.M. Wereley, Advances in gamma titanium aluminides and their manufacturing techniques, Prog. Aerosp. Sci. 55 (2012) 1–16. https://doi.org/10.1016/j.paerosci.2012.04.001.

[109] J. Wang, Z. Pan, D. Cuiuri, H. Li, Phase constituent control and correlated properties of titanium aluminide intermetallic alloys through dual-wire arc additive manufacturing, Mater. Lett. 242 (2019) 111–114. https://doi.org/10.1016/j.matlet.2019.01.112.

[110] J. Wang, Z. Pan, L. Wei, S. He, D. Cuiuri, H. Li, Introduction of ternary alloying element in wire arc additive manufacturing of titanium aluminide intermetallic, Addit. Manuf. 27 (2019) 236–245. https://doi.org/10.1016/j.addma.2019.03.014.

[111] Z. Yang, Q. Liu, Y. Wang, Z. Ma, Y. Liu, Fabrication of multi-element alloys by twin wire arc additive manufacturing combined with in-situ alloying, Mater. Res. Lett. 8 (2020) 477–482. https://doi.org/10.1080/21663831.2020.1809543.

[112] L. Wang, Y. Zhang, X. Hua, C. Shen, F. Li, Y. Huang, Y. Ding, Fabrication of γ-TiAl intermetallic alloy using the twin-wire plasma arc additive manufacturing process: Microstructure evolution and mechanical properties, Mater. Sci. Eng. A. 812 (2021) 141056. https://doi.org/10.1016/j.msea.2021.141056.

[113] J. Wang, Z. Pan, Y. Ma, Y. Lu, C. Shen, D. Cuiuri, H. Li, Characterization of wire

arc additively manufactured titanium aluminide functionally graded material: Microstructure, mechanical properties and oxidation behaviour, Mater. Sci. Eng. A. 734 (2018) 110–119. https://doi.org/10.1016/j.msea.2018.07.097.

[114] X. Cai, B. Dong, X. Yin, S. Lin, C. Fan, C. Yang, Wire arc additive manufacturing of titanium aluminide alloys using two-wire TOP-TIG welding: Processing, microstructures, and mechanical properties, Addit. Manuf. 35 (2020) 101344. https://doi.org/10.1016/j.addma.2020.101344.

[115] C. Shen, Z. Pan, Y. Ma, D. Cuiuri, H. Li, Fabrication of iron-rich Fe-Al intermetallics using the wire-arc additive manufacturing process, Addit. Manuf. 7 (2015) 20–26. https://doi.org/10.1016/j.addma.2015.06.001.

[116] C. Shen, Z. Pan, D. Cuiuri, B. Dong, H. Li, In-depth study of the mechanical properties for Fe3Al based iron aluminide fabricated using the wire-arc additive manufacturing process, Mater. Sci. Eng. A. 669 (2016) 118–126. https://doi.org/10.1016/j.msea.2016.05.047.

[117] C. Shen, K.D. Liss, M. Reid, Z. Pan, X. Hua, F. Li, G. Mou, Y. Huang, Y. Zhu, H. Li, Fabrication of FeNi intermetallic using the wire-arc additive manufacturing process: A feasibility and neutron diffraction phase characterization study, J. Manuf. Process. 57 (2020) 691–699. https://doi.org/10.1016/j.jmapro.2020.07.027.

[118] C. Shen, M. Reid, K.D. Liss, X. Hua, Z. Pan, G. Mou, Y. Huang, H. Li, In-situ neutron diffraction study on the high temperature thermal phase evolution of wire-arc additively manufactured Ni53Ti47 binary alloy, J. Alloys Compd. 843 (2020) 156020. https://doi.org/10.1016/j.jallcom.2020.156020.

[119] B. Dong, Z. Pan, C. Shen, Y. Ma, H. Li, Fabrication of Copper-Rich Cu-Al Alloy Using the Wire-Arc Additive Manufacturing Process, Metall. Mater. Trans. B. 48 (2017) 3143–3151. https://doi.org/10.1007/s11663-017-1071-0.

[120] Z. Qi, B. Qi, B. Cong, R. Zhang, Microstructure and mechanical properties of wire + arc additively manufactured Al-Mg-Si aluminum alloy, Mater. Lett. 233 (2018) 348–350. https://doi.org/10.1016/j.matlet.2018.09.048.

[121] Z. Qi, B. Cong, B. Qi, H. Sun, G. Zhao, J. Ding, Microstructure and mechanical properties of double-wire + arc additively manufactured Al-Cu-Mg alloys, J. Mater. Process. Technol. 255 (2018) 347–353. https://doi.org/10.1016/J.JMATPROTEC.2017.12.019.

[122] Y. Wang, X. Chen, S. Konovalov, C. Su, A.N. Siddiquee, N. Gangil, In-situ wire-feed additive manufacturing of Cu-Al alloy by addition of silicon, Appl. Surf. Sci. 487 (2019) 1366–1375. https://doi.org/10.1016/j.apsusc.2019.05.068.

[123] C. Shen, X. Hua, M. Reid, K.D. Liss, G. Mou, Z. Pan, Y. Huang, H. Li, Thermal induced phase evolution of Fe–Fe3Ni functionally graded material fabricated using the wire-arc additive manufacturing process: An in-situ neutron diffraction study, J. Alloys Compd. 826 (2020) 154097. https://doi.org/10.1016/j.jallcom.2020.154097.

[124] C. Shen, Z. Pan, D. Cuiuri, J. Roberts, H. Li, Fabrication of Fe-FeAl Functionally Graded Material Using the Wire-Arc Additive Manufacturing Process, Metall. Mater. Trans. B Process Metall. Mater. Process. Sci. 47 (2016) 763–772. https://doi.org/10.1007/s11663-015-0509-5.

[125] C. Shen, K.D. Liss, M. Reid, Z. Pan, X. Hua, F. Li, G. Mou, Y. Huang, B. Dong, D. Luo, H. Li, Effect of the post-production heat treatment on phase evolution in the

Fe3Ni–FeNi functionally graded material: An in-situ neutron diffraction study, Intermetallics. 129 (2021) 107032. https://doi.org/10.1016/j.intermet.2020.107032.

[126] F. Martina, J. Ding, S. Williams, A. Caballero, G. Pardal, L. Quintino, Tandem metal inert gas process for high productivity wire arc additive manufacturing in stainless steel, Addit. Manuf. 25 (2019) 545–550. https://doi.org/10.1016/j.addma.2018.11.022.

[127] J. Gu, J. Bai, J. Ding, S. Williams, L. Wang, K. Liu, Design and cracking susceptibility of additively manufactured Al-Cu-Mg alloys with tandem wires and pulsed arc, J. Mater. Process. Technol. 262 (2018) 210–220. https://doi.org/10.1016/j.jmatprotec.2018.06.030.

[128] M. Kumar, S.S. Kumar, A. Sharma, Bi-polynomial fourth-order weld bead model for improved material utilization and accuracy in wire-arc additive manufacturing: A case of transverse twin-wire welding, Adv. Ind. Manuf. Eng. 2 (2021) 100049. https://doi.org/10.1016/j.aime.2021.100049.

[129] W. Liu, C. Jia, M. Guo, J. Gao, C. Wu, Compulsively constricted WAAM with arc plasma and droplets ejected from a narrow space, Addit. Manuf. 27 (2019) 109–117. https://doi.org/10.1016/j.addma.2019.03.003.

[130] T.A. Rodrigues, V.R. Duarte, R.M. Miranda, T.G. Santos, J.P. Oliveira, Ultracold-Wire and arc additive manufacturing (UC-WAAM), J. Mater. Process. Technol. 296 (2021) 117196. https://doi.org/10.1016/j.jmatprotec.2021.117196.

[131] D. Samantaray, S. Mandal, A.K. Bhaduri, S. Venugopal, P.V. Sivaprasad, Analysis and mathematical modelling of elevated temperature flow behaviour of austenitic stainless steels, Mater. Sci. Eng. A. 528 (2011) 1937–1943. https://doi.org/10.1016/J.MSEA.2010.11.011.

[132] L. Palmeira Belotti, J.A.W. van Dommelen, M.G.D. Geers, C. Goulas, W. Ya, J.P.M. Hoefnagels, Microstructural characterisation of thick-walled wire arc additively manufactured stainless steel, J. Mater. Process. Technol. 299 (2022) 117373. https://doi.org/10.1016/J.JMATPROTEC.2021.117373.

[133] A. TrÄbka, Effect of Pulse Shape and Duration on Dynamic Response of a Forging System, Acta Mech. Autom. 13 (2020) 226–232. https://doi.org/10.2478/AMA-2019-0030.

[134] D. Ding, Z. Pan, D. Cuiuri, H. Li, A multi-bead overlapping model for robotic wire and arc additive manufacturing (WAAM), Robot. Comput. Integr. Manuf. 31 (2015) 101–110. https://doi.org/10.1016/j.rcim.2014.08.008.

[135] T. Altan, G. Ngaile, G. Shen, Cold and hot forging : fundamentals and applications, ASM International, 2005.

[136] J.A. McGeough, Introduction to Casting, Semi-Solid Forming and Hot Metal Forming, Compr. Mater. Process. 5 (2014) 1–2. https://doi.org/10.1016/B978-0-08-096532-1.00501-X.

[137] A. Momeni, K. Dehghani, Characterization of hot deformation behavior of 410 martensitic stainless steel using constitutive equations and processing maps, Mater. Sci. Eng. A. 527 (2010) 5467–5473. https://doi.org/10.1016/J.MSEA.2010.05.079.

[138] A. Momeni, K. Dehghani, G.R. Ebrahimi, Modeling the initiation of dynamic recrystallization using a dynamic recovery model, J. Alloys Compd. 509 (2011)

9387–9393. https://doi.org/10.1016/J.JALLCOM.2011.07.014.

[139] N.K. Park, I.S. Kim, Y.S. Na, J.T. Yeom, Hot forging of a nickel-base superalloy, J. Mater. Process. Technol. 111 (2001) 98–102. https://doi.org/10.1016/S0924-0136(01)00489-7.

[140] DRATEC Drahttechnik GmbH, Materials Datasheet, (2021). https://dratec.de/edelstahl/?lang=en (accessed February 17, 2021).

[141] Y. Lee, M. Nordin, S.S. Babu, D.F. Farson, Effect of Fluid Convection on Dendrite Arm Spacing in Laser Deposition, Metall. Mater. Trans. B. 45 (2014) 1520–1529. https://doi.org/10.1007/s11663-014-0054-7.

[142] X. Chen, J. Li, X. Cheng, B. He, H. Wang, Z. Huang, Microstructure and mechanical properties of the austenitic stainless steel 316L fabricated by gas metal arc additive manufacturing, Mater. Sci. Eng. A. 703 (2017) 567–577. https://doi.org/10.1016/J.MSEA.2017.05.024.

[143] Z. Wang, T.A. Palmer, A.M. Beese, Effect of processing parameters on microstructure and tensile properties of austenitic stainless steel 304L made by directed energy deposition additive manufacturing, Acta Mater. 110 (2016) 226–235. https://doi.org/10.1016/j.actamat.2016.03.019.

[144] B.P. Kashyap, K. Tangri, On the Hall-Petch relationship and substructural evolution in type 316L stainless steel, Acta Metall. Mater. 43 (1995) 3971–3981. https://doi.org/10.1016/0956-7151(95)00110-H.

[145] E. Aldalur, F. Veiga, A. Suárez, J. Bilbao, A. Lamikiz, High deposition wire arc additive manufacturing of mild steel: Strategies and heat input effect on microstructure and mechanical properties, J. Manuf. Process. 58 (2020) 615–626. https://doi.org/10.1016/J.JMAPRO.2020.08.060.

[146] S. Roy, B. Silwal, A. Nycz, M. Noakes, E. Cakmak, P. Nandwana, Y. Yamamoto, Investigating the effect of different shielding gas mixtures on microstructure and mechanical properties of 410 stainless steel fabricated via large scale additive manufacturing, Addit. Manuf. 38 (2021) 101821. https://doi.org/10.1016/j.addma.2020.101821.

[147] D. Carrouge, H.K.D.H. Bhadeshia, P. Woollin, Effect of δ-ferrite on impact properties of supermartensitic stainless steel heat affected zones, Sci. Technol. Weld. Join. 9 (2004) 377–389. https://doi.org/10.1179/136217104225021823.

[148] J. Oñoro, Martensite microstructure of 9-12%Cr steels weld metals, J. Mater. Process. Technol. 180 (2006) 137–142. https://doi.org/10.1016/j.jmatprotec.2006.05.014.

[149] B. Arivazhagan, G. Srinivasan, S.K. Albert, A.K. Bhaduri, A study on influence of heat input variation on microstructure of reduced activation ferritic martensitic steel weld metal produced by GTAW process, Fusion Eng. Des. 86 (2011) 192–197. https://doi.org/10.1016/j.fusengdes.2010.12.035.

[150] A. Momeni, K. Dehghani, Prediction of dynamic recrystallization kinetics and grain size for 410 martensitic stainless steel during hot deformation, Met. Mater. Int. 16 (2010) 843–849. https://doi.org/10.1007/S12540-010-1024-5.

[151] P.A. Manohar, M. Ferry, T. Chandra, Recrystallization of Ferrite and Austenite, Ref. Modul. Mater. Sci. Mater. Eng. 12 (2016) 3019–3024. https://doi.org/10.1016/B978-0-12-803581-8.03028-9.

[152] P. Schempp, C.E. Cross, R. Häcker, A. Pittner, M. Rethmeier, Influence of grain

size on mechanical properties of aluminium GTA weld metal, Weld. World. 57 (2013) 293–304. https://doi.org/10.1007/S40194-013-0026-6/TABLES/4.

[153] A.O. İrizalp, H. Durmuş, N. Yüksel, İ. Türkmen, Cold metal transfer welding of AA1050 aluminum thin sheets, Matéria (Rio Janeiro). 21 (2016) 615–622. https://doi.org/10.1590/S1517-707620160003.0059.

[154] Y. Yehorov, L.J. da Silva, A. Scotti, Exploring the use of switchback for mitigating homoepitaxial unidirectional grain growth and porosity in WAAM of aluminium alloys, Int. J. Adv. Manuf. Technol. 2019 1041. 104 (2019) 1581–1592. https://doi.org/10.1007/S00170-019-03959-W.

[155] J.J. Lewandowski, M. Seifi, Metal Additive Manufacturing: A Review of Mechanical Properties, Annu. Rev. Mater. Res. 46 (2016) 151–186. https://doi.org/10.1146/ANNUREV-MATSCI-070115-032024.

[156] T.E. Quested, Understanding mechanisms of grain refinement of aluminium alloys by inoculation, Mater. Sci. Technol. 20 (2013) 1357–1369. https://doi.org/10.1179/026708304225022359.

[157] A.N.M. Tanvir, M.R.U. Ahsan, C. Ji, W. Hawkins, B. Bates, D.B. Kim, Heat treatment effects on Inconel 625 components fabricated by wire + arc additive manufacturing (WAAM)—part 1: microstructural characterization, Int. J. Adv. Manuf. Technol. 103 (2019) 3785–3798. https://doi.org/10.1007/S00170-019-03828-6/FIGURES/11.

[158] C. Li, Y. Tian, Y. Chen, P. Hodgson, X. Wu, Y. Zhu, A. Huang, Hierarchical layered and refined grain structure of Inconel 718 superalloy produced by rolling-assisted directed energy deposition, Addit. Manuf. Lett. 1 (2021) 100009. https://doi.org/10.1016/J.ADDLET.2021.100009.

[159] R. Tamasgavabari, A.R. Ebrahimi, S.M. Abbasi, A.R. Yazdipour, The effect of harmonic vibration with a frequency below the resonant range on the mechanical properties of AA-5083-H321 aluminum alloy GMAW welded parts, Mater. Sci. Eng. A. 736 (2018) 248–257. https://doi.org/10.1016/J.MSEA.2018.08.106.

[160] G. Zhao, Z. Wang, S. Hu, S. Duan, Y. Chen, Effect of ultrasonic vibration of molten pool on microstructure and mechanical properties of Ti-6Al-4V joints prepared via CMT + P welding, J. Manuf. Process. 52 (2020) 193–202. https://doi.org/10.1016/J.JMAPRO.2020.01.045.

[161] S.H. Xia, L. V. Vychigzhanina, J.T. Wang, I. V. Alexandrov, A. V. Sharafutdinov, Controllable bimodal structures in hypo-eutectoid Cu-Al alloy for both high strength and tensile ductility, Mater. Sci. Eng. A. 490 (2008) 471–476. https://doi.org/10.1016/j.msea.2008.03.002.

[162] C. Shen, Z. Pan, D. Ding, L. Yuan, N. Nie, Y. Wang, D. Luo, D. Cuiuri, S. van Duin, H. Li, The influence of post-production heat treatment on the multi-directional properties of nickel-aluminum bronze alloy fabricated using wire-arc additive manufacturing process, Addit. Manuf. 23 (2018) 411–421. https://doi.org/10.1016/J.ADDMA.2018.08.008.

[163] A. Queguineur, & J. Marolleau, & A. Lavergne, G. Rückert, Evaluation of tandem controlled short-circuit GMAW for improved deposition in additive manufacture of large Nickel Aluminium Bronze naval components, Weld. World. 64 (2020) 1389–1395. https://doi.org/W0.1007/s40194-020-00925-z/Published.

[164] T.G. Santos, P. Vilaça, R.M. Miranda, Electrical conductivity field analysis for evaluation of FSW joints in AA6013 and AA7075 alloys, J. Mater. Process.

Technol. 211 (2011) 174–180. https://doi.org/10.1016/j.jmatprotec.2010.08.030.

[165] L. Vázquez, & N. Rodríguez, I. Rodríguez, E. Alberdi, & P. Álvarez, Influence of interpass cooling conditions on microstructure and tensile properties of Ti-6Al-4V parts manufactured by WAAM, Weld. World. 64 (2020) 1377–1388. https://doi.org/10.1007/s40194-020-00921-3/Published.

[166] L. Tonelli, R. Sola, V. Laghi, M. Palermo, T. Trombetti, L. Ceschini, Influence of Interlayer Forced Air Cooling on Microstructure and Mechanical Properties of Wire Arc Additively Manufactured 304L Austenitic Stainless Steel, Steel Res. Int. 92 (2021) 2100175. https://doi.org/10.1002/SRIN.202100175.

[167] Y. Shi, Z. Han, Effect of weld thermal cycle on microstructure and fracture toughness of simulated heat-affected zone for a 800 MPa grade high strength low alloy steel, J. Mater. Process. Technol. 207 (2008) 30–39. https://doi.org/10.1016/J.JMATPROTEC.2007.12.049.

[168] S.S. Babu, The mechanism of acicular ferrite in weld deposits, Curr. Opin. Solid State Mater. Sci. 8 (2004) 267–278. https://doi.org/10.1016/j.cossms.2004.10.001.

[169] H. Zhao, E.J. Palmiere, Effect of austenite grain size on acicular ferrite transformation in a HSLA steel, Mater. Charact. 145 (2018) 479–489. https://doi.org/10.1016/J.MATCHAR.2018.09.013.

[170] H.E. Coules, P. Colegrove, L.D. Cozzolino, S.W. Wen, High pressure rolling of low carbon steel weld seams: Part 1 – Effects on mechanical properties and microstructure, Sci. Technol. Weld. Join. 18 (2013) 76–83. https://doi.org/10.1179/1362171812Y.0000000079.

[171] C. Capdevila, F.G. Caballero, C. García De Andrés, Determination of Ms Temperature in Steels: A Bayesian Neural Network Model, ISIJ Int. 42 (2002) 894–902. https://doi.org/10.2355/ISIJINTERNATIONAL.42.894.

Appendix

Appendix A

For the metallurgical characterization, micro hardness and eddy currents tests, cross sections with approximately 10 mm thick were cut from the samples and embedded in epoxy resin. Then the samples were successively grinded using SiC papers with abrasive grit sizes of P240, P320, P400, P600, P1200 and P2500. The samples were polished in a *MicroFloc*^{TM} polishing cloth using a *MetaDi Ultra* 1 µm diamond suspension paste. The chemical composition of the etchants used to reveal the microstructure of the different materials is shown in Table A1.

Table A1 – Etchant composition used to reveal the microstructure of each material

Material	Reagent	Composition		Immersion time
ER1070	Keller's	Distilled water -	190 ml	10-30 s
		Nitric acid -	5 ml	
		Hydrochloric acid -	3 ml	
		Hydrofluoric acid -	2 ml	
ER316 LSi & ER410 NiMo	Vilella's	Ethanol -	100 ml	60-120 s
		Hydrochloric acid -	5 ml	
		Picric Acid -	1 g	
ER70S-6 ER110S-G	Nital	Ethanol -	90 ml	5-15 s
		Nitric acid -	10 ml	
ER NiCrMo-3	--	Ethanol -	15 ml	10-20 s
		Acetic acid -	10 ml	
		Nitric acid -	10 ml	
ER NiCu7	Carapella's	Ethanol -	99 ml	10-20 s
		Hydrochloric acid -	2 ml	
		Iron(II) chloride -	5 g	

ERCuAL-A2	--	Ethanol -	71 ml	1-5 s
		Hydrochloric acid -	24 ml	
		Iron(II) chloride -	5 g	

Appendix B

Code of the *Python* software

```
import cv2
import numpy as np
from matplotlib import pyplot as plt
from PIL import Image

# initial inputs#
vid_name = 'Martelo_Mesa_10000fps_512x256_INOX_l3_C001H001S0001.mp4'
ini = 500
fim = 1000
Frame_rate = 10000
H_marca_mm= 8.65


vidcap = cv2.VideoCapture(vid_name)
length = int(vidcap.get(cv2.CAP_PROP_FRAME_COUNT))
print (vidcap.get(cv2.CAP_PROP_FRAME_COUNT))

last=[]
px_distance_l=[]
px_distance=[]
count = 0

#process each frame#
for i in range(fim-ini):

    vidcap.set(1, i+ini)

    ret, frame = vidcap.read()
    grayscaled = cv2.cvtColor(frame,cv2.COLOR_BGR2GRAY)
    ret, th1 = cv2.threshold(grayscaled,25,255,cv2.THRESH_BINARY)

#Uncoment for plot each processed frame#
    # cv2.imshow("frame%d.jpg" % count, th1)
    # cv2.imwrite("fra1.jpg", th1)
    # cv2.waitKey(0)
    # cv2.destroyAllWindows()

#find the mark position#
    row, col = th1.shape
    x=[]
```

```
    for i in range(col-1):    #row-1
        n = th1[30,i+1]  #    n = th1[i+1,960]

        if n == 255:
            x.append(i) # get x indices
            px_distance_l = max(x)-min(x)
        # if i == 505:
        #     x.append(i)
        #     px_distance_l = max(x)-min(x)
    px_distance.append(px_distance_l)
    last.append(min(x))


delta_px = np.array(last)-min(last)
delta_mm = delta_px*(H_marca_mm/H_marca_px)


#plot graph#

X = np.linspace(0, (1/Frame_rate)*(fim-ini-1),fim-ini)
X2= np.linspace(0,len(px_distance),len(px_distance))

plt.style.use   ('seaborn')
fig, (ax1,ax2,ax3) = plt.subplots(3)
ax1.plot(X,delta_mm)
ax1.set_title("Psition_mm x time")
ax2.plot(X,delta_px)
```

2022

Valdemar Rebelo Duarte

DEVELOPMENTS IN DIRECTED ENERGY DEPOSITION ADDITIVE MANUFACTURING: IN-SITU HOT FORGING AND INDIRECT COOLING